VNIVERSITAT DE VALÈNCIA

Departament d'Astronomia i Astrofisica

Gravitational Lensing: the Structure of Quasars and Galaxies

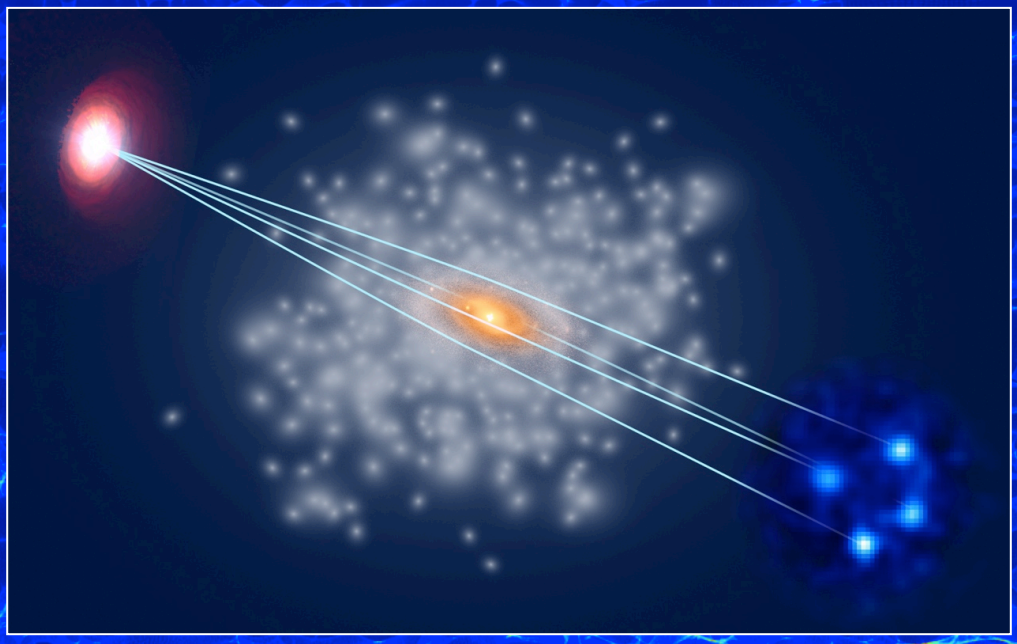

PhD Thesis

Héctor Vives Arias

2016

VNIVERSITAT DE VALÈNCIA

Gravitational Lensing: the Structure of Quasars and Galaxies

Héctor Vives Arias

Departamento de Astronomía y Astrofísica

Universitat de València

PhD thesis in Physics

PhD Advisor: José A. Muñoz Lozano

October 2016

Dr. José A. Muñoz Lozano, profesor titular del Departamento de Astronomía y Astrofísica de la Universidad de Valencia,

CERTIFICA:

Que la presente memoria, **Gravitational Lensing: the Structure of Quasars and Galaxies**, ha sido realizada bajo su dirección en el Departamento de Astronomía y Astrofísica de la Universidad de Valencia por D. Héctor Vives Arias y constituye su Tesis Doctoral, que presenta para optar al grado de Doctor en Física.

Y para que así conste, en cumplimiento de la legislación vigente, firma el presente Certificado en Valencia a 19 de septiembre de 2016.

Fdo.: José A. Muñoz Lozano

A mis padres,
que respondiendo de pequeño a todas mis preguntas
no saciaron mi curiosidad, sino todo lo contrario.

Acknowledgements

Many people have helped me in one way or another over the years that led to the culmination of this PhD thesis, and I would like to use these pages to express how grateful I am to them. I apology in advance for all the names I have not mentioned, but I hope that they all know how deeply I appreciate all they have done for me.

First, I have to thank my advisor, José A. Muñoz, who made this work possible in the first place by offering me a contract when I was buried in paperwork and frantically searching for a research project and advisor for my Master's thesis, from thousands of kilometers away. This is what introduced me to the field of gravitational lensing in the first place, in which I have continued working since then under his guidance.

Many thanks go also to Evencio Mediavilla, for his always cheerful and kind disposition, and for accepting me at the Instituto de Astrofísica de Canarias for a few productive months, and to our other collaborators, Jorge Jiménez and Christopher S. Kochanek, for their valuable insights and effort to achieve the best results in our work.

I would also like to thank Neal Jackson, for being so helpful and teaching me so much about radio interferometry and Python during my long stay in the University of Manchester and the Jodrell Bank Centre for Astrophysics, and for his patience and kindness with this student that had to learn so many things from scratch. Special thanks go also to Mark Purver, Libby Jones, Christina Smith, Carl Roberts, Jonathan Quinn, Rachana Bhatawdekar, Kerry Louise Hebden, and the rest of friends that I made when I was there. And of course I must thank Rebecca Winstanley for five great years, and for being the reason of going to Manchester to do research there in the first place.

I am also incredibly grateful for the diligence and effectiveness of the administrative staff of the Department of Astronomy and Astrophysics of the University of Valencia that I've worked with, Felicidad Pellicer and Manel González, because I don't know what we would do without them to help with the endless bureaucracy.

The rest of the department also deserve my thanks, since practically all of them have helped and taught me at some point, and are always ready to help when asked. I am deeply appreciative of the generosity of Susana Planelles, my first office mate in Valencia, for helping me so much during my Master's thesis despite being busy herself finishing her own PhD, putting me on track for what would become six years of research so far. And special thanks go to Ana Mosquera, who I've not met in person yet but whose PhD thesis has been the basis and starting point of my work, so much that I've been keeping a copy with me for the same amount of time, which has been consulted very often.

Many thanks go to Enric Marco for the technical help and support every time the

desktop computer failed, and for introducing me to the 'Nits de Divendres' activity, in which a few nights a year I could disconnect a bit, observe with a telescope, and explain science to others so that I could realize again that, despite some hardships, astronomy is indeed fascinating. This was done while also having a good time with Fernando Ballesteros, Lorena Seoane, and Rebecca Azulay. I must also thank her for allowing me to share some of the frustrations that arise when things don't go so well, and making them easier to overcome.

Thanks are also due to the Generalitat Valenciana for the Prometeo contract I enjoyed in 2010-2011, and the Spanish former Ministerio de Ciencia e Innovación, whose grant BES-2011-044200 provided adequate funding for four of my years of research.

I would also like to thank my group of friends from the undergrad days, especially those with whom I have remained in contact and have allowed me to vent when I felt it necessary, and offering advice when they have experience with similar situations. Adrián Dorado has been along for almost twenty years of my life, and I still enjoy the occasional roleplaying gaming, geeky conversations, or socialization; Mireia Crispín, has been driven away by her general excellence, but it is still a pleasure to speak with her online from time to time; I have seen Javier Barrios less frequently lately, but I hope his thesis reaches a satisfactory conclusion soon; Yolanda Godoy I have seen less (we should organize something!), but hopefully things are well too! And thanks to Sergio Gimeno for making my office confinement less solitary in the last weeks, providing interesting conversation, entertainment, and also some problem-solving when some aspect of research becomes apparently stuck.

A special mention should go to Juan Ayala, my best physics teacher in high school, of whom I happened to be a student in the last year before university, when I concluded that I was more suited to science than engineering (perhaps it had something to do).

I also wanted to thank Itahisa N. González, who took the time whenever I went to Tenerife to force me to go and see some places, or to take advantage of the great skies and go up the mountain to watch the stars.

Science communication has played an important role in my life, so I would like to acknowledge some people and organizations that have vastly influenced my path along the years. First, I want to thank the astronomy group CIDAM, for providing the means for me to watch the Milky Way from time to time away from light pollution when I lived in Elche, and allowing me to practice my communication skills by explaining some astrophysics or giving talks to astronomy aficionados (I know I have been completely absent during my thesis, but I promise to try to participate in activities when I can). I am also very grateful for the science communicators like Sergio L. Palacios, Remo Tamayo, and others, who helped keep my motivation up as a university student even when the subjects in class were a bit dull, and inspired me to write about science on my own blog.

I deeply appreciate the generosity of the Naukas science communication platform for offering me the incredible opportunity of participating in science communication events that continue helping, via observation and practice, to improve my own skills, and to

regain an appreciation for my own research by explaining it to others (I owe you several blog posts, but I figure after my thesis I will have time again). Some of their bloggers, like Francis Villatoro, Daniel Marín, César Tomé and others, have, in addition, summarized and explained new astrophysics papers that have more than once been useful in my own research.

Also, thanks to Víctor Marín, Elena Denia, and Antonio Sánchez, for letting me participate in their science radio program, El Café Cuántico, and then letting me be part of it for a whole season.

Many thanks go to all my friends on Twitter, who have in a way shared this adventure, reading both my complaints and my enthusiasm, offering advice and encouragement, and increasing my joy when things seemed to go well.

Thanks also to the University of Valencia and Tarongers Archery Clubs, for providing an engaging but relaxing way to do at lest some exercise during these years, while I had a good time in which to disconnect from everyday troubles once or twice per week.

I am grateful for the friendship of the many members of the Spanish Tolkien Society, and especially Adela Torres, who introduced me to this hidden realm and their marvelous inhabitants, that provided excellent experiences, companionship, inspiration, and enthusiasm at a time where they were needed.

My very heartfelt thanks go to Marta Lúthien Gutiérrez, who will probably be proud when I earn the title of Doctor, for having been there this last year, for the endless interesting conversations, for her encouragement, and for ending up convincing me to remain in academia after earning this degree, despite my temporary doubts.

And last but not least, I want to thank my family for their lifelong support, for exposing me to science since the beginning and feeding my curiosity as best they could, for encouraging me to pursue this career, offering advice, and helping me in any way possible. Thanks for listening to my rants when things weren't going well, and for making an effort to understand the science I do, be it when they asked me directly about it or when I tried to explain my frustration when something didn't work. I am incredibly grateful for everything they have done for me my whole life, and I would not be who or where I am today if it wasn't for them.

Abstract

In this PhD thesis we use gravitational lens systems in which a galaxy produces multiple images of a distant quasar to study the properties of both the unresolved structure of the lensed quasar and the mass distribution in the gravitational lens.

First, we estimate the size and the logarithmic slope of the temperature profile in the accretion disk of the lensed quasar Q 2237+0305 using a method that is independent of the component velocities, based on six epochs of multi-wavelength narrowband images from the Nordic Optical Telescope. For each pair of lensed images and each photometric band, we determine the microlensing amplitude and chromaticity using pre-existing mid-IR photometry to define the baseline for no microlensing magnification. A statistical comparison of the combined microlensing data (6 epochs $\times$ 5 narrow bands $\times$ 6 image pairs) with simulations based on microlensing magnification maps gives Bayesian estimates for the half-light radius of $R_{1/2} = 8.5^{+7.5}_{-4.0}\sqrt{\langle M\rangle/0.3\,\mathrm{M}_\odot}$ light-days at $\lambda_{rest} = 1736$ Å, and $p = 0.95 \pm 0.33$ for the exponent of the logarithmic temperature profile $T \propto R^{-1/p}$. This size estimate is in good agreement with most recent studies. Other works based on the study of single microlensing events predict smaller sizes, but could be statistically biased by focusing on high-magnification events.

Then, we present new mid-IR observations of this quadruply lensed quasar taken with CanariCam on the Gran Telescopio Canarias (GTC). Mid-IR emission by hot dust, unlike the optical and near-IR emission from the accretion disk, is unaffected by the interstellar medium (extinction/scattering) or stellar microlensing. We compare these "true" ratios to the same optical/near-IR (stellar) microlensed flux ratios observed before to recalculate the structure of the quasar accretion disk. This time we find a half-light radius of $R_{1/2} = 3.4^{+5.3}_{-2.1}\sqrt{\langle M\rangle/0.3\,\mathrm{M}_\odot}$ light-days, and an exponent for the temperature profile $R \propto \lambda^p$ of $p = 0.79 \pm 0.55$, where $p = 4/3$ for a standard thin-disk model. If we assume that the differences in the mid-IR flux ratios measured over the years are due to microlensing variability, we find a lower limit for the size of the mid-IR emitting region of $R_{1/2} \gtrsim 200\sqrt{\langle M\rangle/0.3\,\mathrm{M}_\odot}$ light-days. We also test for the presence of substructure/satellites by comparing the observed mid-IR flux ratios with those predicted from smooth lens models. We can explain the differences if the surface density fraction in satellites near the lensed images is $\alpha = 0.033^{+0.046}_{-0.019}$ for a singular isothermal ellipsoid plus external shear mass model or $\alpha = 0.013^{+0.019}_{-0.008}$ for a mass model combining ellipsoidal NFW and de Vaucouleurs profiles in an external shear.

Next, we show Very Large Array detections of radio emission in four other quadruply lensed quasars: HS 0810+2554, RX J0911+0511, HE 0435−1223 and SDSS J0924+0219,

and extended Multi-Element Remote Linked Interferometer (e-MERLIN) observations of two of the systems. The first three are detected at a high level of significance, and SDSS J0924+0219 is detected. HS 0810+2554 is resolved, allowing us for the first time to achieve 10-mas resolution of the source frame in the structure of a radio quiet quasar. The others are unresolved or marginally resolved. All four objects are among the faintest radio sources yet detected, with intrinsic flux densities in the range 1–5μJy; such radio objects, if unlensed, will only be observable routinely with the Square Kilometre Array. The observations of HS 0810+2554, which is also detected with e-MERLIN, strongly suggest the presence of a mini-AGN, with a radio core and milliarcsecond scale jet. The flux densities of the lensed images in all but HE 0435−1223 are consistent with smooth galaxy lens models without the requirement for smaller-scale substructure in the model, although some interesting anomalies are seen between optical and radio flux densities. These are probably due to microlensing effects in the optical.

Finally, we compile a sample of 13 gravitational lens systems with quadruply imaged quasars with observed flux ratios in mid-infrared, radio or spectral narrow lines. We use their flux ratio anomalies to estimate the amount of substructure in the dark matter halo of lens galaxies. We assume that the smooth gravitational potential of the galaxies is well modeled by a Singular Isothermal Ellipsoid (SIE) plus external shear (γ) along with an additional Singular Isothermal Sphere (SIS) in some cases, and that the cause of the flux ratio anomalies is dark matter subhalos described by pseudo-Jaffe density profiles. After excluding 5 of the systems from the analysis due to various concerns, our Bayesian estimate for the Einstein radius of the subhalos (as a fraction of the Einstein radius of their corresponding lens galaxy) is $b = 0.0003^{+0.0005}_{-0.0002}$, and their abundance (as a fraction of the total surface density of the lens galaxy at the image positions) is $\alpha = 0.075^{+0.030}_{-0.021}$.

Contents

List of Figures

List of Tables

Resumen

Introducción

El efecto de lente gravitacional es la desviación que una acumulación de masa provoca en los rayos de luz debido a la curvatura que ésta crea en el espacio-tiempo. Este fenómeno es puramente gravitacional, y debido a ello se ha convertido en una de las principales herramientas en astrofísica para analizar efectos causados únicamente por la interacción gravitatoria, sin depender de suposiciones sobre los mecanismos con los que un objeto emite la luz que observamos. Esto nos permite estudiar la *materia oscura*, un tipo de materia abundante en el Universo pero de naturaleza aún desconocida, y que no parece interaccionar de otra forma que no sea la gravedad. Además, la distorsión que las lentes gravitacionales producen en las imágenes de objetos lejanos hace que en muchos casos nos llegue más luz de éstos, de modo que hacen visibles objetos tenues y galaxias tan distantes que de otra forma serían indetectables con la tecnología actual. Estas magnificaciones del brillo del objeto que actúa como fuente de luz tras la lente dependen de forma tan precisa del alineamiento concreto de ambos, que incluso el efecto gravitacional de estrellas individuales es apreciable en algunos sistemas. Este fenómeno ha permitido analizar la estructura de las regiones centrales de los quásares, objetos muy brillantes pero extremadamente lejanos, cuando las estrellas de una galaxia lente se interponen en el camino que su luz sigue hasta llegar a nosotros.

Cuando una galaxia se sitúa frente a una fuente de luz puntual, el efecto lente suele crear dos o cuatro imágenes de la misma, y la posición y la magnificación de cada una de ellas dependerá de la distribución concreta de masa en la lente gravitacional (siendo los flujos resultantes de cada imagen más sensibles a ésta que sus posiciones). Estos casos en los que podemos distinguir las distintas imágenes individuales creadas por la lente se conocen como *macrolensing*. Hay otras situaciones en las que las lentes tienen una masa muy baja, y las imágenes resultantes tienen tan poca separación entre sí que no somos capaces de distinguirlas. En estos casos, conocidos como *microlensing*, vemos sólo que la fuente puntual ha cambiado de brillo a lo largo del tiempo (si la observamos con regularidad) o que su imagen tiene una luminosidad que no cuadraría con lo que sabemos del objeto si no hubiese microlentes afectándola. Además, la magnitud del microlensing depende del

tamaño de la fuente y, si éste es distinto en diferentes longitudes de onda, tiene lugar el fenómeno conocido como *microlensing cromático*. En el caso de una distribución de lentes afectando al brillo de una fuente, como la magnificación que sufre una región determinada depende mucho de su posición concreta respecto de las lentes, una fuente extensa puede tener partes de su superficie más magnificadas que otras. Si nuestra resolución sólo nos permite medir cambios en el brillo total de la fuente extensa debido a que no distinguimos su estructura, los cambios observados estarán amortiguados respecto a los que sufriría una fuente verdaderamente puntual. Por tanto, este fenómeno puede utilizarse para estimar el tamaño del objeto que sufre el efecto lente aunque lo veamos sólo como un punto de luz.

Un tipo de fuente puntual muy útil en estudios con lentes gravitacionales son los *quásares*, objetos muy brillantes y muy lejanos que emiten luz en un gran abanico de longitudes de onda. Son núcleos de galaxias en los que un agujero negro supermasivo está en el proceso de acretar materia, y la acelera a tales velocidades cuando se adentra en el potencial gravitatorio que se forma un disco de gas extremadamente caliente. Éste emite rayos X en su parte más interna, y luz ultravioleta y visible conforme su temperatura desciende hacia el exterior. Es de este disco (de sólo unos días luz de radio) de donde proviene la mayor parte de la energía del quásar, que además produce efectos observables en la materia a su alrededor. En la zona que rodea al disco se sitúan nubes de gas con un espectro de emisión con líneas muy ensanchadas debido al efecto Doppler, y más allá, cuando la temperatura ha descendido lo suficiente como para no sublimarlo, suele haber una gran acumulación de polvo en forma de toroide rodeando el centro, que emite luz en el infrarrojo medio debido a su temperatura templada. Por el hueco central del toroide surge una región bicónica de gas a baja presión ionizado por la fuente central, y que emite líneas espectrales estrechas en el visible e infrarrojo cercano. En torno al 10 % de los quásares también poseen chorros relativistas de materia que surgen de la zona más cercana al agujero negro, y que son detectables por su gran emisión en ondas de radio. Esta diversidad de regiones y mecanismos de emisión permite, eligiendo la longitud de onda en la que observar el sistema, aprovechar el microlensing cromático para estudiar su zona central o bien eliminar el efecto de las estrellas individuales de la galaxia lente a la hora de analizar su distribución de masa.

Esta posibilidad permite a su vez utilizar este tipo de sistemas, con una galaxia lente produciendo imágenes múltiples de un quásar, para estudiar la distribución de la materia oscura en esas galaxias. Los modelos que más se ajustan a las observaciones son los de materia oscura fría (*cold dark matter*, CDM), en los que la materia que la compone se mueve a velocidades no relativistas. No obstante, en las simulaciones con CDM los halos de materia oscura de las galaxias se forman a partir de numerosos subhalos de menor masa, y en ellas en torno a un 10 % de la masa total permanece en subhalos que sobreviven a los efectos de marea. Esto corresponde a cifras de cientos o miles de subhalos por galaxia, y en cambio el número de galaxias satélite observadas es muchísimo menor (apenas un par de

docenas en torno a la Vía Láctea). Dichos subhalos podrían o bien no existir, necesitando revisiones en la teoría o simulación, o existir pero haber sido vaciados de materia bariónica por algún proceso que haya hecho que permanezcan oscuros. La sensibilidad del efecto de lente gravitacional a la distribución de masa en la galaxia lente podría dar respuesta a este problema si se analizan con detenimiento los cocientes de flujo de las imágenes múltiples del quásar, y el perfil de masa para la galaxia sin subhalos está bien reconstruido.

Capítulo 2

El disco de acreción de un quásar está más caliente en su zona central y menos hacia el exterior, de modo que la mayor intensidad de su emisión tendrá lugar en longitudes de onda más largas a radios mayores. Esto hace que el disco presente un tamaño aparente distinto al ser observado en diferentes longitudes de onda y, por tanto, la presencia de microlensing cromático en un sistema en el que las imágenes del quásar se ven afectadas por las estrellas de la galaxia lente permite estimar tanto el tamaño del disco como el exponente logarítmico de su perfil de temperatura.

Un sistema ideal para este tipo de estudio es Q 2237+0305, la Cruz de Einstein. Debido a su cercanía, posee una mayor velocidad angular relativa entre lente y fuente, se forman cuatro imágenes del quásar a través del bulbo de la galaxia lente donde la densidad de estrellas es alta, y hay un retardo temporal muy bajo entre la luz que nos llega de cada imagen, que hace innecesario corregirlo para eliminar la variabilidad intrínseca del quásar en los datos. En este trabajo se utilizan observaciones de este sistema con filtros estrechos en el óptico e infrarrojo cercano tomadas en el Nordic Optical Telescope (NOT) en La Palma en seis épocas diferentes entre 2003 y 2007, que muestran variaciones debidas al microlensing y distintas en cada longitud de onda.

Para realizar los cálculos, primero se genera un 'mapa de magnificación' para cada imagen del quásar, que muestra la magnificación que sufriría una fuente puntual en cada una de las posiciones de una región afectada por microlensing debido a las estrellas de la galaxia. Después, se convolucionan los mapas con el perfil de brillo del disco correspondiente a los valores que se quieren evaluar de sus parámetros (se realiza una convolución por cada valor del tamaño aparente del disco en cada longitud de onda). Luego, se seleccionan posiciones aleatorias en cada mapa, se calculan las magnificaciones por microlensing que predicen, y se comparan con las observaciones. Repitiendo millones de veces para cada conjunto de parámetros esta comparación con las observaciones de la predicción teórica de las diferencias de brillo entre posiciones aleatorias en cada uno de los cuatro mapas, se obtiene la distribución de probabilidad para el tamaño y el perfil de temperaturas en cada modelo del disco. El tamaño del disco varía con la longitud de onda mediante la relación $r_s(\lambda_2) = (\lambda_2/\lambda_1)^p r_s(\lambda_1)$, donde r_s es su radio de escala y depende del modelo

entre los tres utilizados: un perfil gaussiano, $I(R) \propto \exp(-R^2/2r_s^2)$; el modelo de disco delgado, $I(R) \propto \left(\exp\left[(R/r_s)^{1/p}\right] - 1\right)^{-1}$; y un híbrido, $I(R) \propto \left(\exp\left[(R/r_s)^{3/4}\right] - 1\right)^{-1}$. Si se escoge en su lugar el radio efectivo $R_{1/2}$, es decir, el radio al cual se emite la mitad de la luminosidad total, las predicciones por microlensing deberían ser parecidas para los tres. Para separar qué parte de las diferencias de brillo entre distintas imágenes del quásar sería causada por el microlensing y cuál por el macrolensing, se utilizan medidas de los cocientes de flujo en infrarrojo medio de la literatura, que no se vería afectado por la extinción en el medio interestelar, y al provenir del toroide de polvo debería ser inmune al microlensing debido a su gran tamaño.

Para la longitud de onda $\lambda_1 = 1736$ Å, las estimaciones del tamaño para los tres modelos (gaussiano, híbrido y disco delgado) son, respectivamente, $R_{1/2} = (8{,}3^{+11{,}8}_{-4{,}8}, 9{,}0^{+8{,}4}_{-4{,}4}, 8{,}5^{+7{,}5}_{-4{,}0})$ $\sqrt{\langle M \rangle / 0{,}3\,\mathrm{M}_\odot}$ días luz, donde M es la masa de las microlentes. Como se esperaba, son muy similares entre sí, y además consistentes con estimaciones previas, que son a su vez mayores que la predicción teórica para el modelo de disco delgado. Para el exponente del perfil de temperaturas se obtiene $p = 1{,}0 \pm 0{,}3$ para los modelos híbrido y de disco delgado mientras que para el gaussiano es más pronunciado, con $p = 0{,}7 \pm 0{,}3$. No obstante, ambas medidas son consistentes dentro de la incertidumbre, y los dos primeros están próximos a la predicción teórica de $p = 4/3$ para el modelo de disco delgado estándar.

Capítulo 3

Dada la importancia de los flujos en infrarrojo medio para determinar la distribución de la masa en una lente gravitacional al no verse afectados por microlensing de las estrellas o extinción por el medio interestelar, realizamos nuevas observaciones del sistema Q 2237+0305 en 2012 y 2013 utilizando el instrumento CanariCam en el Gran Telescopio CANARIAS (GTC), en La Palma. En el filtro Si5 ($\lambda_c = 11{,}6\,\mu$m, $\Delta\lambda = 0{,}9\,\mu$m), obtenemos los siguientes cocientes de flujo entre las cuatro imágenes del quásar: B/A = $0{,}99 \pm 0{,}03$, C/A = $0{,}69 \pm 0{,}10$ y D/A = $0{,}84 \pm 0{,}13$. Estos cocientes difieren de los obtenidos por otros autores en observaciones en infrarrojo medio en 2005, 2000 y 1999, y éstos entre sí. Ante la posibilidad de que la variación se deba a errores sistemáticos u otros efectos, calculamos la media ponderada de los cocientes de flujo como una representación más fiel de los cocientes "verdaderos": B/A = $0{,}97 \pm 0{,}03$, C/A = $0{,}51 \pm 0{,}02$ y D/A = $0{,}92 \pm 0{,}04$. Posteriormente, ajustamos modelos sencillos del perfil de masa de la galaxia lente a los cocientes de flujo de GTC a la media ponderada de todas las observaciones, y a las posiciones de las imágenes únicamente sin usar los flujos para constreñir el ajuste. Los modelos usados son un Elipsoide Singular Isotermo con un shear externo (SIE + γ), y un halo de tipo Navarro, Frenk & White con shear externo más un perfil de Vaucouleurs para reproducir el bulbo y la barra de la galaxia (NFW + de Vaucouleurs + γ).

A continuación, estimamos el tamaño y perfil de temperaturas del disco de acreción del quásar usando el mismo método del capítulo 2 y el modelo híbrido. Para los cocientes de flujo que hemos medido con el GTC obtenemos $R_{1/2} = 3{,}4^{+5,3}_{-2,1}\sqrt{\langle M\rangle/0{,}3\,\mathrm{M}_\odot}$ días luz y $p = 0{,}79 \pm 0{,}55$, mientras que para la media ponderada de todos los cocientes de flujo observados, las estimaciones son $R_{1/2} = 6{,}2^{+7,4}_{-3,4}\sqrt{\langle M\rangle/0{,}3\,\mathrm{M}_\odot}$ días luz y $p = 0{,}95 \pm 0{,}39$. Dentro de sus intervalos de error, los valores son consistentes a pesar de la diferencia en los cocientes de flujo utilizados en cada caso.

Una explicación alternativa a la variación observada en los flujos medidos en infrarrojo medio en distintas épocas es que sea debida a microlensing, si parte de la emisión se produce en las regiones centrales del quásar y no en el toroide de polvo. Para analizar esta posibilidad, calculamos con un método análogo al anterior el tamaño que se obtendría para la región de emisión de infrarrojo medio si la variabilidad se debiese a microlensing. Para ello utilizamos la media ponderada como flujos no afectados por microlentes, y obtenemos un valor de $R_{1/2} = 228^{+201}_{-107}\sqrt{\langle M\rangle/0{,}3\,\mathrm{M}_\odot}$ días luz. Dado que el radio interno mínimo al que puede sobrevivir el polvo en un quásar de esa luminosidad es mucho mayor, o bien hay una componente del disco de acreción que emite infrarrojo medio y se ve más afectada por microlensing debido a su tamaño, o la variación se debe a errores sistemáticos. En este último caso habríamos estimado un límite inferior para el radio del toroide, $R_{1/2} \gtrsim 200\,\sqrt{\langle M\rangle/0{,}3\,\mathrm{M}_\odot}$ días luz.

Por último, utilizamos los cocientes de flujo medidos en infrarrojo medio para estimar la fracción de masa de la galaxia que tendría que permanecer en forma de subhalos de materia oscura, si las diferencias entre los flujos observados y los predichos por modelos sencillos representan anomalías provocadas por su presencia. Para ello, usamos la media ponderada de los cocientes, que asumimos menos afectada por posibles errores sistemáticos, y las predicciones de los modelos sencillos de masa calculados usando únicamente las posiciones de las imágenes múltiples del quásar. Para el modelo SIE + γ obtenemos una fracción $\alpha = 0{,}033^{+0,046}_{-0,019}$, y para el NFW + de Vaucouleurs + γ estimamos $\alpha = 0{,}013^{+0,019}_{-0,008}$. Estos valores muestran que sólo una pequeña fracción de masa en subhalos es suficiente para reproducir las observaciones, y son consistentes con la predicción de CDM (1 % en las regiones internas del halo de materia oscura).

Capítulo 4

Para estudiar la presencia de subestructura en el halo de materia oscura de las galaxias, también se usaban tradicionalmente observaciones de los cocientes de flujo en radio de las imágenes múltiples de un quásar debido al efecto lente, que tampoco estarían afectados por microlensing o por extinción. El problema es que del centenar de sistemas lente des-

cubiertos con esta configuración, sólo unos pocos contienen un quásar que sea un fuerte emisor en radio. Para ampliar la muestra se puede aprovechar el hecho de que todos los quásares son susceptibles de tener emisión en radio a algún nivel, y que la magnificación producida en las imágenes múltiples del quásar en un sistema lente pone esta tenue emisión al alcance de observatorios de nueva generación como el *Karl G. Jansky Very Large Array* (VLA) y el *extended Multi-Element Remote Linked Interferometer* (e-MERLIN). Además, no se sabe muy bien si a esas bajas luminosidades la emisión de radio proviene de chorros de materia relativista o bien es debida a la formación estelar u otros mecanismos, y este tipo de observaciones son necesarias para discernir entre las distintas posibilidades.

Se observaron cuatro sistemas con el VLA en octubre y noviembre de 2012: HE 0435–1223, RX J0911+0551 y SDSS J0924+0219 en el rango de frecuencias 4488-6512 MHz (banda C), y HS 0810+2554 en el rango 7988-10036 MHz (banda X) para obtener la mayor resolución que requiere este sistema debido a la menor separación de sus imágenes. Todas estas observaciones tuvieron lugar en la configuración A del VLA, que alcanza una distancia máxima entre antenas de 36 km y permite obtener resoluciones teóricas de $0\farcs35$ a 5 GHz y $0\farcs22$ a 8.4 GHz. Además, HS 0810+2554 y RX J0911+0551 se observaron también con e-MERLIN en 2014 en el rango 1287-1799 MHz (banda L). Todos los objetos fueron detectados, y los cocientes de flujo entre las imágenes múltiples del quásar pudieron medirse para todos ellos excepto SDSS J0924+0219.

Una vez procesados, los datos se ajustan a modelos de tipo SIE + γ (excepto HE 0435–1223) asumiendo primero que las imágenes múltiples del quásar son puntuales, y repitiendo luego el ajuste modelando la fuente como un perfil gaussiano elíptico que dará lugar a imágenes extensas tras ser afectada por la lente. Los modelos de la distribución de masa se ajustan comparando las imágenes resultantes de sus configuraciones con los datos observados, y variando sus parámetros hasta minimizar las diferencias.

En el caso de HS 0810+2554, la fuente es claramente extensa, con un tamaño físico de unos 70 pársecs, y no se detecta la gran anomalía de flujo observada en este sistema en el óptico, que podría deberse a microlensing. Las observaciones de e-MERLIN permiten además obtener el índice espectral de la fuente, que es moderadamente pronunciado, de $\alpha = -0{,}55 \pm 0{,}1$.

En HE 0435−1223 no se observan indicios de fuente extensa más allá de 2σ, pero sus cocientes de flujo difieren significativamente de los obtenidos con observaciones previas en infrarrojo medio. Además, son difíciles de reproducir con modelos sencillos consistentes en un perfil de masa de ley de potencias más *shear* externo y una esfera singular isoterma (SIS) en la posición de una galaxia cercana, incluyendo los retardos temporales medidos entre cada imagen del quásar para constreñir el ajuste. Es posible reproducir los flujos si se incluyen subhalos en el ajuste y afectan a la imagen D, dando como resultado una elipticidad $e \approx 0{,}33$ y un perfil de densidad más pronunciado que el isotermo con

exponente $\gamma' \approx 2{,}33$. Alternativamente, si se considera una fuente extensa, se reproducen los flujos con un tamaño para ésta de 80 milisegundos de arco o menor, y dando como resultado $\gamma' = 2{,}00^{+0,08}_{-0,06}$, consistente con un perfil isotermo. Posiblemente esta última explicación sea la correcta, dado que además se requerirían diferentes tamaños para la fuente en radio e infrarrojo medio para reproducir las diferencias entre los cocientes de flujo en ambas longitudes de onda.

RX J0911+0551 se detecta con el VLA pero no con e-MERLIN, lo que implica un límite inferior para el índice espectral de $\alpha = -0{,}5$. Sus cocientes de flujo son consistentes con los predichos por un modelo SIE + γ para la lente, y si se asume una fuente extensa, su tamaño no puede constreñirse bien aunque se situaría en torno a $\sim$1 kpc. No obstante, el buen ajuste en general a los datos muestra que no hay evidencia significativa de subestructura en la galaxia lente. Este sistema es el único de los cuatro en el que la galaxia lente se detecta en radio, con una luminosidad en el límite superior de lo que puede atribuirse a la formación estelar, y cerca del límite entre fuentes emisoras de radio debido a la formación estelar y debido a un núcleo activo en la galaxia.

El sistema SDSS J0924+0219 se observó durante menos tiempo, y debido a ello no se obtiene una señal suficientemente superior al ruido para medir los flujos de las imágenes del quásar por separado, y es de lejos el más tenue de los cuatro objetos estudiados.

Los índices espectrales medidos en las emisiones en radio son consistentes tanto con la presencia de formación estelar en la fuente como con una versión en miniatura de los chorros relativistas que producen la emisión en radio en quásares que brillan intensamente en esas longitudes de onda. Los tamaños observados para las fuentes, no obstante, son más pequeños de lo que se esperaría si se debiese a formación estelar, puesto que en principio ésta se encontraría repartida en buena parte del disco galáctico, extendiéndose unos 5-10 kpc. Sin embargo, no se puede afirmar todavía que una de las posibilidades se haya descartado como mecanismo debido al bajo número de objetos observados.

Capítulo 5

Como se ha explicado en secciones anteriores, la presencia de subestructura en los halos de materia oscura de las galaxias en forma de subhalos, predicha por las simulaciones cosmológicas, puede estudiarse si se dispone de los cocientes de flujo verdaderos entre las imágenes múltiples de un quásar creadas por una lente gravitacional. Estos flujos deben estar libres de los efectos de posible extinción diferencial debida al medio interestelar de la galaxia lente, y provenir de regiones del quásar lo suficientemente grandes como para que el microlensing debido a las estrellas de la galaxia apenas afecte a su brillo total. Hay tres regiones de un quásar que cumplen estos requisitos: el toroide de polvo, que emite en infrarrojo medio (mid-IR); la región de líneas estrechas (NLR), que emite líneas espectrales en el óptico e infrarrojo cercano; y los chorros de materia relativista, de darse, que

emitirían en ondas de radio (aunque la emisión en radio también puede provenir de otras fuentes como la formación estelar en la galaxia que hospeda el quásar). La emisión en mid-IR y en radio es prácticamente inmune a la extinción, y ésta afecta al mismo tiempo tanto a la luz de las líneas estrechas como al continuo sobre el que se mide su intensidad, de modo que en este último caso puede compensarse su efecto.

Para este estudio compilamos una muestra de sistemas cuyos cocientes de flujo han sido obtenidos mediante observaciones en esas longitudes de onda, y que dispongan de cuatro imágenes múltiples del quásar, para que modelos simples de la distribución de masa en la galaxia lente queden bien constreñidos utilizando sólo las posiciones de las mismas. Así, los cocientes de flujo observados podrán compararse con los predichos por los modelos de la distribución de masa sin que hayan sido utilizados para predecir estos últimos. Estos modelos son del tipo SIE + γ o bien SIE + γ + SIS en la mayoría de casos. Nuestra muestra observacional está formada por B 0128+437, MG 0414+0534, HE 0435−1223, B 0712+472, RX J0911+0551, SDSS J0924+0219, PG 1115+080, RXS J1131−1231, B J1422+231, B 1555+375, B 1608+656, WFI J2033−4723 y Q 2237+0305.

Una vez compilada la muestra, se usan los parámetros del potencial gravitatorio en las posiciones de las imágenes de los quásares (dados por los modelos) para generar mapas de magnificación que representan los efectos producidos por una distribución concreta de subhalos de materia oscura. Los parámetros de la distribución son la masa de cada subhalo, definida por su radio de Einstein b, y su abundancia, expresada como la fracción α de la densidad superficial de masa contenida en estos satélites. El tamaño aproximado de la fuente se tiene en cuenta estableciendo el tamaño del píxel con esa escala, y para cada conjunto de parámetros la magnificación producida por los subhalos en cada posible posición de la fuente se restará de la magnificación teórica del modelo simple en esa región, se pasará el resultado a magnitudes, y se calculará la distribución de probabilidad (PDF) con la que dicha distribución de subhalos provocaría en la imagen del quásar una anomalía de cada magnitud concreta. El número de mapas generados para cada conjunto de parámetros puede ser elevado para obtener mejor estadística. Una vez se tengan PDFs para todo el rango escogido de b y α en las cuatro imágenes del quásar en un sistema, se combinan para hallar la probabilidad de que con un par de parámetros concreto se reproduzcan los cocientes de flujo observados en ese sistema.

Para un análisis preliminar, asumimos que el tamaño de la fuente es de 1000 días luz en todos los casos, que los perfiles de masa ajustados a las posiciones de las imágenes de los quásares describen bien la distribución de masa de las galaxias lente en ausencia de subhalos, y que los cocientes de flujo observados no están afectados por ningún otro fenómeno. Entonces calculamos las distribuciones de probabilidad para todos los sistemas excepto RX J0911+0551, SDSS J0924+0219 y B 1555+375,y tras eliminar B 1608+656 y WFI J2033−4723, que seguramente predicen abundancias elevadas de subhalos porque

los modelos de masa usados no son apropiados, se combinan los resultados de los ocho sistemas restantes y se obtiene una estimación de la abundancia promedio $\alpha = 0{,}075^{+0{,}030}_{-0{,}021}$, y un valor medio del radio de Einstein de los subhalos $b = 0\farcs0003^{+0{,}0005}_{-0{,}0002}$, que corresponde aproximadamente con $10^6\,\mathrm{M}_\odot$.

La abundancia de subhalos obtenida es mayor que la predicha por simulaciones de CDM, pero aún marginalmente compatible a 2σ. Se debe tener en cuenta que para este estudio se asumió que las galaxias están bien modelizadas con perfiles SIE + γ (+ SIS), y que los cocientes de flujo no están afectados por sistemáticos, extinción, microlensing u otras perturbaciones. Todos estos factores podrían llevar a una sobrestimación de las anomalías, de modo que el valor obtenido debería ser tomado solamente como un límite superior. Trabajo futuro con modelos de masa más detallados y una muestra más amplia de sistemas ayudará a constreñir los valores reales de la fracción de masa que permanece como subhalos en los halos de materia oscura de las galaxias.

Conclusiones

Nuestras observaciones de sistemas lente en las que una galaxia produce cuatro imágenes diferentes de un mismo quásar han permitido tanto estudiar propiedades de los quásares en sí como de la distribución de masa en la galaxia lente. Se ha podido estimar el tamaño del disco de acreción del quásar Q 2237+0305 en un valor consistente con otros estudios y mayor que la predicción teórica (lo que podría llevar a la necesidad de invocar mecanismos físicos extra para explicarlo), y un perfil de temperaturas más pronunciado que en el modelo estándar de disco delgado pero consistente a 1σ con el valor predicho. Además de servir de base para separar los efectos de macrolensing y microlensing en la lente, nuestros flujos en mid-IR han permitido realizar una estimación del tamaño mínimo del toroide de polvo del quásar, y también de la proporción de la densidad de masa superficial que debería permanecer en forma de subhalos de materia oscura para reconciliar las observaciones con la predicción de modelos sencillos de la distribución de masa en el sistema.

Las observaciones en radio de HS 0810+2554, HE 0435−1223, RX J0911+0551 y SDSS J0924+0219 no han mostrado indicios de anomalías de flujos causadas por subhalos de materia oscura, explicándose de forma más coherente asumiendo que la emisión proviene de una fuente extensa. Dado que la magnificación de las lentes nos permite detectar emisión en radio de sistemas que no son luminosos a estas longitudes de onda, podemos empezar a discernir por qué mecanismo se emite, algo que aún no está claro en estos objetos. Los índices espectrales medidos son consistentes con jets relativistas pequeños o formación estelar en la galaxia en la que se sitúa el quásar, pero el tamaño medido para las fuentes es menor de lo que se esperaría si el segundo mecanismo fuera el causante, aunque más trabajo futuro es necesario para resolver esta cuestión.

Finalmente, desarrollamos un método para calcular la abundancia y tamaño de subhalos de materia oscura que serían necesarios para reproducir las anomalías de flujo observadas en infrarrojo medio, ondas de radio y líneas espectrales en el óptico en una muestra de sistemas lente. En un estudio preliminar obtenemos valores algo superiores a las predicciones teóricas en simulaciones de CDM, aunque todavía marginalmente compatibles a 2σ. La posible sobreestimación de las anomalías debida a modelos de masa demasiado simplificados para los sistemas, o un estudio más exhaustivo para los tamaños de la fuente considerados, serán tenidos en cuenta en un futuro trabajo para mejorar estos resultados preliminares.

Chapter 1

Introduction

Pushing the limits of knowledge is hard, and often requires extracting the largest possible amount of information from data that current technology has barely made available, from a still blurry new window to the universe that was not accessible before. So, when the universe itself conspires to provide us with a way to circumvent our technological limitations, to see further or in more detail than would be possible otherwise, we readily accept it and start figuring out how to use this phenomenon to obtain the best scientific results. Such is the case with gravitational lensing, which turns whole galaxies and galactic clusters into cosmic telescopes that help us see more clearly into what lies beyond. This bending of the paths that light follows across the Universe has become our main probe into effects caused by gravity alone, allowing us to gather insights into the nature of an unknown but abundant kind of matter that does not seem to interact by any other means. The exquisite sensitivity of the effect to the presence of mass has led to the discovery of wandering planets and whole star systems that were never seen before and will probably never be seen again, and has been used to reconstruct the structure of distant objects way beyond the limit of the best resolution we can currently achieve.

In this PhD thesis we use gravitational lensing to study both the properties of the central regions of quasars and similar active galactic nuclei, and the mass distribution of dark matter in galaxies. We will therefore begin by explaining gravitational lensing, and then we will give some details about the other two astrophysical phenomena.

1.1 Gravitational lensing

Mass curves space-time, and this curvature is what we call "gravity". That phrase roughly summarizes one of the main results of Einstein's theory of General Relativity, that describes gravitational interactions in a way that matches all the observations so far. In it, light propagates by following geodesic curves in space-time (a four-dimensional entity

in which time is just one more dimension), that are not necessarily the shortest distance when we only take into account its trajectory in three-dimensional space. Instead, light rays move following the space-time curvature created by gravity, and mass aggregations make light deviate from what would otherwise be a straight path. The bending of light by gravity was already predicted more than 200 years ago by Johann Georg von Soldner (*Soldner* 1804) using Newtonian physics and assuming that light was made of particles, but his theoretical prediction for the angle of deflection by a given amount of mass was only half that of the correct value. The same thing happened to Albert Einstein when using the equivalence principle and assuming the metric of space-time is Euclidean (not affected by gravity) (Einstein 1911), until he improved his own calculations when he developed the General Relativity (Einstein 1915). In fact, the measurement of the bending of light from stars close to the edge of the Sun during an eclipse in 1919 was the first experimental confirmation of his theory and sprang his jump to global fame. Since then, research in gravitational lensing has become increasingly important in astrophysics.

Since it is an effect that only depends on the distribution of mass in space, this phenomenon is a magnificent tool to study the structure of clusters and galaxies in the universe (providing important information about dark matter) and also compact objects, like for example extrasolar planets and other massive, low luminosity objects in the disk and halo of our galaxy. Furthermore, the distortion that the lens creates in the image of the source object can provide information about it or even make some objects detectable that would otherwise be too faint to be seen, and thus increase the limits of what is possible to study with our current instrumentation.

1.1.1 Basic equations

Because the observer-lens and source-lens distances are in general much larger than the thickness of the distribution of mass acting as gravitational lens, this is normally approximated as a thin lens, by projecting its three-dimensional density distribution $\delta(\boldsymbol{r})$ to calculate its surface density $\Sigma(\boldsymbol{\xi})$, where $\boldsymbol{\xi}$ is the distance vector in the lens plane (Narayan & Bartelmann 1997). Figure 1.1 shows a diagram with all relevant distances and angles in this approximation. In it, $\hat{\alpha}$ is the angle with which light from a point S in the source plane is deflected by the lens (that is, the deflection angle). β is the angle from the origin of coordinates (which is arbitrary) at which the observer (O) would see that point of the source plane if it wasn't affected by the lens, and θ is the one at which its image (I) is observed. D_{LS} and D_{OL} are the distances from the source to the lens and from the lens to the observer, respectively, while D_{OS} is the distance from the source to the observer. It is important to keep in mind that these are angular diameter distances in cosmology[1], so in general $D_{OS} \neq D_{LS} + D_{OL}$.

[1]Due to the expansion of the universe, objects at cosmological distances are seen with light that was emitted when they were much closer to us, so that their apparent angular diameter is larger than the

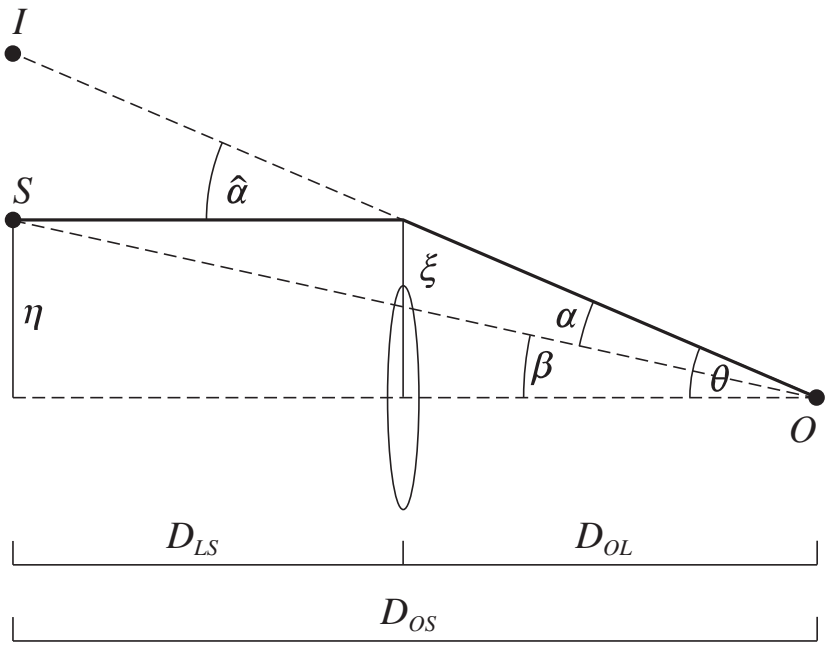

Figure 1.1 Relevant angles and distances in gravitational lensing.

From this we can obtain the lens equation, that establishes the relationship between the angular positions of the source and its corresponding image depending on the deflection angle

$$\boldsymbol{\beta} = \boldsymbol{\theta} - \frac{D_{LS}}{D_{OS}}\hat{\boldsymbol{\alpha}}. \tag{1.1}$$

The deflection angle of light that passes through position $\boldsymbol{\xi}$ is the sum of the deflections due to all the mass elements in the lens plane:

$$\hat{\boldsymbol{\alpha}}(\boldsymbol{\xi}) = \frac{4G}{c^2}\int \frac{(\boldsymbol{\xi} - \boldsymbol{\xi}')\Sigma(\boldsymbol{\xi}')}{|\boldsymbol{\xi} - \boldsymbol{\xi}'|^2} d^2\boldsymbol{\xi} \tag{1.2}$$

In the special case of a lens with circular symmetry, the axis of coordinates can be the axis of symmetry and the problem is reduced to one dimension. The deflection angle

one that would correspond to an object of the same size located now at the actual distance the light has traveled to reach us. The angular diameter distances correct for this effect and allow us to work using simple trigonometry in our calculations.

points then towards the axis, and its modulus is

$$\hat{\alpha}(\xi) = \frac{4GM(\xi)}{c^2\xi}, \tag{1.3}$$

where ξ is the distance from the center of the lens and $M(\xi)$ is the mass enclosed inside the radius ξ. The deflection can be expressed as a function of the angle θ by just taking into account that $\xi = D_{OL}\theta$. Thus, the reduced deflection angle, $\boldsymbol{\alpha} = (D_{LS}/D_{OS})\hat{\boldsymbol{\alpha}}$, can be written as:

$$\alpha(\theta) = \frac{D_{LS}}{D_{OL}D_{OS}}\frac{4GM(\theta)}{c^2\theta}. \tag{1.4}$$

If the lens has a constant surface mass density, the mass enclosed inside the radius θ could be calculated as $M(\theta) = \Sigma\pi(D_{OL}\theta)^2$ and we can define a critical surface density:

$$\Sigma_{cr} = \frac{c^2}{4\pi G}\frac{D_{OS}}{D_{OL}D_{LS}}. \tag{1.5}$$

A lens with $\Sigma > \Sigma_{cr}$ anywhere is said to be *supercritical*, and the source is multiply imaged usually when this condition is met, with some exceptions.

Let's now consider a supercritical lens with circular symmetry. Here, the image of a lens located exactly in the optical axis ($\beta = 0$) will be a ring due to the axial symmetry of the lens, and the radius of that ring is known as *Einstein radius*. From equations (1.1) and (1.4) its value can be obtained:

$$\theta_E = \sqrt{\frac{4GM(\theta_E)}{c^2}\frac{D_{LS}}{D_{OL}D_{OS}}}. \tag{1.6}$$

The Einstein radius provides a natural angular scale to describe the lensing geometry, because in the case of multiple images the separation between them is of the order of $2\theta_E$. Also, a source located at a distance from the optical axis smaller than the Einstein radius will experience significant magnification while for larger distances it will be lower. By comparing equations (1.5) and (1.6) we can also see that the average surface density inside the Einstein radius is precisely Σ_{cr}.

In order to study lenses with more complex density profiles, we can define a scalar potential $\psi(\boldsymbol{\theta})$ that consists of the newtonian potential scaled and projected onto the lens plane, and is called *effective lensing potential*. The gradient of ψ with respect to θ is the deflection angle,

$$\vec{\nabla}_\theta\psi = \boldsymbol{\alpha}, \tag{1.7}$$

its Laplacian is proportional to the surface mass density Σ,

$$\nabla^2_\theta \psi = 2\frac{\Sigma(\boldsymbol{\theta})}{\Sigma_{cr}} \equiv 2\kappa(\boldsymbol{\theta}), \tag{1.8}$$

and $\kappa(\boldsymbol{\theta})$ is the *convergence*, defined as the surface mass density scaled to the critical value.

The local properties of the mapping created by the lensing are described by its Jacobian matrix $\mathcal{A}$,

$$\mathcal{A} \equiv \frac{\partial \boldsymbol{\beta}}{\partial \boldsymbol{\theta}} = \left(\delta_{ij} - \frac{\partial \alpha_i(\boldsymbol{\theta})}{\partial \theta_j}\right) = \left(\delta_{ij} - \frac{\partial^2 \psi(\boldsymbol{\theta})}{\partial \theta_i \partial \theta_j}\right) = \mathcal{M}^{-1}. \tag{1.9}$$

$\mathcal{A}$ is the inverse of the magnification tensor $\mathcal{M}$, that describes how the image of the source is magnified or demagnified by the lensing. The distortion that a solid angle element $\delta\beta^2$ of the source suffers when mapped into the solid angle element $\delta\theta^2$ of the image, and therefore its magnification, is given by the determinant of $\mathcal{A}$:

$$\frac{\delta\theta^2}{\delta\beta^2} = det\mathcal{M} = \frac{1}{det\mathcal{A}}. \tag{1.10}$$

Equation (1.9) shows that the matrix of second derivatives of the potential describes how the mapping produced by the lens under study differs from an identity. We can abbreviate the second derivatives as

$$\frac{\partial^2 \psi}{\partial \theta_i \partial \theta_j} \equiv \psi_{ij}, \tag{1.11}$$

and because the Laplacian is twice the convergence, the convergence then is:

$$\kappa = \frac{1}{2}(\psi_{11} + \psi_{22}). \tag{1.12}$$

Two other important linear combinations of ψ_{ij} are the components of the *shear* tensor,

$$\begin{array}{rcl} \gamma_1(\boldsymbol{\theta}) & = & \frac{1}{2}(\psi_{11} - \psi_{22}) \equiv \gamma(\boldsymbol{\theta}) cos[2\phi(\boldsymbol{\theta})], \\ \gamma_2(\boldsymbol{\theta}) & = & \psi_{12} = \psi_{21} \equiv \gamma(\boldsymbol{\theta}) sin[2\phi(\boldsymbol{\theta})]. \end{array} \tag{1.13}$$

The Jacobian matrix can now be written as

$$\begin{array}{rcl} \mathcal{A} & = & \begin{pmatrix} 1-\kappa-\gamma_1 & -\gamma_2 \\ -\gamma_2 & 1-\kappa+\gamma_1 \end{pmatrix} \\ & = & (1-\kappa)\begin{pmatrix} 1 & 0 \\ 0 & 1 \end{pmatrix} - \gamma \begin{pmatrix} cos2\phi & sin2\phi \\ sin2\phi & -cos2\phi \end{pmatrix}, \end{array} \tag{1.14}$$

where we can see the meaning of the convergence and shear terms. The convergence produces an isotropic magnification of the source, altering its size but not its shape,

and shear introduces an anisotropy (astigmatism) in the mapping. The quantity $\gamma = (\gamma_1^2 + \gamma_2^2)^{1/2}$ describes the magnitude of the shear and ϕ its orientation. Therefore, a circular source of radius 1 affected by shear would become an elliptical image whose major and minor semiaxes would be $(1 - \kappa - \gamma)^{-1}$ and $(1 - \kappa + \gamma)^{-1}$. The magnification of the image is:

$$\mu \equiv \frac{\text{Area of the image}}{\text{Area of the source}} = det\mathcal{M} = \frac{1}{det\mathcal{A}} = \frac{1}{(1-\kappa)^2 - \gamma^2}. \tag{1.15}$$

When the lens does not have circular symmetry (for example, when its potential is elliptical or caused by an irregular set of mass distributions) new pairs of images of the source can appear. If we graph the positions of the source plane in which, when crossed by the source, a new pair of images of it would appear or disappear (which correspond to the places in the mapping where magnification would be infinite, something theoretically possible as seen in equation (1.15)), we obtain curves called *caustics* (Kochanek 2004a). An example of caustics can be seen in Figure 1.3, and we will talk about them more in the following subsections.

1.1.2 Strong lensing

There are cases, generally when the lens is supercritical, in which light from the source can reach the observer from separate paths around the lens, therefore creating multiple images of it. When observed, these multiple images can provide a lot of information about the mass distribution in the gravitational lens in several different ways. The main observational constraints when determining the shape of the lensing potential are the positions of the lensed images, the flux ratios between them, and in the case of a variable source, the time delays with which we see the variability in each of the lensed images. With current instrumentation, we can only resolve separate images of a single source when the gravitational lens is a galaxy or a galaxy cluster (since they have enough mass to for their Einstein radii to be larger than 1 arcsecond), and this subset of cases is designated by the term *macrolensing*.

Aside from the two-image configurations typical of lenses with circular symmetry when the angular distance from the source to the center of the lens is sufficiently small, extra pairs of images can be produced when the structure of the lens is less regular. For example, if the lens becomes elliptical or an external shear is applied, a caustic in the shape of an astroid is created on the source plane at the location of the lens center. If a point source is located inside this caustic, four lensed images will be observed (plus a fifth one with a high demagnification, depending on the particular surface density profile of the lens). The positions of these images for a given lens potential will depend on the exact

location of the source within the caustic, with pairs of images merging if the source is close to or touching the edges of the caustic itself.

The image positions are the most reliable observational probe when constraining the gravitational potential of a galaxy, because we can achieve relatively low uncertainties and they are not subject to a lot of confounding effects that could mask their "true" locations. However, more information about the mass distribution on the lens can be obtained if we also include the flux ratios of the lensed images in the modeling. The image positions are given by the deflection angles and therefore depend on the first derivative of the effective lensing potential, as explained in the previous section. Meanwhile, the magnification of each lensed image depends on the second derivative of the potential, so their flux ratios are more sensitive to the particular distribution of the mass in the lens plane. Precise measurements of the fluxes can be used to constrain models with a higher number of parameters, or even probe for the presence of extra substructure in the lens that would not have been included in a smooth model.

1.1.3 Microlensing

When the mass of the lenses is very low, the angular separation between multiple images of the source can be too small to be seen with our current instrumentation. However, despite our lack of resolving power, the lensing can still have a measurable effect. Since the image distortions will still be there, the angular area of the observed image will be different than the area of the source, and due to this magnification we will see an unresolved object with a flux that is different from the one it would have with no lensing. If there is a relative displacement between the source and the lenses over time, we can then see brightness changes on the source due to lensing. This phenomenon is usually observed when the lenses are compact objects like stars or planets, and since the separation of the multiple images in this case would be on the order of microarcseconds, it is known as *microlensing*.

An array of microlenses creates a distribution of caustics in the source plane, that can be thought of as lines (or very thin regions) of high magnification. Were the source to cross one of these, a very noticeable 'high magnification event' would occur. As explained in previous sections, a source located very close to a caustic has merging pairs of lensed images, and so the images are very stretched and elongated. It is this high ratio between the area of the image and the area of the source that corresponds to the high magnifications.

1.1.3.1 Chromaticity

For the images of the source to be elongated, we cannot have a perfect point-like source, but an object with a certain size. In some cases the source will be a background star, so the lensed images will still be small, but sometimes the lensed object can have a size comparable to the projected Einstein radius of the lenses, and this will have observable consequences. If the microlensed source is big, we can have cases in which only part of the source enters a high magnification region, and only a fraction of its brightness becomes magnified. If the source is on a trajectory that goes through a region of caustics, the lightcurve when monitoring its brightness will be smoother than what a much smaller object would produce—the high magnification events will not be as high, and otherwise rapid changes in magnification will be averaged out, with only the general trends still remaining. The light curve of the observations will effectively be convolved with the brightness profile of the source, and thus this phenomenon can be used to deduce its size. Some astronomical objects consist of several components of different sizes, and if we are lucky enough that they also emit light in different wavelengths, we can use microlensing to study them further. Since their apparent size will be different when observed with different filters, they will not be microlensed in the same way. This phenomenon, known as *chromatic microlensing*, can be very useful to study the temperature profile in lensed accretion disks (with hotter regions emitting at shorter wavelengths), and also allows us to disentangle macrolensing effects from microlensing by observing the system at wavelengths emitted from regions of the source that are too large to be noticeably microlensed.

1.1.3.2 Generating magnification maps

A magnification map describes the magnification that a point source would suffer at each position of the source plane after lensing by a mass distribution in the lens plane. To calculate this, the common procedure consists of dividing into cells the region of the source plane that we are interested in, shooting towards it light rays through the lens plane that will be deflected by the lensing mass distribution, and counting how many of these rays reach each cell of the source plane. This technique is known as *inverse ray shooting* (IRS), and is a simple way of mapping the lens plane onto the source plane. Each ray is representative of a certain amount of area in the lens plane, so that when a cell receives several rays at its location, it means the lens image of that particular cell will be stretched over an area equal to the sum of the areas represented by each ray. If the angular area of the cell in the source plane is smaller than the total area of the rays from the lens plane that reached it, it means it will be magnified. If larger, the cell will be demagnified by the lensing. The cells in the source plane will become the pixels of the magnification map and their size will determine the resolution at which we sample the resulting caustics, so it is important to choose a size small enough for the source considered in each case.

When generating magnification maps for the multiple images of a lensed quasar (section 1.2.3), we have to take into account the convergence and shear due to the potential of the lens galaxy in each region. The calculation can be simplified by choosing a set of coordinates in the lens galaxy so that the orientation of the shear coincides with one of the sides of the map, which would correspond to $\phi = 0$ in equation (1.14). This way, we avoid the presence of diagonal terms that would needlessly complicate the calculations.

Another simplification would be the use of the Einstein radius as a scale for the magnification maps. This also makes the maps independent both from the distances between source, lens and observer, and the mass scale of the lenses used if they are point-like. The coordinates used, then, would be $\boldsymbol{y} = \boldsymbol{\beta}/\theta_E$ for the angular distances in the source plane, and $\boldsymbol{x} = \boldsymbol{\theta}/\theta_E$ for the lens plane. For a set of point-like lenses, from equations (1.1), (1.2), and (1.4), the lens equation would then be:

$$\boldsymbol{y} = \boldsymbol{x} - \frac{D_{LS}}{D_{OL}D_{OS}}\frac{4G\mathrm{M}_\odot}{c^2}\sum_{i=1}^{N} m_i \frac{\boldsymbol{\theta} - \boldsymbol{\theta}_i}{|\boldsymbol{\theta} - \boldsymbol{\theta}_i|^2\theta_E} = \boldsymbol{x} - \theta_E^2 \sum_{i=1}^{N} m_i \frac{\boldsymbol{x} - \boldsymbol{x}_i}{|\boldsymbol{x} - \boldsymbol{x}_i|^2\theta_E^2} \tag{1.16}$$

where we use a scale of one solar mass ($\mathrm{M}_\odot$), m_i is the fraction of one solar mass contained in the point lens i, an Einstein radius θ_E cancels out, and we use the following relations:

$$\frac{\boldsymbol{\theta}}{|\boldsymbol{\theta}|^2} = \frac{\boldsymbol{x}\theta_E}{|\boldsymbol{x}|^2\theta_E^2} = \frac{\boldsymbol{x}}{|\boldsymbol{x}|^2\theta_E}. \tag{1.17}$$

The magnification map for each quasar image is characterized by a κ and a γ that depend on the density profile of the lens galaxy and the image position. Since the convergence is given by the mass surface density, the individual lenses included in the lens plane must contribute to it. Thus, part of the convergence is due to the microlenses, $\kappa_\star$, and part to the smooth distribution of the rest of the mass in the lens galaxy, κ_c, such that $\kappa = \kappa_\star + \kappa_c$. The fraction of the convergence due to the microlenses can then be defined as $\alpha = \kappa_\star/\kappa$.

The effect of the smooth potential of the galaxy would be like the one described by equation (1.14), and can be added to expression (1.16). Thus, we have the complete equation for inverse ray shooting (Schneider et al. 1992) that describes the deflection each ray would suffer due to the combined effect of all the mass elements:

$$\boldsymbol{y}(\boldsymbol{x}) = \boldsymbol{x} - \sum_{i=1}^{N} m_i \frac{\boldsymbol{x} - \boldsymbol{x}_i}{|\boldsymbol{x} - \boldsymbol{x}_i|^2} - \begin{pmatrix} \kappa_c + \gamma & 0 \\ 0 & \kappa_c - \gamma \end{pmatrix} \boldsymbol{x}. \tag{1.18}$$

Given that the image plane as a whole will be distorted by κ and γ when mapped onto the source plane via ray tracing, it is useful to scale it properly so that no regions of the source plane are left where no rays arrived (that is, if the quasar image has become stretched by the lensing and we want to create a square map in the source plane, the area of the image plane where we shoot the rays cannot have the same shape and size, but has to be stretched in a similar way). To compute this compensation, we multiply the size of each dimension of the image plane by the inverse of the transformation applied by the IRS. If the magnification map is a square in the source plane, the size of its side is $size^S$, and the dimensions of the image plane after modifying its shape are $size_1^L$ and $size_2^L$, the operations to apply are:

$$\begin{aligned} size_1^L &= size^S/[1-(\kappa+\gamma)] \\ size_2^L &= size^S/[1-(\kappa-\gamma)] \end{aligned} \tag{1.19}$$

With this transformation, if the mass distribution was completely homogeneous (described only by κ and γ in the matrix of the IRS equation), the rays shot from the image plane would cover exactly the region of the source plane in which we want to generate the map. However, since part of the mass surface density is contained in microlenses with random $\boldsymbol{x}_i$ positions, border effects would occur if these are located only inside the shooting region instead of uniformly distributed in the whole image plane, and also because there would not be rays that, when shot from outside this region, would have ended up in the map after deflection by the lenses. To solve these problems, the dimensions of the area where the lenses are located and where the rays are shot from are multiplied by a factor (generally 1.5). Also, to prevent the effect of the distribution of lenses to have undesired anisotropies, this region will be a square instead of rectangular. This way, we will have a ray shooting region with a size equal to one and a half times $size_{max}^L$, the larger of the sides computed in Eq. 1.19. These transformations and the scaling of the shooting region are illustrated in Figure 1.2.

In this region we will place a random distribution of point masses that will represent the stars of the galaxy that microlens the quasar image. In this work, all stars in the magnification maps will have an equal mass $M = 1\,\mathrm{M}_\odot$, because then all distances can be expressed as a fraction of the Einstein radius so they can be scaled as $\sqrt{M/\mathrm{M}_\odot}$, and our results depend mainly on the mean mass of the microlenses instead of the actual mass function of the distribution of stars. The mass of the stars in this region comprises a surface density Σ that will be expressed as a fraction of the convergence, $\kappa_\star$. We can relate both quantities by expressing the critical surface density as a function of the Einstein radius r_E in the lens plane:

$$\Sigma_{cr} = \frac{c^2}{4\pi G}\frac{D_{OS}}{D_{OL}D_{LS}} = \frac{M}{\left(\sqrt{\frac{4GM}{c^2}\frac{D_{LS}}{D_{OL}D_{OS}}}\right)^2 D_{OL}^2\pi} = \frac{M}{\pi(r_E^L)^2}. \tag{1.20}$$

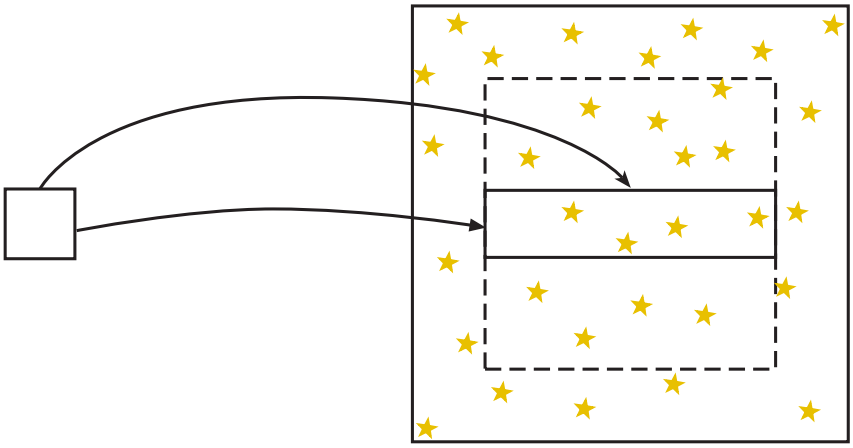

Figure 1.2 Mapping of the square source plane onto the image plane to generate a microlensing magnification map, and the surrounding shooting region with the uniform distribution of microlenses to avoid border effects.

When distances are normalized to the Einstein radius of a point-like lens of one solar mass, the critical density expressed in these units reduces to $\Sigma_{cr} = 1/\pi$. Then, the mass surface density of one solar mass stars will be just the number of them divided by the area of the region in units of square Einstein radii, and the corresponding convergence is:

$$\kappa_\star = \frac{\Sigma}{\Sigma_{cr}} = \frac{\pi n}{(1.5 \times size^L_{max})^2}. \tag{1.21}$$

Using this equation, we can easily obtain the necessary number of stars (n) to achieve the corresponding fraction of the convergence, $\kappa_\star$.

The angular resolution of the magnification map is given by the number of cells per Einstein radius in the source plane, and will be the same for the lens plane. However, the number of rays shot per cell in the lens plane can be increased to improve the precision on the magnification values obtained, and this option can be implemented by fractioning the amount of area of the lens plane that each ray represents when it reaches the source plane.

If the rays are shot from uniformly distributed positions, the caustics will be usually well sampled due to the high magnification and therefore the high number of rays per cell in those regions. However, the smooth areas with low magnification might present noise and irregularities due to a very gradual change in magnification having to be mapped with fewer rays per cell. Since these areas comprise most of the magnification map and therefore most of the light curve of a lensed image when not in a high magnification event, a good precision in the low magnification regions is needed. This can only be

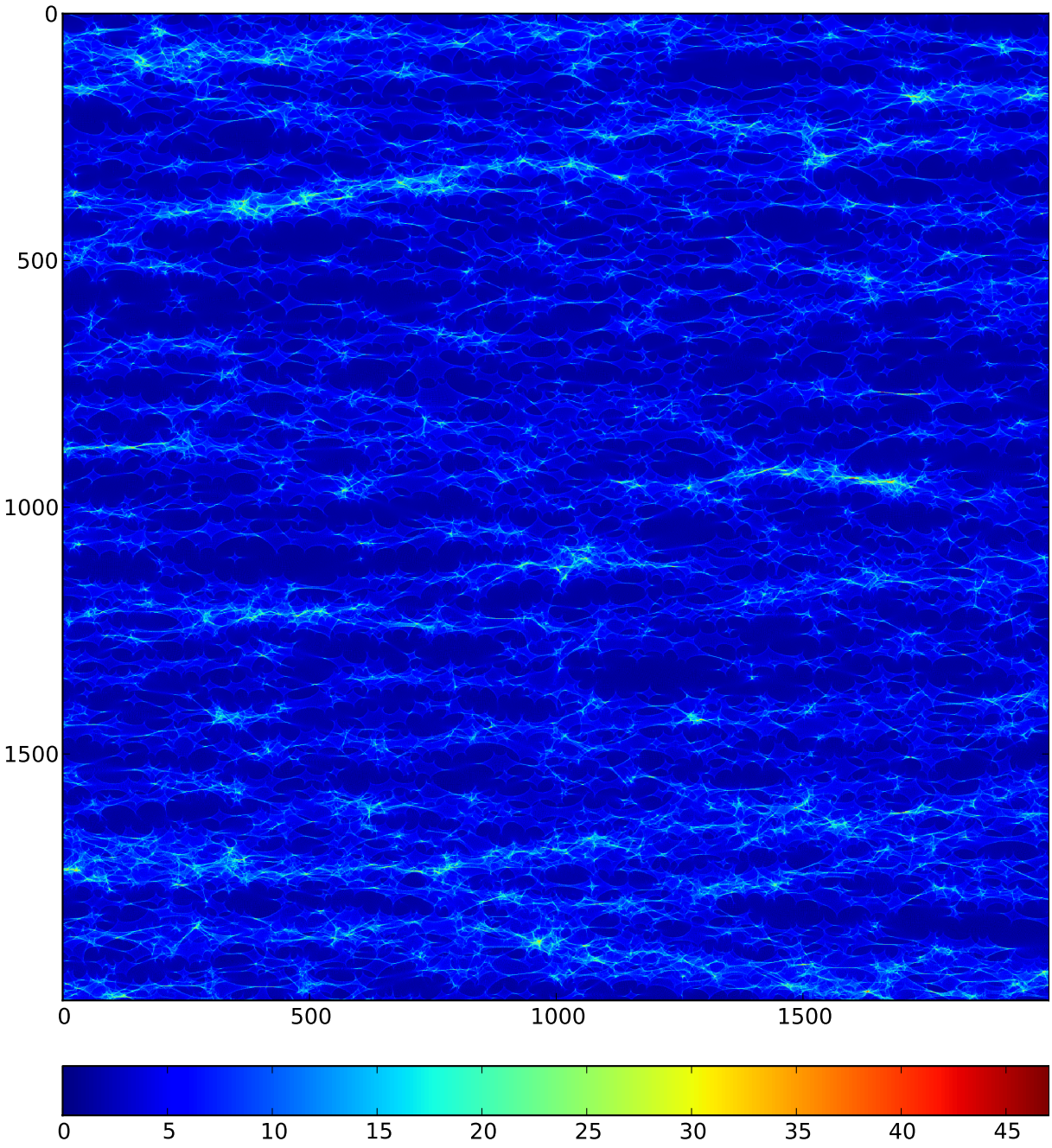

Figure 1.3 Microlensing magnification map for image A of the lensed quasar Q 2237+0305, with $\kappa = 0.36$, $\gamma = 0.40$, and $\kappa_\star = 1$. The map is 2000×2000 pixels in size, with 0.5 light-days pixel^{-1} in the source plane for stars with a mass $M = \mathrm{M}_\odot$.

achieved in IRS by shooting a larger number of rays representing a smaller area each, increasing the calculation times by a factor that could be quite high if large maps or many maps are required. Alternatively, we can use a slightly different technique called *Inverse Polygonal Mapping* (Mediavilla et al. 2006, 2011a). Here, the lens plane is also subdivided in rectangular cells but they are mapped onto the source plane by shooting rays from the vertices and center of each cell, that will be deflected like in the IRS procedure. In this case, however, the exact fraction of the area of a lens plane cell that falls within each source plane cell is computed when obtaining the magnification value, therefore increasing the precision for the low magnification areas without the need for a large number of additional ray shootings. The ray from the center of the lens plane cell helps determine if it is no longer a convex quadrilateral after the mapping, and in this case the cell will be subdivided further before being mapped onto the lens plane. These subdivisions happen at several hierarchic levels to ensure the caustics are well sampled. All magnification maps generated for this thesis are calculated using the Inverse Polygonal Mapping procedure. One of these maps can be seen in Figure 1.3.

1.2 Quasars

1.2.1 History

When first detected, quasars were just radio sources distributed on the sky, in an era where assigning an optical counterpart to them was still difficult. Radio astronomy was a young field in the 1950s, the instrumentation was still in early development, and the resolution of radio observations was low. However, in 1963 the objects 3C 273 and 3C 48 were matched to astronomical sources in optical wavelengths and their spectra could be obtained, becoming the first two astronomical bodies discovered with systemic redshifts greater than 0.1 (Hazard et al. 1963; Schmidt 1963; Oke 1963; Greenstein & Matthews 1963). The fact that the optical counterparts were point sources and looked at first like stars within our galaxy earned them the name "quasars" from a contraction of the designation *quasi-stellar radio sources*. However, their large redshifts (0.16 and 0.37, respectively) were puzzling and sparked some controversy about the nature of these objects. The possibility that these were gravitational redshifts was considered, but the presence of forbidden spectral lines set an upper limit to the gas density at the source, which was hard to believe it could remain stable in such a deep gravitational well. There were less objections to the interpretation of the redshift as cosmological, but in this case these sources would be so far away that their observed brightness required extreme optical luminosities for them, 10–30 times that of the brightest elliptical galaxy, and total emitted energies as high as 10^{60} ergs (Greenstein & Schmidt 1964).

Eventually, it was discovered that quasars were powered by the infall of matter in an

accretion disk towards supermassive black holes in distant galaxies (Lynden-Bell 1969), exchanging gravitational potential energy into kinetic energy and heating up enough to provide the extreme luminosities observed. It is now believed that supermassive black holes exist at the center of most galaxies (including our Milky Way), but many are in a quiescent state with very low accretion rates and therefore not displaying high luminosities. It is when they accrete large quantities of matter that they turn the center of the galaxy into an *active galactic nucleus* (AGN), and quasars are just one type of object powered by this phenomenon. Further observations have shown that only about 10% of these objects have strong radio emission, so the term *quasi-stellar object*, abbreviated 'QSO', was coined to include both the 'radio-loud' quasars and the 'radio-quiet' types. Over time, however, the term 'quasar' has become the default designation for both kinds of QSOs regardless of their amount of radio emission, and the preferred option is to specify if the object is radio-loud or radio-quiet only when relevant. Throughout this work, we will normally use the term 'quasars' to refer to QSOs in general.

Their abundance and incredibly powerful outputs have turned AGNs into very important targets for the study of accretion disks around supermassive black holes, but the compact size of these objects at great distances makes them unresolvable even in the local universe and many of their properties have to be deduced from their spectra only. It is here where gravitational lensing can play a role thanks to the sensitivity of phenomena like microlensing to the size and exact position of a small lensed source.

1.2.2 Structure

AGNs present a large diversity of observational features in many different wavelengths, and after decades of detailed study of relatively nearby ones, a much clearer picture has emerged of their structure and emission mechanisms. It is now understood that an active galactic nucleus is a galaxy that contains a supermassive black hole ($M_{BH} > 10^5\,\mathrm{M}_\odot$) that accretes matter with an Eddington ratio larger than $L_{\mathrm{AGN}}/L_{\mathrm{Edd}} = 10^{-5}$, where L_{AGN} is the bolometric luminosity and $L_{\mathrm{Edd}} = 1.5 \times 10^{38} M_{BH}/\mathrm{M}_\odot$ ergs^{-1} is the maximum luminosity it can achieve before the radiation pressure pushes the matter away from the black hole (although it can be exceeded in some cases) for a solar composition gas.

Since some observational features were shared by some of them and not others, these objects were separated in different classifications until a unified model was proposed to explain them all as observable changes when varying only the viewing angle and the source luminosity (Antonucci 1993; Urry & Padovani 1995; Urry 2003). These models have been modified and improved over the years (for a recent review on the current state of unification models, see Netzer 2015), but the picture they describe to explain the structure and emission mechanisms of AGNs still has many elements in common with the original. They are described below.

Accretion disk. The exchange from gravitational potential energy into kinetic energy in the matter accreting into the supermassive black hole is the main power source of the AGN. With a small size of only up to a few light-days across, it is extremely hot and luminous, and emits in a continuum from at least infrared wavelengths up to hard X-rays, and in some cases even gamma rays, getting hotter and emitting in shorter wavelengths the closer it gets to the center. This produces a broad peak in the optical/UV known as the "big blue bump" in the spectrum (Shields 1978). The regions of the accretion disk observable in optical wavelengths are usually modeled using the standard thin disk model by Shakura & Sunyaev (1973), in which the radial dependence of the surface temperature is obtained by equating the local radiation energy flux to the gravitational energy release. When the local spectrum of the thermal radiation is a Planck distribution, a law with the form $T \propto R^{-1/p}$ is obtained, with $p = 4/3$. This corresponds to a size scaling $R_\lambda \propto \lambda^p$ when defining R_λ as the radius at which the disk temperature matches the wavelength, using $kT(R_\lambda) = hc/\lambda$.

Broad line region (BLR). Surrounding the central area there is a region of hot gas that still travels very fast, larger than the accretion disk (up to tens of light-days across). Clouds of this gas, excited and ionized by the central engine, show permitted optical emission lines that are broadened by these speeds (FWHM > 1000 km s^{-1}). Since the density is still relatively high, no forbidden lines are present, so broad permitted emission lines are very characteristic of this region. Not all AGNs have these lines in their observed spectra, which led to their classification as type I or type II Seyfert galaxies, depending on whether they were present or not, respectively. Unification models propose the presence of optically thick structures, like the dusty torus, that can occult the BLR from certain viewing angles.

Narrow line region (NLR). Further away, reaching up to many parsecs, there is a much larger area of low pressure gas, colder and slower than in the BLR, but still excited and ionized by the central engine of the AGN. It is usually an outflow in the shape of a biconical region aligned with the axis of the dusty torus, and presents narrow emission lines in the optical, both permitted and forbidden in this case due to the lower pressures. It can also have emission in mid-IR wavelengths due to the presence of dust (Hönig et al. 2013).

Jets. Some AGNs also have a different kind of outflows, as relativistic jets of particles coming from the region closest to the black hole, and collimated by the magnetic fields originating in the innermost region of the accretion disk. Their total length can vary but is often far larger than their host galaxy, and terminate in lobes that are very visible in radio wavelengths due to synchrotron radiation. These jets can be are about 1000 times brighter in radio than the IR-UV continuum when they are present. However, 80–90% of

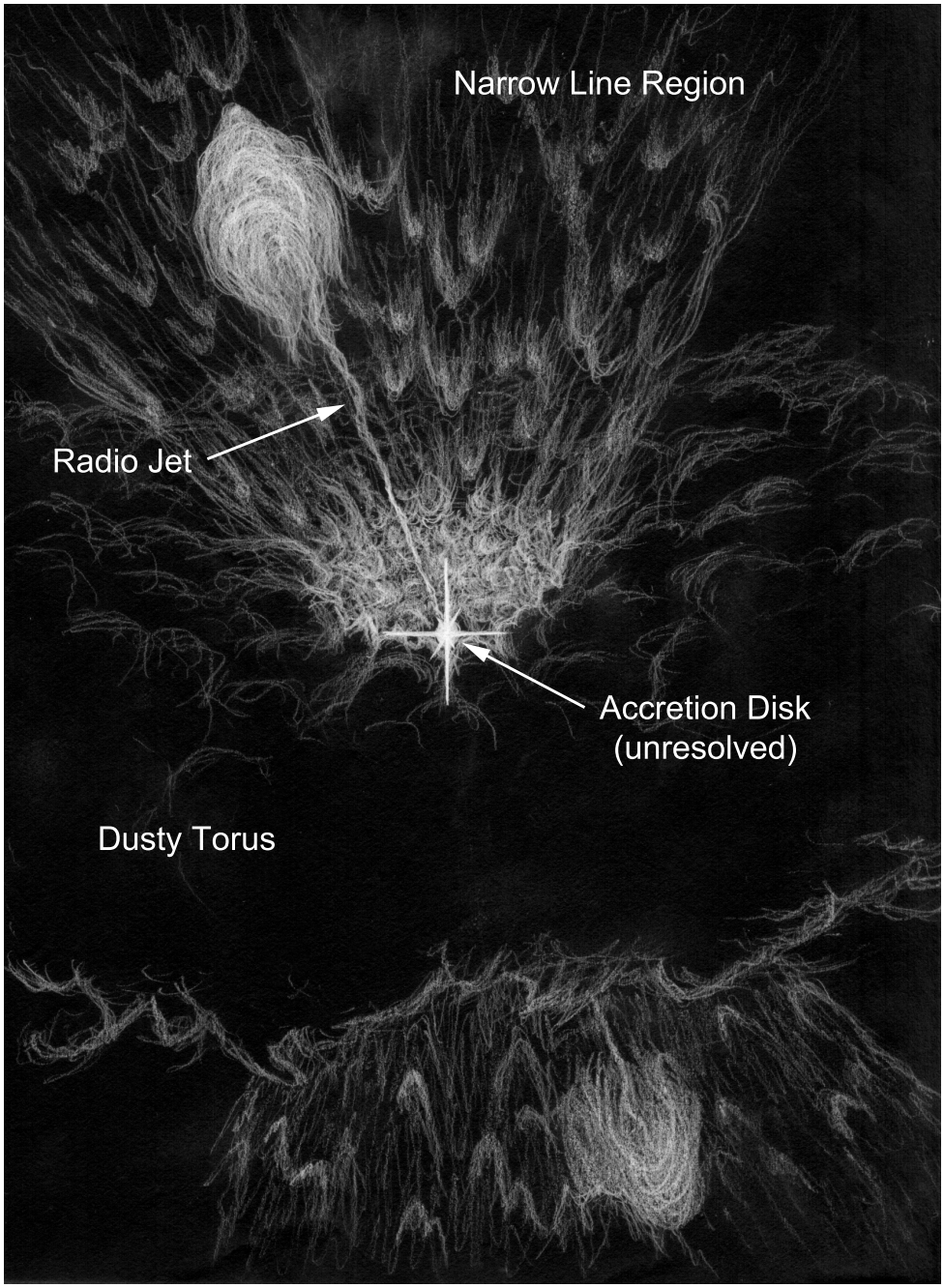

Figure 1.4 Artistic representation of the largest components of an active galactic nucleus. The dusty torus surrounding the central engine can be seen, as well as the biconical narrow line region. The radio jets are usually much larger than depicted, but were scaled down to be shown in this image. The accretion disk and broad line region are so small at this scale that they are unresolved.

all AGNs are radio-quiet, and the jets are the characteristic feature that distinguishes the radio-loud type.

Dusty torus. This optically thick structure was proposed in unification models to explain the difference between type I and type II Seyfert galaxies. The torus surrounds the accretion disk and the BLR, sometimes obscuring them, depending on the viewing angle. It is composed of warm dust heated by the AGN, so it has thermal emission with temperatures usually between 50 and 1000 K, and is visible in the spectra as a broad peak in the IR known as the "IR bump" (Sanders et al. 1989). Since dust cannot exist at temperatures higher than about 1000-1500 K, this means that for a simple thermal equilibrium, ignoring Planck factors, the inner radius of the torus is $r_{min} \simeq 730 L_{46}^{1/2} T_{d3}^{-2}$ light-days, where the luminosity of the AGN is $L = 10^{46}\ L_{46}$ erg s^{-1} and the destruction temperature is $T_d = 1000\, T_{d3}$ K. More recent observations have led to the conclusion that the obscuring structure is not always a torus, and even when it is the case, the torus is rather clumpy instead of uniform. The overall size of the torus can vary with the luminosity of the AGN (and sometimes even disappear altogether at low luminosities), and infrared interferometry using the MID-infrared Interferometric instrument (MIDI) at the Very Large Telescope has allowed to estimate the half-light radius $R_{1/2}$ of this mid-IR emission region to be in the range 0.1-10 pc (Burtscher et al. 2013).

1.2.3 Quasar lensing

Many of the known gravitational lenses are systems in which a galaxy is in the same line of sight as a much more distant quasar, generating typically two or four lensed images of it. The configuration of these systems allows us to gather information both from the distribution of the mass in the lens galaxy and the distant AGN itself, so they are incredibly useful astrophysical tools and the main object of study of this thesis. The reviews by Kochanek (2004a) and Schmidt & Wambsganss (2010) give a good description of the details and different applications of lensing in these systems.

As described in Section 1.1.2, the positions of the lensed images and their flux ratios can be used as constraints to model the mass distribution of the lens galaxy. Lensed quasars let us put this theory into practice in a fairly straightforward way due to their point-like appearance: the lensed images have to be mapped into a simple point source by the lensing potential of the model, their positions can be measured accurately, and their separate fluxes can be obtained even if the angular resolution of the observations is not very good (which can happen when using long wavelengths). However, a number of effects hinder this potential application. For example, differential extinction in the lens can alter the observed fluxes of some images more than others, or compact objects like stars in the lens could further magnify the images independently with their own gravitational microlensing effects. If we are interested in studying the overall potential of the lens

and not the population of compact objects or its extinction, these complications can be circumvented by observing the system in wavelengths that are immune to extinction from the interstellar medium, and/or emitted by regions of the source that are large compared to the Einstein radius of the compact objects themselves. As can be seen in the previous subsection, many of the different observational features of AGNs come from regions of different sizes, so in principle one can select which component of the AGN to use as source for the lensing in order to disentangle the microlensing and macrolensing magnifications. The largest regions of the AGN are the jets, the dusty torus, and the NLR, so for this goal the systems have to be observed in radio or mid-IR wavelengths, or we would need to obtain a spectra of each of the images in order to measure the narrow spectral lines in the optical or near-IR. Once we have the "true" flux ratios for a lens system, we can proceed to use them as constraints to model the mass distribution with simple models, or search for anomalies that could be indicative of substructure. When using radio observations, however, one must be careful because the size of the jet could be too large to have point-like lensed images, and after the lensing distortion they could have a resolvable structure in very long baseline interferometry (VLBI) observations. If this is the case, one can proceed as before by locating the core of the AGN in the radio map and using only the flux ratios of the center of the source, or use the whole jet structure as multiple point sources that provide extra information about the lens when applied as constraints. Of course, the fact that the structure of the jet becomes stretched and magnified means that we can learn more about the source itself thanks to the gravitational lens. In some cases, the magnification also makes the host galaxy of the quasar visible as an Einstein ring due to its extended nature. In these cases, each pixel of the extended source can also be used as an extra constraint because they sample the lens potential at a higher number of locations, or one could use the extra information to study the environment of the AGN itself.

But the magnification and stretching of the lensed images of extended components of the AGN are not the only way we can gather information about it using this type of lens systems—we can also obtain insights about the smallest regions and the central engine itself. Generally, the paths of light that will form the observed images go through some region of the lens galaxy, encountering part of the population of compact objects (like stars) that will induce microlensing of the smaller components of the AGN like the accretion disk and the BLR. This phenomenon can then be used to learn more about the accretion process and the inner regions of the AGN by obtaining estimates of their sizes as described in Section 1.1.3. However, there is a catch. The brightness of the accretion disk is not always constant, but it presents a certain variability that could be hard to distinguish from microlensing. It is here where the multiple images of the source play an important role, because any intrinsic variability will take place in all of them while microlensing affects each image independently. After obtaining light curves for all of the images, one could cancel out the intrinsic variability by working with their flux ratios instead. The problem is that since the paths the light takes for each image are not exactly

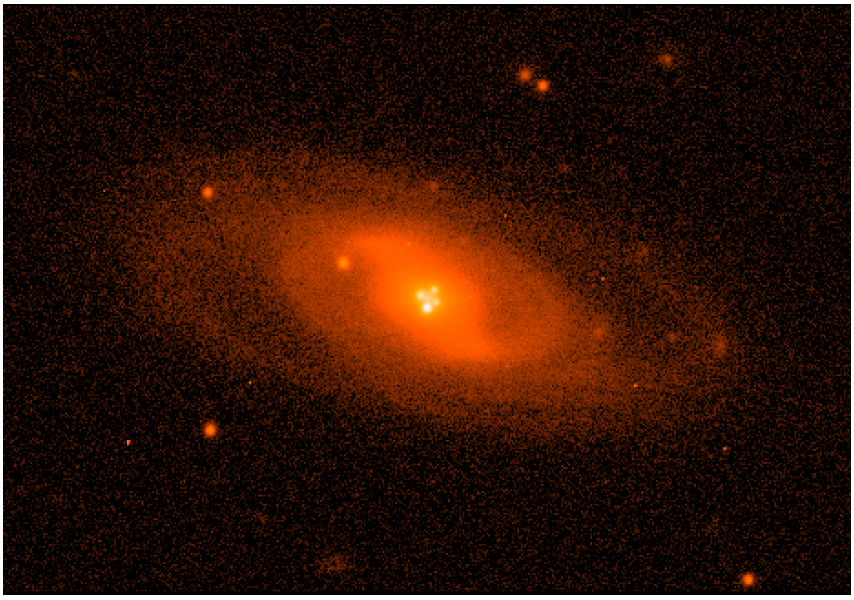

Figure 1.5 Color image of the lensed quasar Q 2237+0305, with the four images created by the lens galaxy located within the bulge, a region with a high probability of microlensing.

the same, the variability does not show up simultaneously in all of the images. This can be circumvented by measuring the time delays via careful monitoring of the lens, or working with systems with negligible time delays among their lensed images. Also, when working with the flux ratios between the images to study the microlensing, we need to disentangle this effect from the macrolensing magnification due to the bulk mass distribution of the lens galaxy itself. This is usually done by obtaining the "true" flux ratios between the lensed images as explained above.

1.3 Dark matter

1.3.1 History

In the cosmological models widely accepted today, most of the Universe's mass is found in a form that receives the name of *dark matter* due to its apparent non-detectability by means other than its gravitational interactions with light and the ordinary, baryonic matter. Postulated in the 1930s by Fritz Zwicky to explain the velocities of galaxies at the outskirts of the Coma cluster (Zwicky 1933, see also Zwicky 1937) and recovered in the 1970s as an explanation for the rotation profiles of spiral galaxies (which seemed to correspond to the velocities the matter in the galactic disc would have if it was immersed in a more or less spherical distribution of matter, the halo, see Rubin et al. 1978, 1980),

this kind of matter that doesn't interact electromagnetically is the best explanation we have for this kind of phenomena.

Observations of gravitational lensing over background galaxies have allowed to map the distribution of dark matter in clusters and superclusters, and even confirm that it is indeed a component separate from ordinary matter in the cases where a cluster collision has heated the intergalactic gas to millions of degrees and stripped it from the galaxy groups, while most of the mass has moved through with no more interaction than gravity (Clowe et al. 2006). Furthermore, the numerical simulations that allow us to understand the evolution of the Universe and the formation of galaxies, clusters and superclusters need to include dark matter in their ingredients to reproduce the observed cosmological structures accurately.

What we do know about dark matter is that for cosmological models to reproduce the observations, if it is made up of particles they have to travel at non-relativistic speeds, much slower than the speed of light, so that their total mass-energy is dominated by their rest mass mc^2 instead of their kinetic energy. This version is known as *cold dark matter* (CDM). From studying the cosmic microwave background (CMB) and fitting its properties to the standard cosmological model with cold dark matter and a cosmological constant (the ΛCDM model), dark matter is found to make up some 85% of the mass density of the universe (Planck Collaboration et al. 2014). This number is similar to the one we obtain by measuring the mass of clusters and galaxies when studying their kinematics or using gravitational lensing, and comparing it with their baryonic matter content as measured by observing their emission at different wavelengths.

The nature of dark matter is unclear. An early hypothesis stated that dark matter was made of baryonic compact objects, like rogue planets or stellar remnants, that would be too dim to be easily detected with telescopes, and would explain the lack of inner pressure due to electromagnetic forces in dark matter haloes. These candidates were named *massive astrophysical compact halo objects* (MACHOs), and would produce an observable microlensing signal if millions of stars in the Magellanic Clouds were monitored. Campaigns were undertaken with this purpose and it was concluded that MACHOs couldn't make up the majority of dark matter (Alcock et al. 2000, 2001). There are doubts regarding the strength of the exclusion from these results because they depend strongly on the model adopted for the density profile of the Milky Way halo (see e.g. Hawkins 2015), but other lines of evidence point in the same direction. For example, microlensing studies on distant lens systems conclude that only about 20% of the mass at the Einstein radius of these lenses is in compact objects (Jiménez-Vicente et al. 2015a,b). Additional attempts at direct detection or even production of dark matter have been performed by assuming that it is composed of as-yet undiscovered elementary particles that interact only via the weak nuclear force in addition to gravity, but all of them have so far been unsuccessful

(e.g. Akerib et al. 2016; PandaX-II Collaboration et al. 2016; XENON100 Collaboration et al. 2016).

1.3.2 The missing satellites problem

Even though cold dark matter is the best model we have to explain the observational evidence, some details of CDM simulations do not match observations completely, and this will require refinements to the theory, improvements on the observational techniques, or perhaps even a change of paradigm. According to cosmological simulations, as the universe evolved, dark matter would have accumulated into haloes due to gravity and irregularities in the initial mass distribution. These overdensities would have grown and accreted other dark matter haloes, while the gravity wells thus created attracted baryonic matter towards the central regions of those haloes in the process. Many of the small sized subhaloes accreted would be destroyed by tidal effects, but not all of them, so this evolution would have given rise to *substructure* in the dark matter distribution. Large haloes would contain smaller ones and so would these, resulting in the hierarchical organization we see today in the way of a large scale structure of superclusters that are themselves formed by clusters, these by galaxies, et cetera.

The amount of substructure in galaxy-sized CDM haloes is currently an open question. Simulations suggest that 10% of the mass remains in satellites today, with the fraction dropping closer to 1% in the inner regions as tidal effects destroy the satellites (e.g. Zentner & Bullock 2003). However, the number of satellite galaxies detected around the Milky Way and other nearby galaxies is just a few dozen, a much lower value than the prediction of these models (which can reach up to thousands of subhaloes, e.g. Stadel et al. 2009), so there is a contradiction between the theoretical predictions and the observations (Klypin et al. 1999; Kravtsov et al. 2004; Moore et al. 1999).

This discrepancy could be solved in several ways. One possibility is that the number of these subhaloes really is low, perhaps because some mechanism prevents the formation of separate haloes with such low masses (some kinds of self-interacting dark matter particles might have this effect), because their destruction by tides is more efficient than expected, or by some other factors. Another solution, however, consists of assuming the subhaloes are there as the models predict, but for some reason their baryonic content is very low and most of them contain few or no stars, thus becoming hard to detect. Most of the reasons why the subhaloes could be dark are baryonic processes, especially the effects of photo reionization and stellar feedback on galaxy formation (Benson et al. 2002; Bovill & Ricotti 2009; Bullock et al. 2000; Cooper et al. 2010; Font et al. 2011; Guo et al. 2011). In any case, the gap between the observed numbers of satellite galaxies and the dark matter predictions has been reduced somewhat in the last decade with the discovery of a new population of dozens of Milky Way faint satellites (Belokurov et al. 2006; Koposov

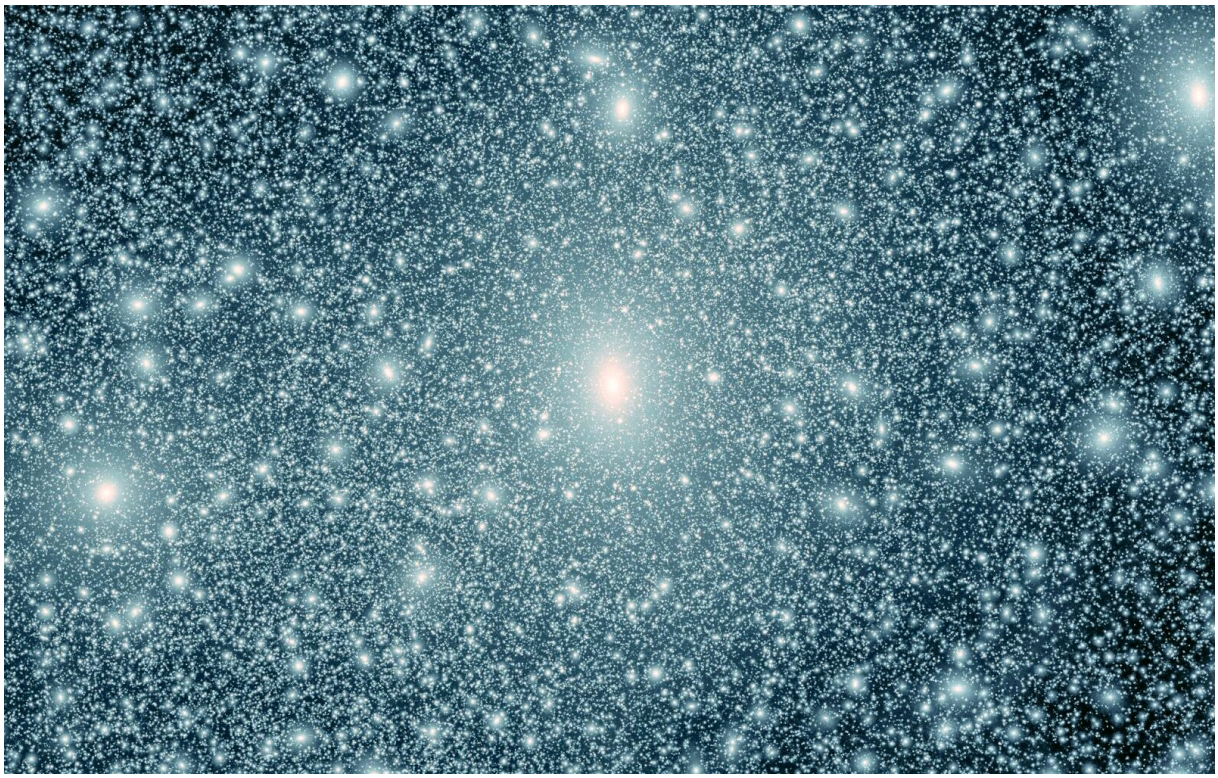

Figure 1.6 GHALO simulation of the dark matter distribution in a galactic halo similar to the Milky Way. The height of the image is 400 kpc, and thousands of dark matter subhaloes are visible. *Credit:* Stadel et al. (2008).

et al. 2015; Zucker et al. 2006). Also, new estimations of the Milky Way halo mass are leaning towards lower values ($\lesssim 10^{12}\,M_\odot$ instead of around twice that), and this reduces the predicted halo population at the high-mass end (Kafle et al. 2014; Wang et al. 2012). However, the true virial mass of the Milky Way is hard to estimate with current methods due to a diversity of biases and assumptions that might not match the particularities of a certain halo (Wang et al. 2015), and in any case the discrepancy at lower subhalo masses would still exist.

Even if most of the dark matter subhaloes were completely dark, searches could be performed by using the effect their gravity would have in the flux ratios of lensed quasars. In fact, several of these systems have anomalous fluxes in some of their images that are hard to explain by modeling the smooth potential of the lens. This is the 'anomalous flux ratio' problem (Kochanek 1991). Besides possible systematic errors and the intrinsic variability of the quasar plus the time delays, it was argued that ISM extinction would cause these differences, or that gravitational microlensing could magnify the lensed images separately (or at least the bright regions of the accretion disk), but these anomalous fluxes were also detected in radio frequencies. At these wavelengths, absorption by the ISM is less important and the quasar variability is low, and the radio emitting regions are too large to be affected by stellar microlensing, so the former explanations would be discarded in these cases. On the other hand, the anomalous flux is surprisingly easy to reproduce by adding a satellite galaxy to the model of the lens potential. It is possible that these anomalous fluxes are the needed observable imprint to solve the problem of the dark matter subhaloes, turning gravitational lensing into a very useful tool for their detection and study.

A number of studies have been performed over the years using N-body simulations to test if the predicted CDM substructures have the right amount to explain the observed frequency of anomalous lenses in currently available samples. Dalal & Kochanek (2002), Bradač et al. (2004), Dobler & Keeton (2006), and Metcalf & Amara (2012), among others, suggest that there is a consistency between the CDM model and observations. On the other hand, however, Mao et al. (2004), Amara et al. (2006), Macciò et al. (2006), Macciò & Miranda (2006), Chen et al. (2011), and Xu et al. (2009, 2010) find that subhaloes from CDM simulations are actually insufficient to explain the observed radio flux anomalies, that is, that the number of satellites would have to be even larger than predicted. There are some factors that could influence this result. For example, the flux ratios are quite sensitive to the ellipticity of the main lens, so without a good estimation of this value, the analysis could yield discrepancies that were not really there (Keeton et al. 2003; Metcalf & Amara 2012). Also, about 80-90 % of the observed lenses are massive elliptical galaxies (Keeton et al. 2003; Kochanek et al. 2000; Rusin et al. 2003) and the subhalo abundance increases rapidly with increasing host halo mass (e.g. De Lucia et al. 2004; Gao et al. 2004; Zentner et al. 2005; Wang et al. 2012), but many estimates were done by scaling

Milky Way-sized haloes like those from the Aquarius project (Springel et al. 2008), and this would lead to an underestimation of the number of subhaloes predicted by CDM in these lenses. More studies are still required in order to solve this problem.

Chapter 2

Structure of the Accretion Disk in the Lensed Quasar Q 2237+0305

We present estimates for the size and the logarithmic slope of the disk temperature profile of the lensed quasar Q 2237+0305, independent of the component velocities. These estimates are based on six epochs of multi-wavelength narrowband images from the Nordic Optical Telescope. For each pair of lensed images and each photometric band, we determine the microlensing amplitude and chromaticity using pre-existing mid-IR photometry to define the baseline for no microlensing magnification. A statistical comparison of the combined microlensing data (6 epochs × 5 narrow bands × 6 image pairs) with simulations based on microlensing magnification maps gives Bayesian estimates for the half-light radius of $R_{1/2} = 8.5^{+7.5}_{-4.0}\sqrt{\langle M\rangle/0.3\ \mathrm{M}_\odot}$ light-days, and $p = 0.95\pm0.33$ for the exponent of the logarithmic temperature profile $T \propto R^{-1/p}$. This size estimate is in good agreement with most recent studies. Other works based on the study of single microlensing events predict smaller sizes, but could be statistically biased by focusing on high-magnification events.

This chapter is based on the article *Structure of the Accretion Disk in the Lensed Quasar Q2237+0305 from Multi-epoch and Multi-wavelength Narrowband Photometry* by Muñoz, J.A., Vives-Arias, H., Mosquera, A.M., Jiménez-Vicente, J., Kochanek, C.S. & Mediavilla, E. (2016), *ApJ*, **817**, 155.

2.1 Q 2237+0305: the Einstein Cross

Q 2237+0305 (Huchra et al. 1985) is a gravitational lens system in which a nearby spiral galaxy ($z_L = 0.0395$) produces four images of a distant quasar ($z_S = 1.695$) that is almost in the exact line of sight as the center of the lens galaxy (Yee 1988). It was one of the first four-image lenses discovered, and the symmetry of the quasar images produced by

this alignment earned this system the nickname '*the Einstein Cross*'. The closeness of the lens galaxy to the observer makes the light paths of the multiple images go through the dense galactic bulge, and leads to a high effective transverse velocity between lenses, source and observer. These factors create a very high probability of stellar microlensing in the system, making it the first one where this effect was ever detected (Irwin et al. 1989). Furthermore, because the light paths for the different images are so similar, the time delays between intrinsic brightness variations from the quasar are less than 1 day between image pairs (Dai et al. 2003; Koptelova et al. 2006; Vakulik et al. 2006). Since quasars have little variability power on such short time scales, there is no need to correct for the delays in this system when performing microlensing studies, which allows us to obtain useful information even when using data from a single epoch.

Since this is a well studied system, with microlensing variability which has now been observed for ∼30 years (e.g. Corrigan et al. 1991; Webster et al. 1991; Woźniak et al. 2000), many parameters of the different components of the AGN source have been determined over the last decade. Motta et al. (2004) may have been able to determine an NLR size between ~ 0.7 and ~ 1.0 kpc using early integral field spectroscopy observations. The size of the BLR is better constrained by studying the microlensing effect on several spectral lines, with a half-light radius of $R_{\mathrm{C\,IV}} \sim 66^{+110}_{-46}$ light-days and $R_{\mathrm{C\,III]}} \sim 49^{+105}_{-35}$ light-days (Sluse et al. 2011), consistent with previous estimates by Wayth et al. (2005), who estimate the size of the $\mathrm{C_{III]}}/\mathrm{Mg_{II}}$ BLR to be ~ 0.06 pc (~ 70 light-days), also using microlensing. Agol et al. (2009) performed infrared observations that allowed them to estimate the minimum radius for the dusty torus of the AGN at about 1pc, and to determine the total bolometric luminosity of the source, $L_{tot} = 4.0 \times 10^{46}$ erg s^{-1}. Using broad spectral emission lines, the mass of the supermassive black hole powering the AGN was estimated at $M_{BH} \sim 10^{8.3\pm0.3}\,\mathrm{M}_\odot$ using the $\mathrm{C_{IV}}$ spectral line (Sluse et al. 2011), and $M_{BH} = 10^{9.08\pm0.39}\,\mathrm{M}_\odot$ using the Hβ emission line, which might be more reliable (Assef et al. 2011). X-ray spectroscopy of the innermost region of the accretion disk has even allowed to estimate that the spin of the black hole is $a_* = 0.74^{+0.06}_{-0.03}$, with 90% confidence, or $a_* \geqslant 0.65$ at the 4σ level (Reynolds et al. 2014). Microlensing studies of this X-ray emission conclude that the size of this inner region is ~ 1 light-day (Mosquera et al. 2013). In this chapter we will focus on the size of the accretion disk itself, by studying light that corresponds to its UV emission at rest wavelengths.

2.2 Estimating the size of accretion disks with gravitational lensing

The basic model for describing the inner regions of quasars is the thin disk model (Novikov & Thorne 1973; Shakura & Sunyaev 1973) which predicts the size of the accretion disk and the radial dependence of its surface temperature (see Section 1.2.2). Gravitational

microlensing (Chang & Refsdal 1979, 1984, see also Section 1.1.3, Kochanek 2004b and Wambsganss 2006) is the main tool used to estimate both parameters, either from time variability or through the wavelength dependence of the microlensing magnification. Microlensing studies (see e.g. Blackburne et al. 2011, 2014, 2015; Hainline et al. 2013; Jiménez-Vicente et al. 2012, 2014; MacLeod et al. 2015; Morgan et al. 2010; Mosquera & Kochanek 2011; Mosquera et al. 2013; Pooley et al. 2007; Sluse et al. 2011) have found that the mean sizes of quasar accretion disks are roughly a factor of 2-3 greater than the predictions of the standard thin disk model. These differences are too large to be explained by contamination from the broad emission lines and the pseudo-continuum contributions, or scattering on scales larger than the accretion disk (Dai et al. 2010; Morgan et al. 2010). Recent measurements of wavelength-dependent continuum lags in two local AGN are consistent with the microlensing results (Edelson et al. 2015; Fausnaugh et al. 2015; Shappee et al. 2014).

The study of the disk temperature profile is more complicated than obtaining only its size because multi-wavelength observations are needed to detect chromatic microlensing (Anguita et al. 2008; Bate et al. 2008; Blackburne et al. 2011, 2015; Eigenbrod et al. 2008; Floyd et al. 2009; Mediavilla et al. 2011b; Mosquera & Kochanek 2011; Motta et al. 2012; Muñoz et al. 2011; Poindexter et al. 2008; Rojas et al. 2014). In this case it also becomes more important to separate the contributions from strong emission lines. This can be done most cleanly using narrow band photometry or spectroscopy.

Many of the studies of the source size in Q 2237+0305 are based on the fitting of its light curves with tracks extracted from simulated microlensing magnification maps (Kochanek 2004b; Mosquera et al. 2013; Poindexter & Kochanek 2010a). As an alternative to light-curve fitting, we will study the size and temperature profile of Q 2237+0305 using several epochs of multi-wavelength narrow band observations. This allows us to remove the influence of the broad emission lines on the amplitude of the continuum microlensing (Mosquera et al. 2009). We will follow a procedure similar to that used in SBS 0909+532 (Mediavilla et al. 2011b) and HE 1104–1804 (Muñoz et al. 2011), but in the case of Q 2237+0305 we have significantly better statistics with 6 epochs (4 will be considered independent) and 4 quasar images. This method relies on changes in the microlensing amplitude and chromaticity but not on its dependence with time and hence no velocity estimates are necessary. However, a baseline for the intrinsic flux ratios in the absence of microlensing is needed, and we will define these by the mid-IR flux ratios from Minezaki et al. (2009, see also Agol et al. 2000).

2.3 Observations and Data Analysis

Q 2237+0305 was observed with the 2.56 m Nordic Optical Telescope (NOT) located at the Roque de los Muchachos Observatory, La Palma (Spain), using the 2048×2048 ALFOSC detector, with a spatial scale of 0.188 arcsec/pixel. A total of five epochs in 2006 and 2007 were obtained, which we combine with an earlier epoch from Mosquera et al. (2009) taken in 2003. A set of seven narrow filters plus the wide Bessel I filter were used, covering the wavelength range 3510-8130Å. Table 2.1 provides a log of these observations. For the first epoch, a V-band image was also taken. In the second epoch, the wavelength coverage was poorer, because observations with all the filters were not possible due to bad weather conditions.

The data were reduced with standard IRAF[1] procedures, and point-spread function (PSF) photometry fitting was used to derive the difference in magnitude as a function of wavelength between the 4 images. As in Mosquera et al. (2009), the galaxy bulge was modeled with a de Vaucouleurs profile, and the quasar images as point sources. This model was convolved with PSFs derived from stars observed in each of the frames, and fit to the image using χ^2 statistics following McLeod et al. (1998) and Lehár et al. (2000). Even in the bluest filters, the fits were excellent due to the good seeing conditions for most of the epochs ($0\farcs6$ in I-band). Among the narrower filters that were used, only two were affected by the broad emission lines of the quasar. The Strömgren-u filter contains roughly 40% of the Lyα emission line, based on the SDSS quasar composite spectrum from Vanden Berk et al. (2001). And at $\lambda = 4110$ Å, the wavelength range covered by the Strömgren-v filter coincides with the position and width of the CIV emission line (for more details see Mosquera et al. 2009).

Figure 2.1 shows the results for the six nights and Table 2.1 reports the photometry for the new data. A clear wavelength dependence of the flux ratios $(m_i - m_A)_{i=B,C,D}$ relative to image A is observed for the epochs HJD 2454056 (Fig. 2.1d) and HJD 2454404 (Fig. 2.1f). Chromatic effects are also observed relative to image B $(m_i - m_B)_{i=A,C,D}$ on the first of these two dates. Since extinction effects would be common to all the epochs (e.g. Falco et al. 1999 or Muñoz et al. 2004) and the time delays are negligible, this dependence can only be explained by chromatic microlensing of images A and B (for more details see Mosquera et al. 2009). Since image C seems little affected by chromatic microlensing on any of those nights, the difference $(m_C - m_A)^I - (m_C - m_A)^b$ allows us to determine the chromaticity in image A, with values of $m_A^b - m_A^I = -0.43 \pm 0.16$ and $m_A^b - m_A^I = -0.33 \pm 0.16$ for HJD 2454056 and HJD 2454404 respectively. In a similar way, the chromaticity for image B is $m_B^b - m_B^I = -0.25 \pm 0.16$ for HJD 2454056. The

[1]IRAF is distributed by the National Optical Astronomy Observatory, which is operated by the Association of Universities for Research in Astronomy (AURA) under a cooperative agreement with the National Science Foundation

Table 2.1. Q 2237+0305 PHOTOMETRY

Filter	$m_B - m_A$	$m_C - m_A$	$m_D - m_A$	Observation date
Str-u ($\lambda = 3510$ Å)	1.18±0.07	1.56±0.11	1.47±0.06	Aug 21 2006
Str-v ($\lambda = 4110$ Å)	1.15±0.06	1.58±0.08	1.46±0.06	Aug 21 2006
Str-b ($\lambda = 4670$ Å)	1.19±0.06	1.59±0.07	1.61±0.06	Aug 21 2006
V-band ($\lambda = 5300$ Å)	1.19±0.04	1.64±0.06	1.56±0.06	Aug 21 2006
Str-y ($\lambda = 5470$ Å)	1.19±0.03	1.59±0.05	1.59±0.04	Aug 21 2006
Iac#28 ($\lambda = 6062$ Å)	1.14±0.10	1.50±0.10	1.51±0.10	Aug 21 2006
Hα ($\lambda = 6567$ Å)	1.15±0.06	1.51±0.08	1.47±0.03	Aug 21 2006
Iac#29 ($\lambda = 7015$ Å)	1.16±0.06	1.54±0.06	1.48±0.06	Aug 21 2006
I-band ($\lambda = 8130$ Å)	1.16±0.08	1.59±0.15	1.48±0.06	Aug 21 2006
Str-u ($\lambda = 3510$ Å)	1.13±0.08	1.49±0.05	1.44±0.07	Sep 23 2006
Str-v ($\lambda = 4110$ Å)	1.13±0.10	1.55±0.10	1.41±0.10	Sep 23 2006
Str-y ($\lambda = 5470$ Å)	1.10±0.10	1.39±0.10	1.34±0.10	Sep 23 2006
Hα ($\lambda = 6567$ Å)	1.14±0.05	1.47±0.08	1.38±0.06	Sep 23 2006
I-band ($\lambda = 8130$ Å)	1.15±0.06	1.53±0.09	1.41±0.06	Sep 23 2006
Str-u ($\lambda = 3510$ Å)	1.22±0.09	1.74±0.08	1.74±0.10	Nov 17 2006
Str-v ($\lambda = 4110$ Å)	1.14±0.02	1.57±0.03	1.41±0.03	Nov 17 2006
Str-b ($\lambda = 4670$ Å)	1.22±0.05	1.74±0.09	1.63±0.05	Nov 17 2006
Str-y ($\lambda = 5470$ Å)	1.22±0.08	1.73±0.11	1.60±0.06	Nov 17 2006
Iac#28 ($\lambda = 6062$ Å)	1.30±0.03	1.59±0.07	1.62±0.04	Nov 17 2006
Hα ($\lambda = 6567$ Å)	1.02±0.08	1.38±0.07	1.22±0.04	Nov 17 2006
Iac#29 ($\lambda = 7015$ Å)	1.17±0.07	1.64±0.12	1.43±0.05	Nov 17 2006
I-band ($\lambda = 8130$ Å)	1.05±0.08	1.31±0.13	1.19±0.08	Nov 17 2006
Str-u ($\lambda = 3510$ Å)	1.33±0.10	1.84±0.09	1.44±0.09	Oct 15 2007
Str-v ($\lambda = 4110$ Å)	1.28±0.06	1.74±0.10	1.29±0.06	Oct 15 2007
Str-b ($\lambda = 4670$ Å)	1.37±0.05	1.83±0.05	1.37±0.04	Oct 15 2007
Str-y ($\lambda = 5470$ Å)	1.31±0.04	1.63±0.10	1.18±0.06	Oct 15 2007
Iac#28 ($\lambda = 6062$ Å)	1.28±0.10	1.60±0.09	1.29±0.10	Oct 15 2007
Hα ($\lambda = 6567$ Å)	1.24±0.06	1.63±0.10	1.25±0.06	Oct 15 2007
Iac#29 ($\lambda = 7015$ Å)	1.25±0.08	1.63±0.08	1.26±0.06	Oct 15 2007
I-band ($\lambda = 8130$ Å)	1.25±0.06	1.58±0.06	1.21±0.06	Oct 15 2007
Str-u ($\lambda = 3510$ Å)	1.43±0.03	2.06±0.09	1.48±0.04	Oct 31 2007
Str-v ($\lambda = 4110$ Å)	1.32±0.08	1.89±0.10	1.37±0.09	Oct 31 2007
Str-b ($\lambda = 4670$ Å)	1.39±0.09	2.02±0.10	1.46±0.07	Oct 31 2007
Str-y ($\lambda = 5470$ Å)	1.37±0.08	1.98±0.10	1.43±0.06	Oct 31 2007
Iac#28 ($\lambda = 6062$ Å)	1.33±0.09	1.97±0.11	1.45±0.08	Oct 31 2007
Hα ($\lambda = 6567$ Å)	1.34±0.06	1.82±0.10	1.40±0.08	Oct 31 2007
Iac#29 ($\lambda = 7015$ Å)	1.24±0.06	1.67±0.10	1.21±0.02	Oct 31 2007
I-band ($\lambda = 8130$ Å)	1.22±0.08	1.69±0.12	1.22±0.08	Oct 31 2007

I and b filters were chosen to perform these calculations since they are the reddest and bluest filters that are not affected by the broad emission lines. The other epochs do not show any significant dependence on wavelength. In particular the magnitude difference as a function of wavelength for the epoch HJD 2454001 (Fig. 2.1c) is flat given our errors of order ~ 0.1 mag. This suggests a smaller differential extinction than the estimates of Agol et al. (2000), although we cannot rule out fortuitous cancellations of color variations due to extinction by chromatic microlensing effects. Finding chromatic microlensing during this period of observations is not a surprise, since the OGLE V-band continuum data (Woźniak et al. 2000) shows significant brightness variations in the three independent magnitude differences at this time. This implies that microlensing is strongly affecting the quasar images, making chromatic microlensing effects more likely.

2.4 Results

The method used to estimate the size of the accretion disk and the wavelength dependence with the radius proceeds as follows. First, we generate a magnification map for each of the four lensed images (see Section 1.1.3.2) using the local values of κ and γ for the macrolensing potential of the lens. Then, because the microlensing magnifications depend on the size of the source, and the apparent size depends on the wavelength observed, we convolve the magnification maps with the source brightness profile for each wavelength in each set of parameters that we want to test. After that, for each of these cases we select random locations in the four corresponding magnification maps, calculate the resulting predicted microlensing magnifications and compare them to the observations. We estimate the probability of reproducing the observed magnitude differences between the lensed images by performing a large number of iterations of this process, and thus obtain the probability distribution function (PDF) for a given range of parameters of the chosen brightness profile for the source. We take into account the several independent epochs by multiplying their resulting PDFs. This statistical procedure is a variant of that described in Mediavilla et al. (2011b), Muñoz et al. (2011) and Jiménez-Vicente et al. (2012). The main difference is that, in this work, the observed magnitudes for the four quasar images in the five different bands will be used simultaneously to calculate the probability distributions.

The magnification maps were calculated using the Inverse Polygon Mapping algorithm (Mediavilla et al. 2006, 2011a). We have used canonical values for κ and γ for the four images from Schmidt et al. (1998) and put all the mass into equal mass stars. The models used by Poindexter & Kochanek (2010b) are very similar but with a mass spectrum for the stars. The maps have 2000×2000 pixels and a pixel size of 0.5 light-days for a mean stellar mass of $\langle M \rangle = 1\,\mathrm{M}_\odot$ and all linear sizes can be scaled with $(\langle M \rangle/\mathrm{M}_\odot)^{1/2}$. We considered three surface brightness profiles. In all three models, the scaling of the source size

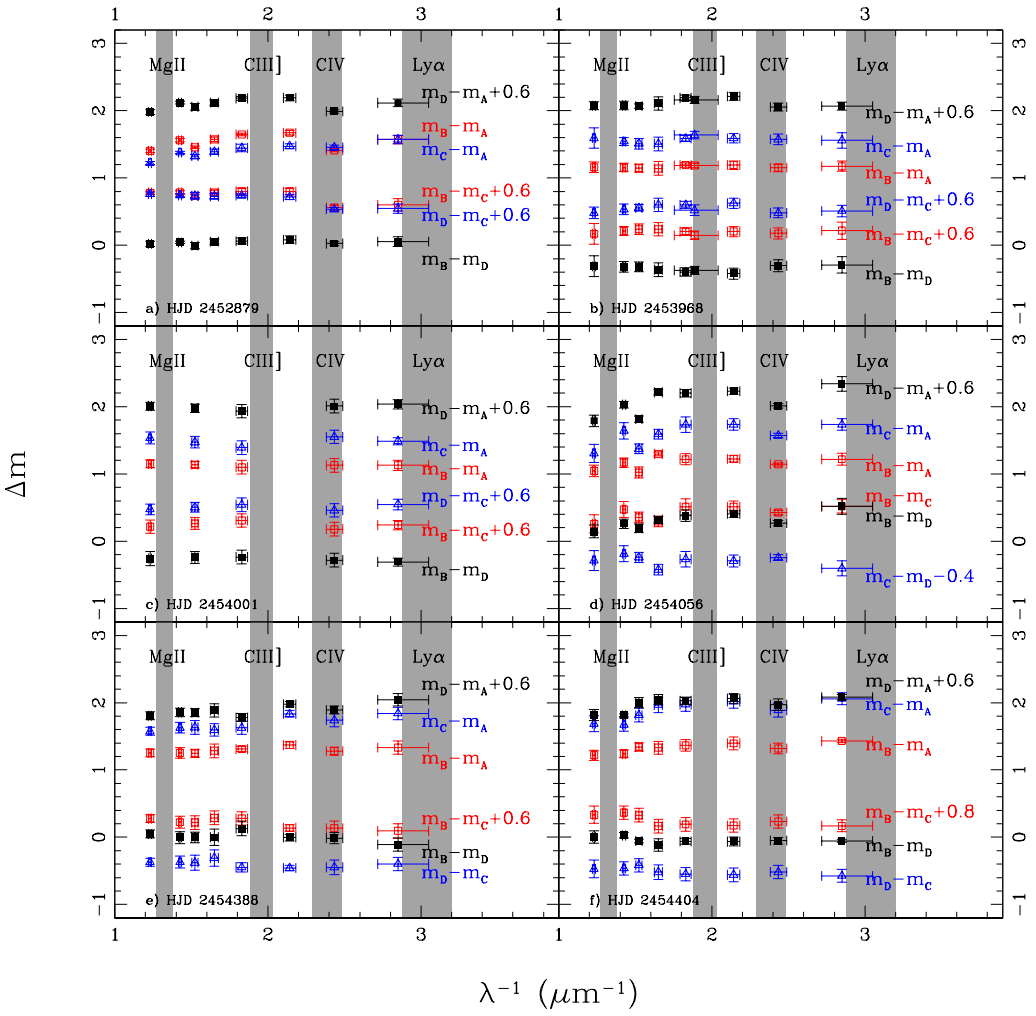

Figure 2.1 Magnitude differences as a function of the inverse of the observed wavelength for Q 2237+0305 during the six epochs of observation. Image A showed chromaticity on epoch HJD 2452879 (a), as previously analyzed by Mosquera et al. (2009). Here we find that image A also shows evidence of chromaticity on HJD 2454056 (d) and HJD 2454404 (f), as does image B on HJD 2454056 (d). The shaded regions correspond to the wavelength location and full width of the most prominent quasar broad emission lines. The horizontal error bars indicate the FWHM of the filters.

with wavelength is described by a power-law, $r_s(\lambda_2) = (\lambda_2/\lambda_1)^p r_s(\lambda_1)$ where λ_i is the rest wavelength corresponding to each filter. The first model we consider is a simple Gaussian, $I(R) \propto \exp(-R^2/2r_s^2)$. The second model, $I(R) \propto \left(\exp\left[(R/r_s)^{3/4}\right] - 1\right)^{-1}$ becomes the standard thin disk model when $p = 4/3$. The third model, $I(R) \propto \left(\exp\left[(R/r_s)^{1/p}\right] - 1\right)^{-1}$ also becomes the standard thin disk model when $p = 4/3$. The third model corresponds to a thermally emitting disk with a temperature profile $T \propto R^{-1/p}$ and is well-defined only for $p > 1/2$ since we are not including an inner edge. The second model is a hybrid, but by holding the exponent in the black body function fixed and only varying the scale length, the brightess profile is well defined for all p. We will refer to the three models as the Gaussian, hybrid and thin disk models. The length scales r_s will depend on the profile and p, but we expect the estimates of the half-light radii for the different profiles to agree based on the results of Mortonson et al. (2005). We use the bluest observed wavelength, $\lambda_1^{obs} = 4670\,\text{Å}$ as the reference wavelength, corresponding to $\lambda_1 = 1736$ Å in the rest frame. When no reference is made to a specific wavelength, the size is for this reference wavelength, $r_s \equiv r_s(1736\,\text{Å})$.

The observed magnitude of image $I = (A, B, C, D)$ is

$$m_I^{obs}(t_j, i) = m_0(t_j, i) + \mu_I + \delta\mu_I(t_j, i) \tag{2.1}$$

where $m_0(t_j, i)$ is the intrinsic magnitude of the source at time t_j in filter i, μ_I is the macro magnification (in mag) of image I and $\delta\mu_I(t_j, i)$ is the time varying microlensing magnification (in mag) of image I in filter i. Since we have no direct information on the intrinsic variability of the source or the absolute magnifications, we ultimately want to work in terms of magnitude differences between images. We assume that the mid-IR flux ratios from Minezaki et al. (2009) (cf. their Table 4) correctly estimate the intrinsic flux ratios μ_{IJ}^{ir}, which means that they define all the values of $\mu_{IJ}^{ir} = \mu_I - \mu_J$. Following Kochanek (2004b), we eliminate the intrinsic magnitude of the source $m_0(t_j, i)$ by starting from the fit to the four individual images at a single epoch and wavelength

$$\chi^2(t_j, i) = \sum_I \sigma_I(t_j, i)^{-2} \left[m_I^{obs}(t_j, i) - m_0(t_j, i) - \mu_I - \delta\mu_I(t_j, i)\right]^2 \tag{2.2}$$

and optimizing for the best source model $m_0(t_j, i)$. If we then substitute this best fit source model into $\chi^2(t_j, i)$, we are left with a sum over the six possible pairs between the four images

$$\chi^2(t_j, i) = \sum_I \sum_{J>I} \sigma_{IJ}(t_j, i)^{-2} \left[\Delta m_I(t_j, i) - \Delta m_J(t_j, i)\right]^2 \tag{2.3}$$

where

$$\Delta m_I(t_j, i) = m_I^{obs}(t_j, i) - \mu_I - \delta\mu_I(t_j, i) \tag{2.4}$$

and the errors $\sigma_{IJ}(t_j, i)$ are defined in the equation 7 of Kochanek (2004b) but reduce to $\sigma_{IJ}(t_j, i) = 2\,\sigma(t_j, i)$ if $\sigma_I = \sigma_J (\equiv \sigma)$ as we will assume here[1]. This expression only depends on $\mu_I - \mu_J$, whose values are supplied by the mid-IR flux ratios. Thus, the full χ^2_j for a given epoch t_j becomes the sum of Equation 2.3 over the filters,

$$\chi^2_j = \sum_i \chi^2(t_j, i) \tag{2.5}$$

which can be evaluated for any microlensing trial defining the values of $\delta\mu_I(t_j, i)$.

For a given pair of parameters (r_s, p), the magnification maps for the four images A, B, C, D are convolved to the size $r_s(\lambda/\lambda_0)^p$ appropriate for each wavelength and the χ^2_j are calculated for N=10^8 randomly selected locations in each of the four magnification maps. The probability density function $P_j(r_s, p)$ for each epoch is computed as the sum

$$P_j(r_s, p) \propto \sum_{i=1}^{N} e^{-\frac{1}{2}\chi^2_j} \tag{2.6}$$

over a 2D grid of values for r_s and p. We have used a logarithmic grid in r_s such that $\ln(r^i_s/\text{light-days}) = 0.3 \times i$ for $i = 0, \cdots, 17$ and a linear grid in p with $p^j = 0.25 \times j$ for $j = 0, \cdots, 9$. This way, r_s spans from roughly 1 to 165 light-days and p runs from 0 to 2.25. For the thin disk model, which is only defined for $p > 1/2$, we ran extra cases at $p = 0.55$ and 0.68 and then follow the remainder of the sequence.

We have data for six different epochs between August 2003 and October 2007. Some of the epochs are very close on time and we have combined them into a single epoch because they cannot be considered independent. Epoch HJD 2453968 (Aug 21st 2006) is combined with HJD 2454001 (Sep 23rd 2006) and epoch HJD 2454388 (Oct 15th 2007) is combined with HJD 2454404 (Oct 31st 2007). The dispersion around the mean for all values of the combined epochs is 0.08 mag, which is the same as the measurement error we adopted for the merit function above.

The joint probability distribution $\mathcal{P}(r_s, p)$ for the four independent epochs is obtained by the product of the probabilities for each of the epochs

$$\mathcal{P}(r_s, p) = \prod_j P_j(r_s, p) \tag{2.7}$$

The resulting joint probability distributions of the three surface brightness profiles are shown in Figure 2.2 and are compared to previous size estimates for Q 2237+0305 in

[1]Although there are slightly different errors for every individual image we have chosen to use the average measurement error $\sigma = 0.08$ for weighting all the data.

Figure 2.3. The maximum likelihood estimate from this work corresponds to $r_s = (15.6^{+5.5}_{-7.9}, 5.3^{+1.9}_{-2.4}, 27^{+22}_{-19})\ \sqrt{\langle M\rangle/0.3\,\mathrm{M}_\odot}$ light-days and $p = (0.50^{+0.15}_{-0.27}, 1.0^{+0.25}_{-0.50}, 0.85^{+0.25}_{-0.25})$ for the Gaussian, hybrid and thin disk models respectively. Using a logarithmic (linear) prior for r_s (p), we obtain Bayesian estimates for the expected values of $r_s = (7.0^{+10.0}_{-4.1}, 3.7^{+3.5}_{-1.8}, 7.9^{+16.6}_{-5.3})\sqrt{\langle M\rangle/0.3\,\mathrm{M}_\odot}$ light-days and $p = (0.66 \pm 0.32, 1.04 \pm 0.29, 0.95 \pm 0.33)$. As a test we also computed the joint probability distribution without merging the closely separated epochs and obtained very similar results.

2.5 Discussion and Conclusions

At $\lambda_1 = 1736$ Å, the half-light radius estimates for the three (Gaussian, hybrid, thin disk) models of $R_{1/2} = (8.3^{+11.8}_{-4.8}, 9.0^{+8.4}_{-4.4}, 8.5^{+7.5}_{-4.0})\sqrt{\langle M\rangle/0.3\,\mathrm{M}_\odot}$ light-days are remarkably similar (see Figure 2.2), consistent with the prediction from Mortonson et al. (2005) that estimates of the half-light radius should be insensitive to the particular surface brightness profile shape. Our $R_{1/2}$ estimations are also in agreement with previous estimates by Poindexter & Kochanek (2010a, $R_{1/2} = 5.4 \pm 3.2$ light-days), Sluse et al. (2011, $R_{1/2} = 3.4^{+6.4}_{-2.4}$ light-days) and Mosquera et al. (2013, $R_{1/2} = 9.9^{+5.1}_{-3.3}$ light-days), as shown in Figure 2.3. The latter two results are also scaled to $\langle M\rangle = 0.3\,\mathrm{M}_\odot$. The Poindexter & Kochanek (2010a) result marginalizes over the uncertainties in $\langle M\rangle$, finding $\langle M\rangle = 0.52\,\mathrm{M}_\odot$ ($0.12\,\mathrm{M}_\odot < \mathrm{M} < 1.94\,\mathrm{M}_\odot$). Poindexter & Kochanek (2010a,b), Mosquera et al. (2013) and Sluse et al. (2011) set the scales by adopting priors on the effective source velocity rather than choosing a fixed mean mass $\langle M\rangle$. That our results agree demonstrates that these priors are reasonable.

Analyses of individual high magnification events tend to measure smaller sizes. For example Anguita et al. (2008) find $R_{1/2} = 1.0^{+0.2}_{-0.5}$ light-days and Eigenbrod et al. (2008) find $R_{1/2} = 3.0 \pm 2.0$ light-days. However, studies of high magnification events are likely biased toward small accretion disk size estimates because it is easier to obtain high magnifications with small sources (e.g. Blackburne et al. 2011; Eigenbrod et al. 2008; Kochanek 2004b). It is also interesting to note that without considering any velocity prior (i.e. adopting a uniform prior), the size determinations of Eigenbrod et al. (2008) and Anguita et al. (2008) increase by a factor ~ 4 (see Sluse et al. 2011) but would then require cosmologically unrealistic peculiar velocities for the lens/source.

In any case, most of the results derived from the optical may be reconciled near a value of $\sim (7 \pm 4)\sqrt{\langle M\rangle/0.3\,\mathrm{M}_\odot}$ light-days. This value is large compared to the predictions of the thin disk model based on the flux (~ 1 light-day, Mosquera & Kochanek 2011). It is in agreement with the results from other lenses, where the Morgan et al. (2010) black hole-mass-size correlation predicts a size of ~ 5 light-days for an estimated black hole mass of $1.2 \times 10^9\,\mathrm{M}_\odot$ (Assef et al. 2011). This size discrepancy is now also seen in the

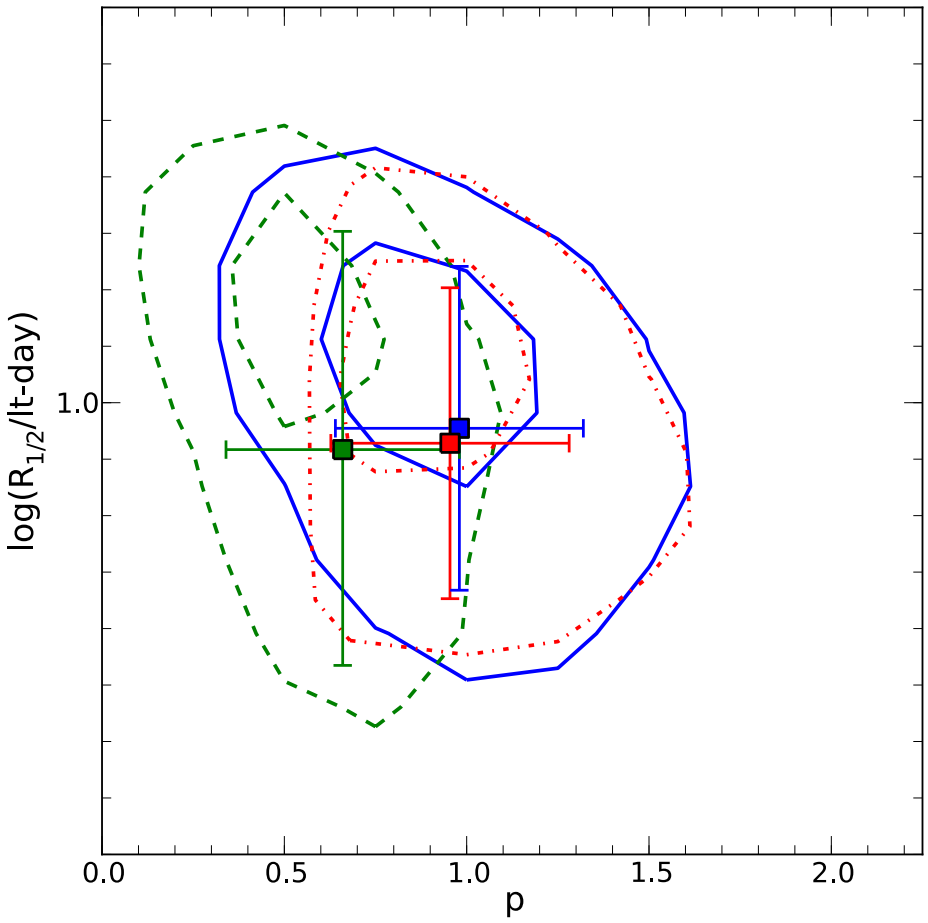

Figure 2.2 Joint probability density function $\mathcal{P}(r_s, p)$ in terms of the half-light radius $R_{1/2}$, at rest $\lambda_1 = 1736$ Å, and the logarithmic slope p ($r_s \propto \lambda^p$). The contours for each model correspond to the 1σ and 2σ levels for one parameter. The Gaussian, hybrid and thin disk models are shown by the green (dashed), blue (solid) and dotted (red) colors (lines). The filled squares are the Bayesian estimates for the expected values of $R_{1/2}$ and p.

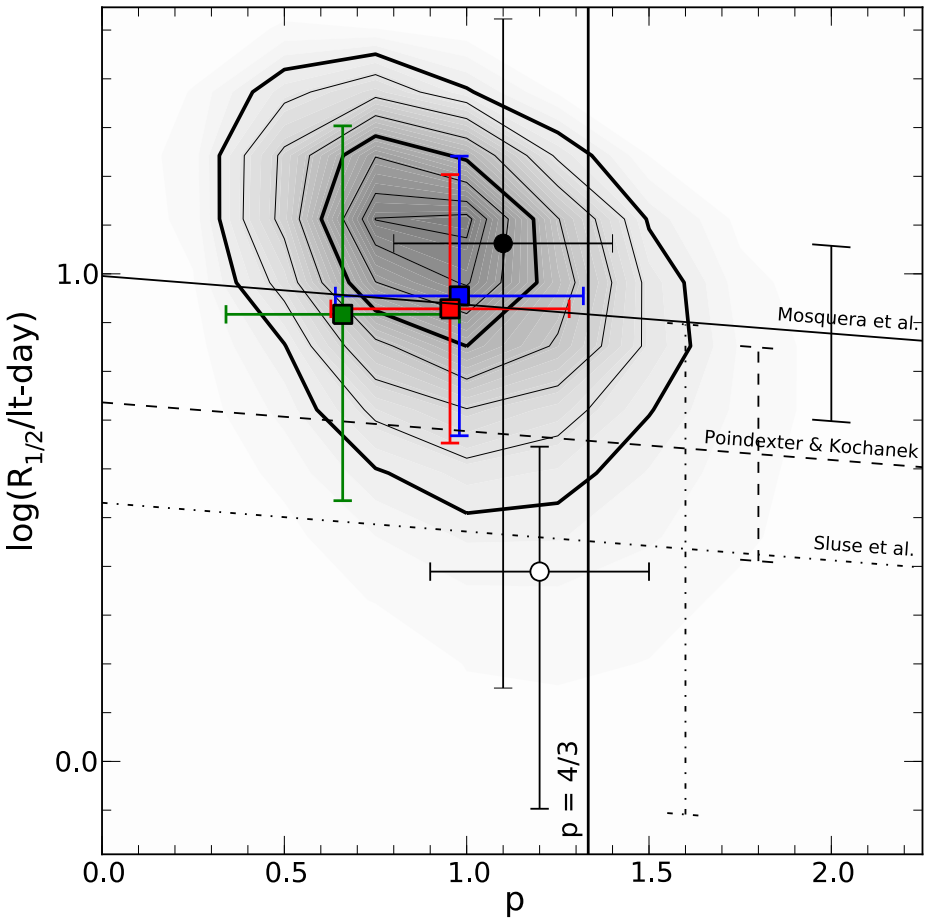

Figure 2.3 Joint probability density function $\mathcal{P}(r_s, p)$ in terms of the half-light radius $R_{1/2}$, at rest $\lambda_1 = 1736$ Å, and the logarithmic slope p ($r_s \propto \lambda^p$) for the hybrid model. The separation between consecutive contours corresponds to 0.25σ, the 1σ and 2σ for one parameter contours are heavier. The blue filled square is our Bayesian estimate for the expected value of $R_{1/2}$ and p for the hybrid model (the values for the Gaussian and thin disk models are also plotted as green and red filled squares respectively for comparison). The open (filled) circle corresponds to the measurement by Eigenbrod et al. (2008) with (without) a velocity prior. Straight lines correspond to the measurements by Poindexter & Kochanek (2010a) (dashed line), Sluse et al. (2011) (dotted-dashed line) and Mosquera et al. (2013) (continuous line), that have no estimate on p; the associated error bars correspond to their $\pm 1\sigma$ uncertainties. The size comparisons have been made setting the mean mass of the stars to $\langle M \rangle = 0.3\,\mathrm{M}_\odot$.

recent size estimates for two local AGN using measurements of continuum lags (Edelson et al. 2015; Fausnaugh et al. 2015; Shappee et al. 2014). The size problem is clearly not unique to the microlensing method.

The hybrid and thin disk models both find $p = 1.0 \pm 0.3$ for the slope of the dependence of the disk size on wavelength, while the Gaussian model favors a steeper (in temperature) slope of $p = 0.7 \pm 0.3$. The three estimates are mutually compatible and smaller than the prediction of the standard thin disk model ($p = 4/3$). The differences for the (presumably) more physical hybrid or thin disk models are small enough to represent only a modest inconsistency. Experiments with broader wavelength ranges are needed to provide better estimates of the temperatures exponent.

Chapter 3

Observations of Q 2237+0305 in the mid infrared

We present new mid-IR observations of the quadruply lensed quasar Q 2237+0305 taken with CanariCam on the Gran Telescopio Canarias (GTC). Mid-IR emission by hot dust, unlike the optical and near-IR emission from the accretion disk, is unaffected by the interstellar medium (extinction/scattering) or stellar microlensing. We compare these "true" ratios to the (stellar) microlensed flux ratios observed in the optical/near-IR to constrain the structure of the quasar accretion disk. We find a half-light radius of $R_{1/2} = 3.4^{+5.3}_{-2.1}\sqrt{\langle M\rangle/0.3\,\mathrm{M}_\odot}$ light-days at $\lambda_{rest} = 1736$ Å, and an exponent for the temperature profile $R \propto \lambda^p$ of $p = 0.79 \pm 0.55$ where $p = 4/3$ for a standard thin disk model. If we assume that the differences in the mid-IR flux ratios measured over the years are due to microlensing variability, we find a lower limit for the size of the mid-IR-emitting region of $R_{1/2} \gtrsim 200\,\sqrt{\langle M\rangle/0.3\,\mathrm{M}_\odot}$ light-days. We also test for the presence of substructure/satellites by comparing the observed mid-IR flux ratios with those predicted from smooth lens models. We can explain the differences if the surface density fraction in satellites near the lensed images is $\alpha = 0.033^{+0.046}_{-0.019}$ for a singular isothermal ellipsoid plus external shear mass model or $\alpha = 0.013^{+0.019}_{-0.008}$ for a mass model combining ellipsoidal NFW and de Vaucouleurs profiles in an external shear.

This chapter is based on the article *Observations of the Lensed Quasar Q 2237+0305 with CanariCam at GTC* by Vives-Arias, H., Muñoz, J. A., Kochanek, C. S., Mediavilla, E. & Jiménez-Vicente, J. (2016), *ApJ*, **831**, 43.

3.1 The need for mid-IR fluxes

Gravitational lenses are a very powerful tool for many astrophysical and cosmological studies (e.g. see the review by Kochanek 2006). In particular, multiply imaged quasars allow us to probe the mass distribution and interstellar medium (ISM) of the galaxy as well as properties of the quasar itself that are hard to characterize otherwise. The flux ratios of the images, one of their most easily measured properties, are controlled not only by the smooth gravitational potential of the lens but also by perturbations produced by stars (microlensing) and satellites/cold dark matter (CDM) substructure (millilensing), as well as propagation effects in the lens (scattering/extinction). As a result, smooth lens models almost always fail to fit image flux ratios and thus are rarely used as model constraints, even though they encode important astrophysical information.

Optical and near-IR observations are affected by differential extinction between the lensed images (e.g. Elíasdóttir et al. 2006; Falco et al. 1999; Muñoz et al. 2004; Nadeau et al. 1991). While we can try to correct for this by fitting extinction models, microlensing by the stars in the lens galaxy also produces color changes between images that can mimic extinction (e.g. Mosquera et al. 2009; Muñoz et al. 2011; Poindexter et al. 2008), so the two effects cannot be fully separated. Radio lenses generally avoid this problem (see Kochanek & Dalal 2004), although there are clear examples of images that are scatter broadened (e.g. Sykes et al. 1998). Unfortunately, radio lenses are also a minority of lenses and in many cases lack the ancillary information needed to make them useful astrophysical probes (redshifts and well-studied lens galaxies). Mid-IR wavelengths are almost ideal for measuring the intrinsic flux ratios of lensed images. They are too long (short) to be affected by extinction (electrons), thereby eliminating the ISM as a factor affecting the flux ratios. Because the mid-IR emission is dominated by hot dust, which is destroyed if too close to the quasar (e.g. Barvainis 1987), the mid-IR emission regions should also be large enough to be little affected by microlensing, leaving only the magnifying effects of the smooth lens potential and substructure (satellites). However, one must proceed with caution, because mid-IR flux ratios could still be affected by microlensing of the dusty torus taking place in timescales of decades or centuries (Stalevski et al. 2012). Also, if the accretion disk of the quasar has a contribution to the mid-IR emission, microlensing of this small region by the stars of the lens galaxy could have a measurable effect on the mid-IR flux of the lensed images (Sluse et al. 2013).

If these effects are negligible, then the deviations of the mid-IR flux ratios from models would primarily probe the mean gravitational potential of the lens and the effects of substructure. This is astrophysically important because the amount of substructure in CDM haloes is an open question. Simulations suggest that 10% of the mass remains in satellites, with the fraction dropping closer to 1% in the inner regions as tidal effects destroy the satellites (e.g. Zentner & Bullock 2003), in contradiction with the observations

Table 3.1. Log of Q 2237+0305 observations with CanariCam

Date	Filter	Readout mode	Exposure (s)	Notes
2012 Jun 6	N-10.36	S1R1_CR	1001.9	Detected, non-Gaussian noise
2012 Jul 10	N-10.36	S1R1_CR	3×675.3	Detected, non-Gaussian noise
2013 Sep 4	Si5	S1R3	3×595.7	Nondetection
2013 Sep 18	Si5	S1R3	3×1853.3	Detected, low S/N in third image
2013 Sep 19	Si5	S1R3	2×1522.4	Detected

of the Milky Way halo (Klypin et al. 1999; Moore et al. 1999). Although the gap has been reduced somewhat in the past decade with the discovery of a new population of Milky Way faint satellites (Belokurov et al. 2006; Koposov et al. 2015; Zucker et al. 2006), and new estimations of the mass of our galactic halo lower the predicted subhalo population at the high-mass end (Kafle et al. 2014; Wang et al. 2012), the discrepancy still exists. Gravitational lensing is one of the only means of detecting dark substructures, and results from studying anomalous flux ratios in radio lenses (Dalal & Kochanek 2002; Kochanek & Dalal 2004; Vegetti et al. 2012) suggest that the missing satellites are present. However mid-IR observations are available for only six lenses (Agol et al. 2000, 2001, 2009; Chiba et al. 2005; MacLeod et al. 2009, 2013; Minezaki et al. 2009).

3.2 Observations and Data analysis

The lens system Q 2237+0305 (described in detail in Section 2.1) was observed in mid-IR using the CanariCam instrument on Gran Telescopio CANARIAS (GTC), located at the Roque de los Muchachos Observatory, La Palma (Spain), in July 2012 and September 2013. CanariCam has a field of view of $25\farcs6 \times 19\farcs2$ with a spatial scale of $0\farcs08$ pixel^{-1}. For the filters we use, the resolution is diffraction limited by the 10.4 m primary mirror of GTC. For all observations, we set a chopping position angle of 53 degrees, a nodding position angle of -127 degrees, and a throw of $10''$ for both motions. The mid-IR standard stars HD 220009 and HD 220954 were observed for each epoch of observation to be used as point-spread function (PSF) templates for the data reduction.

A test image was obtained on June 6th, 2012 with an on-source exposure time of 1001.9 seconds using the S1R1_CR readout mode, a chopping frequency of 2.05 Hz, and the N-10.36 filter ($\lambda_c = 10.36\mu$m, $\Delta\lambda = 5.2\mu$m). Since the object was successfully detected, three more images with on source exposure times of 675.3 seconds each and a chopping frequency of 2.01 Hz were obtained on July 30th, 2012. The S1R1_CR mode, however, introduced a non-Gaussian horizontal noise pattern in the images that makes it

difficult to accurately measure the fluxes of targets with low signal-to-noise ratios (S/N). The horizontal bands could be removed in the area of interest by selecting a range of columns with the same noise pattern as the region of the image where the target is located, averaging them and subtracting the pattern from the whole image. However, since we are interested in measuring flux ratios between images at different locations on the image, it is better to avoid this kind of noise altogether.

For the next set of observations, we switched to the newly available S1R3 readout mode, in which the noise pattern has a more Gaussian structure and the same properties along lines and columns. Unfortunately, the new mode also uses longer frame times, leading to high backgrounds that more easily saturate the detector. As a result, the N filter is not recommended for use in this mode unless the precipitable water vapor (PWV) is below 3 mm (which happens only around 2% of the observing time). For this reason, for the rest of observations we switched to the narrower Si5 filter ($\lambda_c = 11.6\mu$m, $\Delta\lambda = 0.9\mu$m). On September 4th, 2013, three images were obtained with on-source exposure times of 595.7 seconds each and a chopping frequency of 2.07 Hz, but the target was not detected due to the smaller width and lower transmission of the Si5 filter. We then increased the exposure times for a last set of observations using the same configuration to obtain three images on September 18th and two images on September 19th with total on-source exposure times of 3×1853.3 and 2×1522.4 seconds respectively. A summary of all our observations can be found in Table 3.1.

The data were reduced by first aligning the images from each night of observation and then separately combining the images from the 2012 and 2013 observations. To determine the offset between the individual images for the alignment, we performed PSF fitting relative to the known locations of the quasar images from the *Hubble Space Telescope* (HST) observations available on the CASTLES website[1]. The final combined image (Figure 3.1) used only the 2013 observations due to their better instrumental conditions, excluding the third image from September 18th which had a very poor S/N due to a significant rise in the PWV. Experiments including this third image and/or the shorter exposures from September 4th did not lead to improved results. The raw FWHM of the quasar images is $0\farcs24$ which we have smoothed with a Gaussian kernel of $\sigma = 0\farcs12$ for Figure 3.1.

3.3 Flux ratios

The flux ratios of the lensed images were obtained using PSF-fitting photometry from the combined 2013 image. The scatter between the results from applying this same procedure to the individual noncombined images was used to estimate the errors. The final flux ratios are B/A $= 0.99 \pm 0.03$, C/A $= 0.69 \pm 0.10$, and D/A $= 0.84 \pm 0.13$. Since the

[1] http://www.cfa.harvard.edu/glensdata/

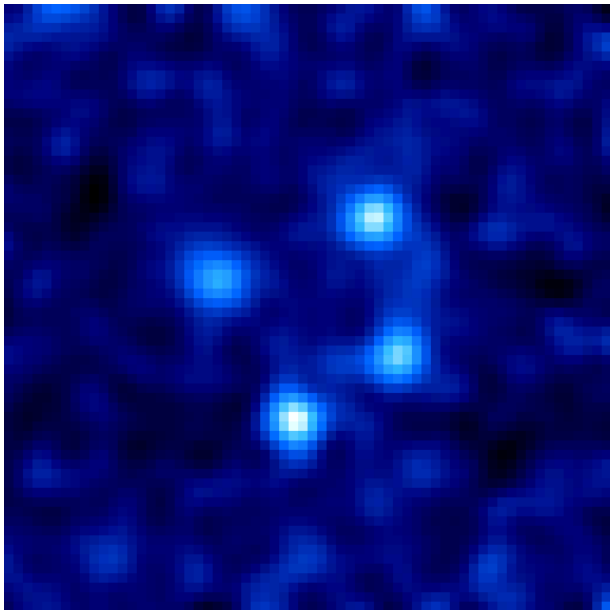

Figure 3.1 The quadruple lens system Q 2237+0305 at 11.6μm using data taken with CanariCam at GTC on 2013 September 18 and 19 (UT). The pixel scale is 0.″08 pixel^{-1} and the image subtends 5.″12. North is up, east is left, and the quasar images are, starting from top right and moving clockwise, B, D, A, and C, respectively. This image has been smoothed with a Gaussian kernel of $\sigma = 0.''12$ in order to improve the contrast relative to the noise.

Table 3.2. Flux ratios of Q 2237+0305

Reference†	Date	Wavelength / Model	Flux Ratio		
			B/A	C/A	D/A
This work	2013 Sep 18, 19	11.6 μm	0.99 ± 0.03	0.69 ± 0.10	0.84 ± 0.13
This work	2012 Jul 10	10.36 μm	0.96 ± 0.11	0.57 ± 0.06	1.04 ± 0.21
1	2005 Nov 17	8.0 μm	0.93 ± 0.07	0.59 ± 0.04	0.84 ± 0.08
2	2005 Oct 11, 12	11.7 μm	0.84 ± 0.05	0.46 ± 0.02	0.87 ± 0.05
3	2000 Jul 11	11.7 μm	1.11 ± 0.09	0.72 ± 0.07	1.17 ± 0.09
4	1999 Jul 28, Sep 24	8.9 & 11.7 μm	1.11 ± 0.11	0.59 ± 0.09	1.00 ± 0.10
4	1999 Sep 24	11.7 μm	0.91 ± 0.30	0.41 ± 0.21	0.66 ± 0.27
4	1999 Sep 24	8.9 μm	0.88 ± 0.28	0.51 ± 0.22	1.05 ± 0.31
4	1999 Jul 28	11.7 μm	1.07 ± 0.25	0.61 ± 0.16	1.09 ± 0.25
4	1999 Jul 28	8.9 μm	1.42 ± 0.33	0.66 ± 0.20	1.09 ± 0.27
Average	2013, 2005, 2000 & 1999	8.0 - 11.7 μm	0.97 ± 0.03	0.51 ± 0.02	0.92 ± 0.04
This work		SIE + γ (no flux)[1]	0.89	0.45	0.82
This work		SIE + γ (GTC)	0.89	0.45	0.84
This work		SIE + γ (average)	0.89	0.48	0.89
This work		NFW + de Vaucouleurs (no flux)[1]	0.88	0.48	0.87
This work		NFW + de Vaucouleurs (GTC)	0.88	0.50	0.90
This work		NFW + de Vaucouleurs (average)	0.94	0.51	0.91
5		Bulge + disk + halo + bar	1.02	0.56	1.19

†1. Agol et al. 2009; 2. Minezaki et al. 2009; 3. Agol et al. 2001; 4. Agol et al. 2000; 5. Trott et al. 2010.

[1]Best fit when taking only the images and galaxy positions as constraints.

2012 observations give self-consistent flux ratios that differ from the 2013 observations, this difference was also taken into account in the final error estimation.

As shown in Table 3.2, our measured B/A and C/A flux ratios differ significantly from the ones obtained by Minezaki et al. (2009) at $\lambda = 11.67\mu$m in October 2005 with Subaru. Interestingly, they are compatible at the 1σ level with the ratios measured by Agol et al. (2009) at $\lambda = 8.0\mu$m in November 2005 with the *Spitzer Space Telescope*. Previous observations at $\lambda = 11.7\mu$m from November 2000 with the Long Wavelength Spectrometer on Keck by Agol et al. (2001) yielded flux ratios that are inconsistent with the ones measured by Minezaki et al. (2009), but much closer to our estimates. Only the D/A flux ratio shows a significant difference.

The flux ratios measured by Minezaki et al. (2009) are in agreement with the prediction yielded by a simple singular isothermal ellipsoid (SIE) plus external shear (γ) model without the need for any additional structure when taking only the HST image positions as constraints. On the other hand, the Trott et al. (2010) mass model, consisting of a galactic bulge, bar, and disk combined with a dark matter halo fitted to the image positions and the observed kinematics of the galaxy but not the flux ratios, predicts fluxes that are closer to the ones observed by Agol et al. (2000). We discuss the consequences of these flux ratio differences further in Section 3.5.2.

3.4 Mass modeling

The positions and relative fluxes of the quasar images, when not affected by microlensing, are determined by the distribution of the mass in the lens galaxy and the distances between observer, lens and source. Once measured from mid-IR observations, then, these positions and fluxes can serve as constraints to apply when fitting mass models to the lens galaxy.

To see the effect that our new flux ratios would have in the determination of the mass distribution in the lens galaxy, we use them as constraints for mass modeling with the Gravlens/Lensmodel code (Keeton 2001, 2011). However, despite obtaining a very low scatter for the B/A ratio in all of our images and therefore small uncertainties for it, in order to account for the possibility that this arose by chance due to the noise variation, we set an error of 0.10 in all three of our flux ratios for these calculations. We fit a simple SIE + γ profile and then a more elaborate model with a Navarro, Frenk & White (NFW) dark matter halo and a de Vaucouleurs profile for the bulge and bar of the lens galaxy. To reduce the number of free parameters on the second model, we set constraints for the ellipticity (e) and position angle (θ_e) of the de Vaucouleurs profile measured from HST photometry. A more relaxed condition was set for the effective radius (R_e), since this can vary among different filters. The parameters for the break radius r_s and the surface density at the break radius κ_s of the NFW profile are constrained to be close to those obtained by Trott et al. (2010) for their more detailed model, which correspond to a halo of virial mass $10^{12} M_\odot$ and we favored models with a small ellipticity to avoid unphysical solutions. As can be seen in Table 3.2, the mid-IR flux ratios reported by different authors and at different epochs are not mutually consistent given their uncertainties. For comparison to simply using the estimate from our new data, we repeat the model fittings using an error-weighted average of all the available mid-IR data (the "average" entry in Table 3.2). Finally, we fit the models only to the image positions without including the flux ratios as constraints (designated as "no flux" in the tables).

For our GTC flux ratios with uncertainties set to 0.1, the goodness of the fit is $\chi^2_{red} = 0.973$ for the SIE + γ model, and $\chi^2_{red} = 0.686$ for the NFW + de Vaucouleurs. The weighted average fluxes with their small uncertainties are harder to reproduce with these smooth models, and we get $\chi^2_{red} = 2.03$ with the SIE + γ and $\chi^2_{red} = 0.791$ when using the NFW + de Vaucouleurs models. Finally, when not using the flux ratios as constraints we have extra degrees of freedom leading to an over-fitting of the data, with $\chi^2_{red} = 0.00144$ and $\chi^2_{red} = 0.0066$ respectively, but the fluxes predicted will be useful for later comparisons. In all cases we get $\chi^2_{red} < 1$ when fitting an NFW + de Vaucouleurs, which would indicate an overfitting or an overestimation of the uncertainties, but this could be due to the large range of freedom we gave to some of the parameters. Since we have considered the constraints as data points when calculating the number of degrees

Table 3.3. Model fits to Q 2237+0305

Model/ component	Parameter	Constraint	Values GTC	Values Average	Values No flux
SIE + γ	b (arcsec)		$0.857^{+0.006}_{-0.007}$	0.865 ± 0.004	$0.854^{+0.007}_{-0.008}$
	x_0 (arcsec)	-0.075 ± 0.003	-0.076 ± 0.003	-0.079 ± 0.003	-0.075 ± 0.003
	y_0 (arcsec)	0.939 ± 0.003	0.9387 ± 0.0015	0.9383 ± 0.0015	0.9388 ± 0.0015
	e		$0.36^{+0.03}_{-0.04}$	0.30 ± 0.02	0.37 ± 0.04
	θ_e (°)		-64.7 ± 0.6	$-63.9^{+0.8}_{-0.7}$	-64.9 ± 0.6
	γ		$0.013^{+0.007}_{-0.004}$	0.015 ± 0.004	$0.015^{+0.009}_{-0.006}$
	θ_γ (°)		53^{+22}_{-13}	84^{+9}_{-13}	47^{+22}_{-11}
NFW halo	κ_s	0.010 ± 0.006	0.010 ± 0.006	$0.015^{+0.005}_{-0.004}$	0.010 ± 0.006
	x_0 (arcsec)	-0.075 ± 0.003	-0.075 ± 0.003	-0.075 ± 0.003	-0.075 ± 0.003
	y_0 (arcsec)	0.939 ± 0.003	0.939 ± 0.003	0.939 ± 0.003	0.939 ± 0.003
	e	0.00 ± 0.25	$0.04^{+0.26}_{-0.04}$	$0.52^{+0.13}_{-0.18}$	0.00 ± 0.25
	θ_e (°)		46^{+38}_{-45}	49^{+10}_{-9}	30^{+51}_{-120}
	γ		$0.016^{+0.010}_{-0.011}$	$0.031^{+0.012}_{-0.013}$	$0.023^{+0.036}_{-0.008}$
	θ_γ (°)		-84^{+8}_{-6}	-52 ± 11	-79 ± 11
	r_s (arcsec)	33.66 ± 10.00	35^{+9}_{-11}	33^{+11}_{-9}	34 ± 10
de Vaucouleurs	b		1.35 ± 0.07	$1.33^{+0.05}_{-0.06}$	$1.39^{+0.16}_{-0.08}$
	x_0 (arcsec)	-0.075 ± 0.003	-0.075 ± 0.003	-0.075 ± 0.003	-0.075 ± 0.003
	y_0 (arcsec)	0.939 ± 0.003	0.9396 ± 0.0016	0.9386 ± 0.0016	$0.9394^{+0.0018}_{-0.0019}$
	e	0.33 ± 0.20	0.31 ± 0.03	0.32 ± 0.02	0.33 ± 0.04
	θ_e (°)	-65.6 ± 20.0	$-64.5^{+0.6}_{-0.7}$	$-64.7^{+0.8}_{-0.7}$	$-64.7^{+0.8}_{-0.6}$
	R_e (arcsec)	4.72 ± 4.00	6.1 ± 2.6	$6.5^{+2.5}_{-1.9}$	5^{+4}_{-3}

of freedom, this mimics the effects of an overestimation of the error margins in the data. Table 3.3 shows the model components and the values obtained for each of their parameters in the best fits, and the flux ratios they predict are shown in Table 3.2.

Most of our models predict flux ratios that are very similar to the ones predicted by a simple SIE + γ constrained by the images and galaxy positions only. The exception is when we fit the NFW + de Vaucouleurs model to the weighted average of all mid-IR flux ratios, which reproduces them well but at the cost of a very large and unrealistic ellipticity of $e = 0.52^{+0.13}_{-0.18}$ for the NFW halo. Something similar happens if we set B/A $= 0.99 \pm 0.03$ in our 2013 observations, where our best fit to reproduce the flux ratios has an ellipticity of $e = 0.64$. The SIE + γ model is unable to reproduce the average fluxes, and in fact the χ^2_{red} for that fit is dominated by the flux ratios. If the weighted average of the flux ratios is a good estimate of the real intrinsic ones, then it could indicate that more

complex models including the bar, disk and other components are needed, or that there might be flux anomalies caused by substructure in the dark matter halo. We analyze this possibility further in Section 3.6.

3.5 Source size estimations using microlensing

3.5.1 Accretion disk size

Since the magnitude of the microlensing of the quasar images depends on the projected size of the source compared to the average Einstein radius of the microlenses, microlensing can be used to determine the size of the accretion disk, or other emission regions. The temperature of the disk is also expected to increase radially toward the center, so observations in different optical bands should give different results because shorter wavelengths correspond to smaller, more central higher-temperature regions of the disk. These chromatic effects can be used to determine the scaling slope of the radial dependence for the temperature.

In the previous chapter we use a Bayesian analysis of narrowband filter observations of Q 2237+0305 in the range 4670-8130 Å and previous mid-IR observations as an estimate of the intrinsic flux ratios, to estimate two parameters of the disk, its half-light radius ($R_{1/2}$) and the logarithmic scaling slope (p) of its temperature profile $T \propto R^{-1/p}$. Muñoz et al. (2016) found, as expected from earlier studies (Mortonson et al. 2005), that the half-light radius ($R_{1/2}$) estimates are independent of the surface brightness profile. Here we recalculate these two disk parameters using our new mid-IR observations and the method described in Section 2.2. We assumed a standard thin disk model, $I(R) \propto \left(\exp\left[(R/r_s)^{3/4}\right] - 1\right)^{-1}$ with the disk radius varying with wavelength as $r_s(\lambda) = (\lambda/\lambda_0)^p\, r_s(\lambda_0)$, where $\lambda_0 = 1736$ Å at the rest frame. We used 2000×2000 microlensing magnification maps computed using the Inverse Polygon Mapping algorithm (Mediavilla et al. 2006, 2011a) with 0.5 light-day pixels and $1\,\mathrm{M}_\odot$ stars. All linear sizes can be scaled to a different mass as $(\langle M\rangle/\mathrm{M}_\odot)^{1/2}$ and microlensing results are generally insensitive to the mass function (e.g. Wyithe et al. 2000). The maps were then convolved with the disk model using the appropriate size $r_s(\lambda)$ for each wavelength and for each pair of parameters (r_s, p) from a 2D grid of values such that $\ln(r_s^i/\text{light-days}) = 0.3 \times i$ for $i = 0, \cdots, 17$ and $p^j = 0.25 \times j$ for $j = 0, \cdots, 9$. For each case we then selected $N = 10^8$ random locations in each of the four maps, computed the microlensing magnifications for the different filters, and compared them to the narrowband observations for each epoch. Since this method relies on changes in the microlensing amplitude with wavelength and size but not on its dependence with time, no velocity estimates are necessary. For every

image $I = (A, B, C, D)$, observed at time t_j and filter i, the goodness of the fit is

$$\chi^2(t_j, i) = \sum_I \sum_{J>I} \sigma_{IJ}(t_j, i)^{-2} [\Delta m_I(t_j, i) - \Delta m_J(t_j, i)]^2 \tag{3.1}$$

where

$$\Delta m_I(t_j, i) = m_I^{obs}(t_j, i) - \mu_I - \delta\mu_I(t_j, i), \tag{3.2}$$

$m_I^{obs}(t_j, i)$ are the data, μ_I is the macro magnification, $\delta\mu_I(t_j, i)$ is the microlensing magnification, and $\sigma_{IJ}(t_j, i)$ are the errors as defined in the equation 7 of Kochanek (2004b). As described in Muñoz et al. (2016), these errors reduce to $\sigma_{IJ}(t_j, i) = 2\,\sigma(t_j, i)$ if $\sigma_I = \sigma_J (\equiv \sigma)$, and we have chosen to use the average measurement errors of $\sigma = 0.08$ mag for weighting all the data. From this, we estimate the probability density function $\mathcal{P}(r_s, p)$.

Here we use our new mid-IR flux ratios as the intrinsic flux ratios $\mu_{IJ}^{ir} = \mu_I - \mu_J$, instead of those from Minezaki et al. (2009). The results for the expected values of the disk parameters are $r_s = 1.40^{+2.19}_{-0.85}\sqrt{\langle M\rangle/0.3\,\mathrm{M}_\odot}$ light-days (equivalent to a half-light radius $R_{1/2} = 3.4^{+5.3}_{-2.1}\sqrt{\langle M\rangle/0.3\,\mathrm{M}_\odot}$ light-days) and $p = 0.79 \pm 0.55$, where we have scaled the results to a mean stellar mass of $\langle M\rangle = 0.3\,\mathrm{M}_\odot$. A logarithmic slope of $p = 4/3$ corresponds to a standard thin disk. As can be seen in Table 3.2 and discussed in Section 3.3, the mid-IR flux ratios reported by different authors and at different epochs are not mutually consistent given their uncertainties. For comparison to simply using the estimate from our new data, we repeated the calculation using an error-weighted average of all the available mid-IR data (the "average" entry in Table 3.2). In this case we obtain a scale radius of $r_s = 2.5^{+3.0}_{-1.4}\sqrt{\langle M\rangle/0.3\,\mathrm{M}_\odot}$ light-days, a half-light radius of $R_{1/2} = 6.2^{+7.4}_{-3.4}\sqrt{\langle M\rangle/0.3\,\mathrm{M}_\odot}$ light-days, and $p = 0.95 \pm 0.39$. Figure 3.2 shows the contours of the probability density function using this weighted average along with the results using only our new mid-IR flux ratios, as well as our earlier results from Muñoz et al. (2016) using the Minezaki et al. (2009) flux ratios. Despite the differences in the mid-IR flux ratios, all these estimates for $R_{1/2}$ and p are mutually consistent.

3.5.2 Size of the mid-IR emitting region

The small changes observed in the mid-IR flux ratios over time are likely dominated by systematic errors, but an alternative explanation is that it consists of variability induced by stellar microlensing of the mid-IR emission (Sluse et al. 2013). If we assume that this variability is indeed due to microlensing, we can then infer the size of the emitting region using a similar method to the one above. For this analysis we have generated magnification maps for the four lensed images of the quasar that are 2000×2000 pixels with a size of 4 light-days pixel^{-1} for stars with a mass of $\langle M\rangle = 1\,\mathrm{M}_\odot$. We then convolve them with simple Gaussian models for the source, $I(R) \propto \exp(-R^2/2r_s^2)$, such that

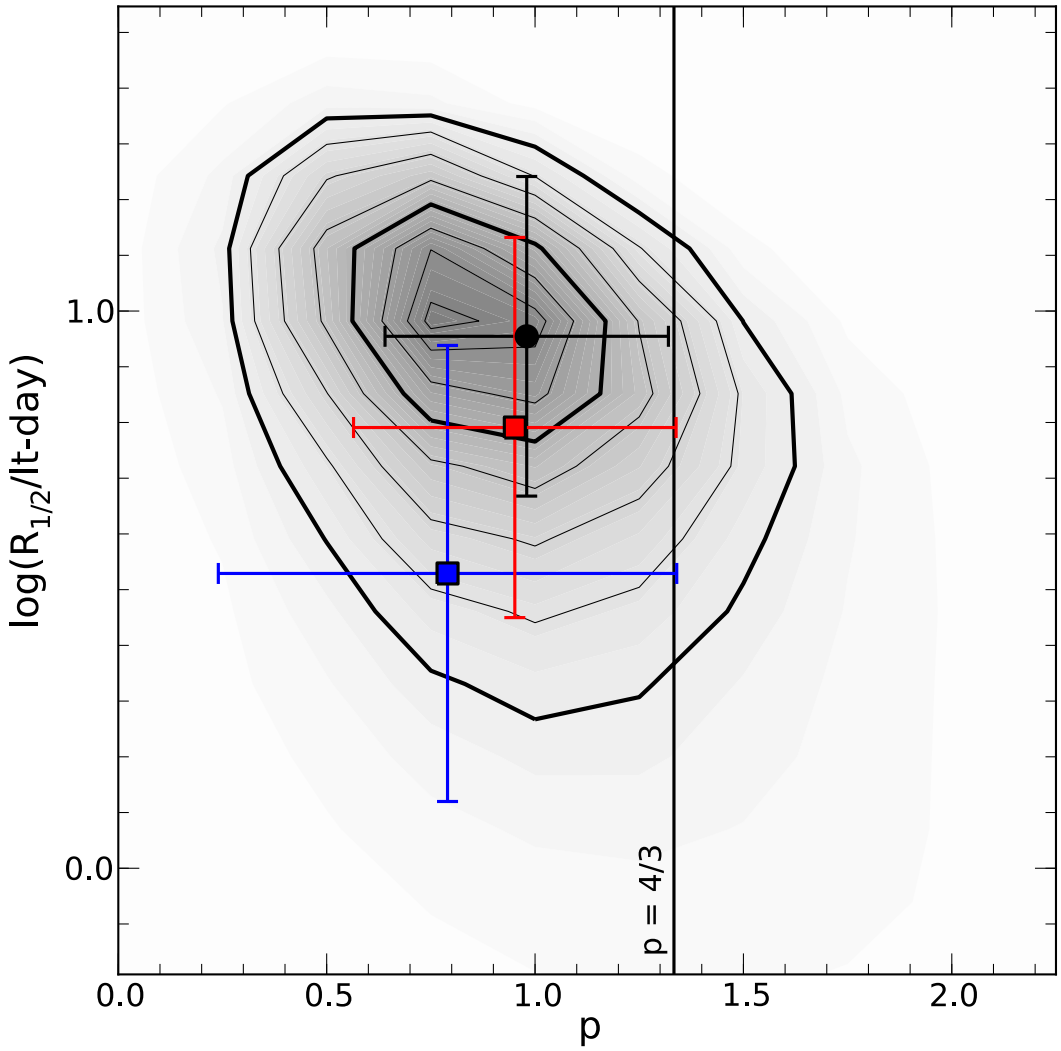

Figure 3.2 Joint probability density function $\mathcal{P}(r_s, p)$ for the half-light radius $R_{1/2} = 2.44 r_s$ (at rest $\lambda_0 = 1736$ Å) and the logarithmic slope p ($r_s \propto \lambda^p$) for the disk model using the weighted average of the mid-IR flux ratios from Agol et al. (2000), Agol et al. (2001), Minezaki et al. (2009), Agol et al. (2009) and this work. The separation between consecutive contours corresponds to 0.25σ, and the 1σ and 2σ contours for one parameter are heavier. The red filled square is the Bayesian estimate for the expected values of $R_{1/2}$ and p for the averaged mid-IR flux ratios, and the blue filled square is the result of the same calculation using our 2013 mid-IR observations only. The black filled circle corresponds to the measurement by Muñoz et al. (2016) using the mid-IR flux ratios from Minezaki et al. (2009). All sizes are scaled to a mean stellar mass of $\langle M \rangle = 0.3\,\mathrm{M}_\odot$. The $p = 4/3$ vertical line coincides with the temperature slope for the standard thin accretion disk model.

$\log_{10}(r_s^i/\text{light-days}) = 1 + 0.15 \times i$ for $i = 0, \cdots, 19$, and the values of r_s span from 10 to roughly 7000 light-days. Using the weighted average of all observations as an estimate for the baseline with no microlensing and a logarithmic prior, we obtain a Bayesian estimate for the scale radius of the Gaussian source of $r_s = 194^{+171}_{-91}\sqrt{\langle M\rangle/0.3\,\mathrm{M}_\odot}$ light-days, which corresponds to a half-light radius of $R_{1/2} = 228^{+201}_{-107}\sqrt{\langle M\rangle/0.3\,\mathrm{M}_\odot}$ light-days. We have also repeated the calculations using the radio flux ratios from Falco et al. (1996) to define the intrinsic flux ratios. Because of the large uncertainties on the radio fluxes, we obtain only a lower limit for the size of the mid-IR emission, with $R_{1/2} > 340\,\sqrt{\langle M\rangle/0.3\,\mathrm{M}_\odot}$ light-days. The probability density functions for these estimates can be seen in Figure 3.3.

Since the mid-IR wavelengths correspond to $\lambda \sim 4$ μm in the rest frame, the main contribution to the mid-IR emission in this lensed quasar should be dust emission. Dust cannot be closer to the central engine than the point where it would be heated to its evaporation temperature. For a simple thermal equilibrium, ignoring Planck factors, this corresponds to a radius of $r_{min} \simeq 730 L_{46}^{1/2} T_{d3}^{-2}$ light-days where the luminosity of the AGN is $L = 10^{46}\ L_{46}$ erg s^{-1} and the destruction temperature is $T_d = 1000\,T_{d3}$ K. Agol et al. (2009) estimated a luminosity of $L = 4 \times 10^{46}$ erg s^{-1} corresponding to $r_{min} \simeq 1500\,T_{d3}^{-2}$ light-days. Mid-IR interferometric observations of AGNs point to a torus size of approximately $R_{1/2} \lesssim 3$ pc for this luminosity (Burtscher et al. 2013). Also, the time scale for microlensing variability of the emission from a torus this large would be many decades rather than years, reducing the likelihood that the differences can be due to microlensing (Stalevski et al. 2012). This suggests that our default hypothesis, that the apparent "variability" is really an indication that there are systematic errors in the mid-IR fluxes (or their uncertainties), is likely correct, and we should view these estimates for the size of the dusty torus just as a lower limit with $R_{1/2} \gtrsim 200\,\sqrt{\langle M\rangle/0.3\,\mathrm{M}_\odot}$ light-days. Sluse et al. (2013), however, find that by extending the Shakura & Sunyaev accretion disk model to mid-IR wavelengths and including it in the source models, the probability of microlensing by the stars contributing to variations of the total measured mid-IR flux up to around 0.1 mag is not negligible even for an AGN of this luminosity, especially in the case of $\kappa_*/\kappa = 1$. If the mid-IR variability is real and not due to systematic errors, then it could be due to stellar microlensing of the accretion disk. This might also help to explain the significantly different flux ratios measured by Agol et al. (2009) and Minezaki et al. (2009) from observations less than a month apart as microlensing chromaticity between 8.0 μm and 11.7 μm. In fact, Agol et al. (2009) explicitly show the presence of chromatic microlensing in their mid-IR fluxes in several bands.

3.6 Dark matter substructure

Beyond problems in the macro models, the alternate interpretation of differences between the mid-IR flux ratios and smooth models is magnification perturbations due to

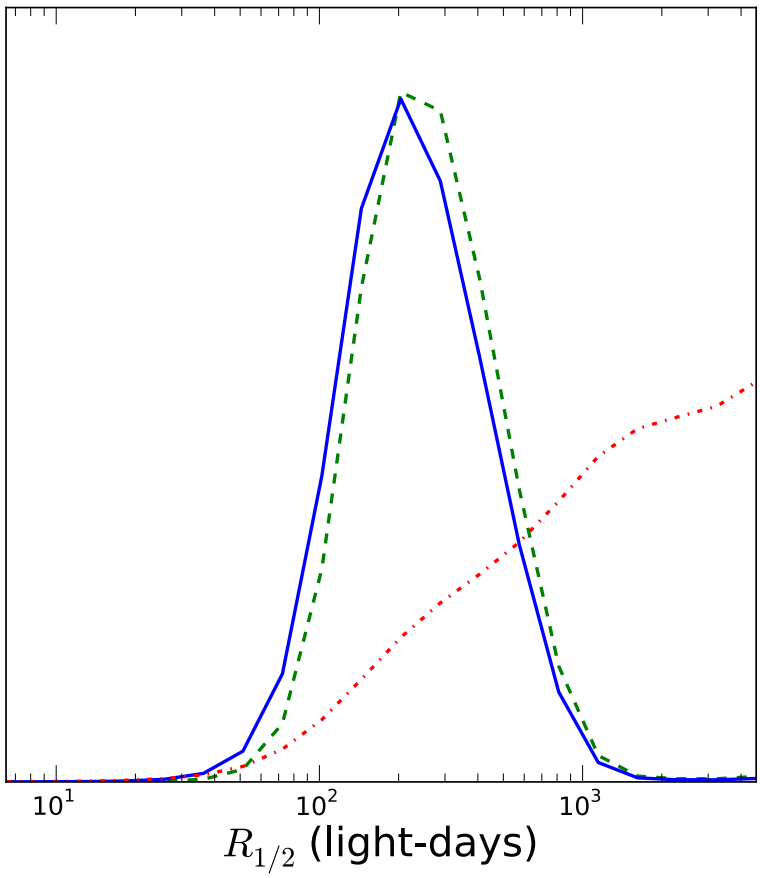

Figure 3.3 Probability density functions for the size of the mid-IR emitting region of the AGN assuming that the variability of the flux ratios in different observations (Table 3.2) is due to microlensing by stars in the lens galaxy, and a Gaussian source of the form $I(R) \propto \exp(-R^2/2r_s^2)$. The solid blue line corresponds to the estimate using as a non-microlensed baseline the weighted average of the mid-IR flux ratios from Agol et al. (2000), Agol et al. (2001), Minezaki et al. (2009), Agol et al. (2009) and our 2013 fluxes. The dashed green line is the same calculation but adding our 2012 observations as an extra epoch, and the dotted line is the result of using the radio observations from Falco et al. (1996) as the intrinsic flux ratios. All sizes correspond to a mean mass of the stars $\langle M \rangle = \mathrm{M}_\odot$.

substructure in the lens. In this section we will assume that the mid-IR flux anomalies between our observations and those predicted by our simple smooth SIE+γ or NFW+de Vaucouleurs+γ models (when constrained only by the image positions) are caused by (dark matter) subhaloes orbiting the lens galaxy and acting as "millilenses". The goal is to estimate $\beta = b/b_0$, the ratio of their average Einstein radius b to that of the lens galaxy b_0, and their abundance α, the fraction of the lensing convergence κ that is in the form of subhaloes. Since we are using only magnifications, we should not be able to determine β, but should be able to constrain α.

For each pair (α, β) we calculate magnification maps for each of the images of the quasar using the Inverse Polygonal Mapping algorithm, but this time the mass is in Pseudo-Jaffe density profiles $\rho \propto r^{-2}(r^2 + a^2)^{-1}$, see Muñoz et al. (2001), instead of point masses. We set the scale a as the tidal radius of the subhalo, $a = \sqrt{b\, b_0}$ (Dalal & Kochanek 2002). We use satellite mass fractions of $\alpha_j = 2^{-j}$ for $j = 2, \cdots, 8$ and the Einstein radius ratios of $\beta_i = b_0^{-1} \times 10^{-4} \times 2^i$ for $i = 0, \cdots, 8$. The mass of the individual subhaloes spans roughly from $2 \times 10^4\,\mathrm{M}_\odot$ to $8 \times 10^7\,\mathrm{M}_\odot$. Given the large size expected for the dusty torus (see discussion in section 3.5.2), we calculated magnification maps with a pixel scale of 1000 light-days and a size of 200×200 pixels. These regions are still small enough for the millilensing magnification maps associated with each image to be statistically independent. However, when the mass of the millilenses is at the upper end of our range and the abundance is low, only part of one caustic (if any) will be present, and for the smallest subhaloes and highest abundances the number of lenses can be so high as to create computational challenges. In the first case, the solution is to generate a larger number of maps to get good statistics, while in the latter case, the size of the map (and/or the area where the lenses are placed, since border effects will be less important when the mass distribution consists of very large numbers of very small subhaloes) has to be reduced. In any case, our approach assumes an upper limit on the subhalo masses to avoid both correlations between the magnification maps for different images and ray deflections so large that they would require modifications to the macrolens model. The procedure is explained in more detail in Section 5.3.

For each quasar image I, the millilensing magnification is

$$\Delta m_I^{obs} = m_I - m_0 - \mu_I \tag{3.3}$$

where m_0 is the unknown intrinsic magnitude of the source, m_I is the observed magnitude of image I, and μ_I is the macromodel magnification for that image. If we consider the millilensing magnifications on each of the quasar images as independent events, we can define the probability of observing microlensing magnifications Δm_I^{obs} conditioned to the parameters α and β as

$$P(\Delta m_I^{obs}|\alpha, \beta) = \prod_{I=A,B,C,D} P_I(\Delta m_I|\alpha, \beta) \tag{3.4}$$

where $P_I(\Delta m_I|\alpha,\beta)$ are the individual probability distribution functions (PDFs) for each image calculated from the magnification maps. If we then substitute equation 3.3 into equation 3.4 and marginalize over the unknown source magnitude m_0, we have

$$P_{marg}(m_I - \mu_I|\alpha,\beta) = \int \prod_{I=A,B,C,D} P_I(m_I - m_0 - \mu_I|\alpha,\beta)dm_0 \tag{3.5}$$

which we can calculate if m_0 is uniform over the range considered, since we have m_I from the mid-IR observations, and μ_I from the macromodel.

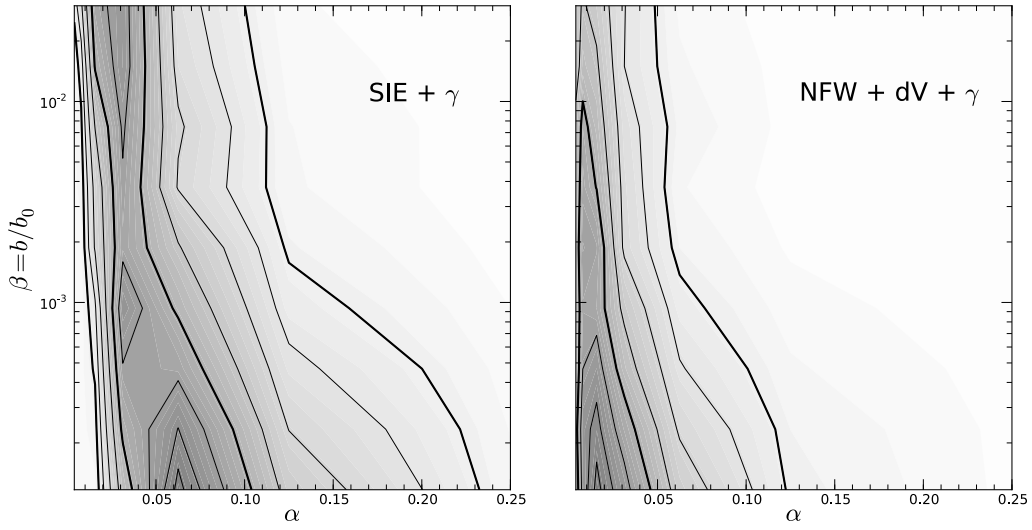

Figure 3.4 Probability densities for a distribution of (dark matter) subhaloes around Q 2237+0305 in terms of their local mass fraction α, and their Einstein radius b expressed as a fraction $\beta = b/b_0$ of the Einstein radius of the SIE profile that best fits the lens galaxy. The left panel uses the SIE + γ model and the right panel uses the NFW + de Vaucouleurs model. The separation between consecutive contours corresponds to 0.25σ, and the 1σ and 2σ contours for one parameter are heavier.

Figure 3.4 shows the resulting PDFs for α and β corresponding to the SIE+γ and NFW+de Vaucouleurs+γ lens models assuming that the true flux ratios are given by the weighted average of all mid-IR observations. We cannot estimate the mass scale of the subhaloes b; however, their mass fraction α is reasonably well constrained. The SIE+γ profile gives an estimate for the abundance of subhaloes $\alpha = 0.033^{+0.046}_{-0.019}$ (Figure 3.4, left). If we repeat the analysis with the prediction of the NFW+de Vaucouleurs+γ model, we obtain $\alpha = 0.013^{+0.019}_{-0.008}$ (Figure 3.4, right). This shows that a small amount of (dark

matter) substructure suffices to explain the flux ratio anomalies that smooth macromodels struggle to fit properly.

3.7 Discussion and Conclusions

We have measured the mid-IR flux ratios at 11.6μm (4.3μm in the rest frame) for the quadruple lens system Q 2237+0305 with the CanariCam imager at the GTC. Compared with previous results in the literature, we found moderately significant differences $\sim 2\sigma$ given the error estimates. Similar differences are seen between the various prior mid-IR flux ratio measurements. These differences have little effect on estimates of the properties of the quasar accretion disk. We repeated our estimates of the size and temperature profile of the disk from Muñoz et al. (2016). The results are mutually consistent whether we use the mid-IR flux ratios from Minezaki et al. (2009) that we used in Muñoz et al. (2016), our new mid-IR flux ratios, or the weighted average of all available flux ratios. In particular, we found a disk half-light radius of $R_{1/2} = 6.2^{+7.4}_{-3.4}\sqrt{\langle M\rangle/0.3\,\mathrm{M}_\odot}$ light-days at $\lambda_{rest} = 1736$ Å, and wavelength scale $R \propto \lambda^p$ of $p = 0.95 \pm 0.39$ using the weighted average of the flux ratios, where a standard thin disk model would have $p = 4/3$. These results are also consistent with previous estimates based on different approaches to the microlensing calculations (e.g. Poindexter & Kochanek 2010a, Sluse et al. 2011, Mosquera et al. 2013).

The observed variability of the mid-IR flux ratios in different epochs could be due to systematics, but we also considered microlensing by the stars in the lens galaxy as an alternative explanation. Under this hypothesis, we obtain an estimated size for the mid-IR emission region assuming a Gaussian source of $R_{1/2} = 228^{+201}_{-107}\sqrt{\langle M\rangle/0.3\,\mathrm{M}_\odot}$ light-days. This is smaller than the size expected for the mid-IR emitting dusty torus in the AGN. This could be due to either underestimated or systematic uncertainties in the mid-IR flux ratios or a residual contribution from microlensing of the more compact disk even at these wavelengths (Sluse et al. 2013). It is probably better to regard this estimate as a lower limit.

Finally, assuming that the observed mid-IR flux anomalies with respect to the predictions of simple macromodels are due to (dark matter) substructure, we estimate the mass fraction in satellites that would be needed to reproduce the mid-IR observations. For the flux ratios predicted by a SIE+γ model we found $\alpha = 0.033^{+0.046}_{-0.019}$, and for a NFW+de Vaucouleurs+γ model, $\alpha = 0.013^{+0.019}_{-0.008}$. As expected from simply fitting flux ratios, no constraint is found in the mass of the satellites. These results are consistent with CDM predictions (e.g. Zentner & Bullock 2003) and the observational results obtained by both Dalal & Kochanek (2002) and Vegetti et al. (2014). They also bring down the high estimate obtained by Metcalf et al. (2004) for Q 2237+0305 based on the narrow-line flux

ratios of this system.

Chapter 4

Detecting radio-quiet lensed quasars in radio

We present Very Large Array detections of radio emission in four four-image gravitational lens systems with quasar sources: HS 0810+2554, RX J0911+0511, HE 0435−1223 and SDSS J0924+0219, and extended Multi-Element Remote Linked Interferometer (e-MERLIN) observations of two of the systems. The first three are detected at a high level of significance, and SDSS J0924+0219 is detected. HS 0810+2554 is resolved, allowing us for the first time to achieve 10-mas resolution of the source frame in the structure of a radio quiet quasar. The others are unresolved or marginally resolved. All four objects are among the faintest radio sources yet detected, with intrinsic flux densities in the range 1–5μJy; such radio objects, if unlensed, will only be observable routinely with the Square Kilometre Array. The observations of HS 0810+2554, which is also detected with e-MERLIN, strongly suggest the presence of a mini-AGN, with a radio core and milliarcsecond scale jet. The flux densities of the lensed images in all but HE 0435−1223 are consistent with smooth galaxy lens models without the requirement for smaller-scale substructure in the model, although some interesting anomalies are seen between optical and radio flux densities. These are probably due to microlensing effects in the optical.

This chapter is based on the article *Observations of radio-quiet quasars at 10-mas resolution by use of gravitational lensing* by Jackson, N., Tagore, A. S., Roberts, C., Sluse, D., Stacey, H., Vives-Arias, H., Wucknitz, O. and Volino, F. (2015), *MNRAS*, **454**, 287. The main contribution of the author in this research was focused on HS 0810+2554 VLA observations.

4.1 The need for radio observations of lensed quasars

Strong gravitational lens systems, in which background sources are multiply imaged by foreground galaxies, are important for two main reasons. First, the lensing effect magnifies the background source; although the surface brightness is conserved, the area increases and we can observe background sources with typically 5–10 times better signal-to-noise than without the lensing. Second, the lensing effect allows us to probe the mass distribution of the lensing galaxy, on scales from the overall mass profile down to the scales of individual stars. General reviews of strong lensing and its applications relevant to this work are given by Kochanek (2004a), Courbin et al. (2002), Zackrisson & Riehm (2010), Bartelmann (2010) and Jackson (2013).

Lens systems in which the background source is a quasar were the first class of systems to be discovered, mostly in radio surveys (Walsh et al. 1979; Hewitt et al. 1988; Browne et al. 2003) but later in optical surveys (e.g. Wisotzki et al. 1993; Inada et al. 2003b). Lens systems with optical, or "radio-quiet", quasars as the source now dominate the sample of strongly lensed quasars. The radio-selected sample is mostly composed of the 22 lenses from the Cosmic Lens All-Sky survey (CLASS; Myers et al. 2003; Browne et al. 2003) together with smaller samples from the MIT-Greenbank (MG) and southern surveys (e.g. Hewitt et al. 1992; Winn et al. 2002). This sample has not expanded significantly in the last 15 years, because of the difficulty – in the era before the Square Kilometre Array – of conducting more sensitive wide-field radio surveys at the necessary sub-arcsecond resolution for lens discovery.

In order to increase the size of the sample of quasar lenses observed at radio wavelengths, we can use the fact that all quasars are likely to have radio emission at some level. For example, White et al. (2007) performed a stacking analysis at the positions of radio-"quiet" quasars from the FIRST 20-cm radio survey (Becker et al. 1995) and found that quasars not detected at the 1-mJy level are likely, on average, to have radio flux densities which fall with decreasing optical brightness to $\sim 100\mu$Jy at $I = 20 - 21$. This is within reach of the new generation of telescopes such as the Karl G. Jansky Very Large Array (VLA) and the extended Multi-Element Remote Linked Interferometer (e-MERLIN). We began a programme (Wucknitz & Volino 2008, Jackson 2011) to investigate four-image quasar lens systems without current radio detections, and achieved a successful detection, at around the 20-30μJy level, of lensed images of the background quasar in the cluster lens system SDSS J1004+4112, as well as detections of lensed images at a brighter level in the lens system RXJ 1131−1231.

There are three main motivations for radio observations of the radio emission from

radio-"quiet"[1] quasar lens systems. The first is that the emission mechanisms of radio-quiet quasars are not well understood, and in particular it is not clear how far the mechanisms which power radio-loud quasars – accretion and the formation of a powerful jet close to a black hole – also apply to radio-quiet quasars. In sources of intermediate flux density, jets characteristic of ordinary active nuclei are seen (Blundell & Beasley 1998; Leipski et al. 2006) and the radio sources appear to be variable (Barvainis et al. 2005). Both of these observations suggest that the AGN paradigm applies to these objects. In fainter cases (<1 mJy at 1.4 GHz at redshifts of a few tenths) however, Condon et al. (2013) argue that star formation is the primary mechanism for the emission. This is inferred from an analysis showing that the radio luminosity function of QSOs turns up sharply below $L_{1.4\mathrm{GHz}} < 10^{24}$ W Hz^{-1} and suggesting that a second population emerges at these luminosities. It is also possible that a different emission mechanism is at work in the core of the sources. (Blundell & Kuncic 2007) suggest the presence of optically-thin bremsstrahlung emission (although see Steenbrugge et al. 2011 for evidence against this view) and Laor & Behar (2008) propose the possibility of emission from magnetically-heated coronae, rather than a classical AGN source. It is important to achieve high-resolution radio imaging of these sources in order to separate the possibilities. This is typically very difficult to achieve with current long-baseline interferometers in very faint objects. However, the use of lensing magnification provides a way to detect otherwise unobservable objects.

The second motivation is that radio and optical observations are subject to different propagation effects. The main such effect in the optical is microlensing due to stars in the lens galaxy, which produces measurable flux changes because the size of the optical source is very small. Repeated optical monitoring can reveal the flux density variations associated with the movement of the source with respect to the microlensing caustic patterns (Blackburne et al. 2011; Burud et al. 2002; Irwin et al. 1989; Muñoz et al. 2011; Poindexter et al. 2008; Wisotzki et al. 1993). At radio wavelengths, the source is larger, and therefore much less susceptible to microlensing; hence, comparison between the two wavebands can reveal the effects of microlensing directly. In the radio, the only significant propagation effect is scattering by ionized media (Koopmans et al. 2003)[2]. This seems to be particularly noticeable in a few cases, such as CLASS B0128+437 (Biggs et al. 2004; Phillips et al. 2000) but should in principle decrease strongly at higher radio frequencies. A corresponding problem at optical wavelengths is extinction by dust in the lensing galaxy, which can be used to learn about the properties of the dust if the intrinsic fluxes

[1] In the rest of this chapter, we drop the inverted commas, but it should be understood that radio-"quiet" quasars are not radio silent.

[2] In principle, the size of a compact, synchrotron self-absorbed radio source decreases as the square root of the brightness, but this is unlikely to result in microlensing until the source is fainter than 1μJy. Claims exist for radio microlensing (Koopmans & de Bruyn 2000) which could also be explained by other propagation effects. In principle, free-free absorption is also possible (Mittal et al. 2006) although the electron columns are likely to be too small in all but exceptional cases.

are known (e.g. Falco et al. 1999, Jackson et al. 2000, Muñoz et al. 2004, Elíasdóttir et al. 2006, Østman et al. 2008). Radio wavelengths therefore provide an important input to any programme which aims to disentangle the effects of substructure in the lens galaxy from those of microlensing and extinction.

The third motivation for radio observations of four-image gravitational lens systems is their potential to probe substructure in the lens galaxies. In principle, quasar lens systems are useful for probing small-scale structure within the lens potential, down to $10^6\,M_\odot$ and below (Mao & Schneider 1998), because the flux density of the lensed image can be perturbed by small-scale mass structures close to the corresponding ray path. Such sub-galactic scale structures are important predictions of Cold Dark Matter (CDM) models. Initially they were thought not to be present in required quantities in the Milky Way (Klypin et al. 1999; Moore et al. 1999). The situation is now less clear, as a population of faint Milky Way satellites have since been discovered (Belokurov et al. 2006; Zucker et al. 2006; Koposov et al. 2015). The Milky Way halo mass is a critical variable (Kafle et al. 2014; Wang et al. 2012) as the predicted halo population is sensitive to it. In lens systems, the flux density of the lensed images is particularly sensitive to small structures, because it depends on the second derivative of the lensing potential, as opposed to the image positions which depend on the first derivative. The usual evidence for a detection of substructure is therefore a set of image flux ratios which cannot be fit by smooth models. More particularly, four-image lenses in cusp configurations (where the source is close to the cusp of the astroid caustic) and fold configurations (resulting from the source being close to the caustic fold) give clear theoretical expectations for image flux ratios which must be obeyed by any smooth model. In cusp lenses, there are three close images and the middle image is expected to have the brightness of the sum of the outer two (Schneider & Weiss 1992); in fold lenses, the two close images are expected to have the same flux (Keeton et al. 2003; Congdon et al. 2008). Because of optical microlensing, radio lens systems have traditionally been used for this work (Mao & Schneider 1998, Fassnacht et al. 1999a, Metcalf & Zhao 2002, Metcalf 2005, Kratzer et al. 2011). The statistics of such objects were analysed by Dalal & Kochanek (2002) who found a fraction of between 0.6% and 7% of mass in $10^6 - 10^9\,M_\odot$ substructures at the radius probed by the lensing. More recent theoretical work has used more realistic treatment of lens galaxies via the use of numerical simulations (Bradač et al. 2004, Amara et al. 2006, Macciò et al. 2006, Xu et al. 2009). The conclusions are generally that there is, if anything, an excess of substructure over what is predicted to exist in CDM (though see Metcalf & Amara 2012, Xu et al. 2015). At the same time, analyses of individual lens systems have yielded constraints on substructures at the $\sim 10^6\,M_\odot$ level (e.g. Fadely & Keeton 2012). The major problem in using quasar lenses to constrain substructure has been the lack of large enough samples of radio-loud four-image lenses; the seven studied by Dalal & Kochanek (2002) have formed the sample for most subsequent investigations. Possible solutions to this problem include the use of mid-infrared fluxes (Chiba et al. 2005; Fadely & Keeton

2011; Vives-Arias et al. 2016) assuming that the mid-IR source is large enough not to be subject to microlensing (but see Sluse et al. 2013). An alternative approach is to use the narrow line region of quasars (Moustakas & Metcalf 2003, Sugai et al. 2007, Nierenberg et al. 2014) which should also be large enough to be unaffected by microlensing, or submillimetre observations in the case of new lenses from Herschel and the SPT (Hezaveh et al. 2013). A further alternative is to perform lens reconstruction of systems with extended sources (Warren & Dye 2003, Dye & Warren 2005, Koopmans 2005, Vegetti & Koopmans 2009, Vegetti et al. 2012). Cases of substructure detections have already been reported from these works, although the sensitivity is mainly towards the higher-mass end of the substructure mass function; quasar lenses are thus likely to be usefully complementary to this method.

This work presents a continuation of a programme to detect and image faint radio sources in gravitational lens systems. Its aim is to increase the number of four-image lenses with detected radio fluxes, both to increase the sample sizes of quasar lens systems suitable for the investigation of sub-galactic scale substructures in the lens, and to begin the study of the very faint radio sources which are imaged by the foreground lens galaxies. Where necessary we use a standard flat cosmology with $\Omega_m = 0.27$ and $H_0 = 68$ km s^{-1} Mpc^{-1}.

4.2 Radio interferometry

The maximum angular resolution that can be achieved by a telescope is given by λ/D (in radians), where D is the telescope's diameter and λ is the wavelength of the observations. This is due to diffraction of the light by the limited aperture of the instrument, which acts as a two-dimensional version of Young's double slit experiment. As a wavefront of light enters the telescope, it interferes with itself and creates a diffraction pattern that can be broader than the observed source, making it hard to separate two different objects situated at a small angular distance. This becomes a problem in radio astronomy, where wavelengths are so long that they would require very large dishes to achieve the resolutions that are commonplace in optical or even infrared observations, but it can be circumvented by taking advantage of the same interference phenomenon that causes the problem in the first place.

4.2.1 Basic principles

The interference patterns created by Young's slits are caused by the length difference in the path that light travels to reach the same point on the screen through one slit and the other, which creates a time delay between their arrivals. This delay also happens if instead of two slits and a screen, we have two separate detectors and the source is at a

different distance from each of them. If we combine (make interfere) the signals from each of the detectors when measuring a plane incident wave from a coherent and monochromatic source, at different relative positions we would obtain a constructive interference, a destructive interference, or anything in between. This situation is analogous to the double slit experiment, and the same equations apply. If we put all the elements in the same plane, for a source at a certain angle θ from the baseline between both detectors, separated a distance d, the delay is $(d\cos\theta)/c$, where c is the speed of light. This corresponds to the delay between the rays of light that come from the slits at an angle θ when the distance between the slits is d, and will combine in the same position on the screen. In both cases, the interference pattern will have fringes at an angular distance λ/d from each other.

If the source is extended, each point of its surface can be considered a point source, but they will no longer be coherent with each other. Since an angular displacement of the source produces an angular displacement in the pattern, the resulting interference pattern will be the sum of the intensities (not amplitudes) of patterns with the same structure that are slightly displaced from each other, and the fringes will be less visible because there is no longer completely destructive interference and the contrast will decrease. The fringe visibility (defined as the difference between maximum and minimum intensity, normalized by the sum of maximum and minimum intensity) will drop to zero as the source size approaches λ/d, and will become 1 when the angular size of the source is $\ll \lambda/d$. A way to increase the visibility for a large source is to decrease the distance d, because then a displacement of the source will produce a much lower displacement of the fringes. And at the same time, in order to get fine details in small sources, one needs to increase the baseline length between the receptors. This is how a radio interferometer of several antennas can in principle achieve resolutions as high as a telescope with a diameter d, but with much lower technical difficulties as the ones building a single antenna of such a large size would involve.

4.2.2 How radio interferometry works

The relation between the intensity distribution of the source as a function of the angle on the sky, $I(\theta)$, and the visibility of the interference fringes as a function of the slit separation or the baseline length, $V(d)$, is one which maps a large Gaussian into a small Gaussian and vice versa, like a Fourier transform. In fact, the interference pattern will be the Fourier transform of the source intensity distribution, if we compensate for the different distances from the receptors to the source so that we are only left with the time delays associated with the different angular positions at the source plane. This can be done by inserting electronic delays before combining the signals of the different receptors, so that their phase is shifted accordingly. By doing this, the interferometer effectively becomes a projection of the locations of the different receptors onto a plane perpendicular to the vector that points towards the source.

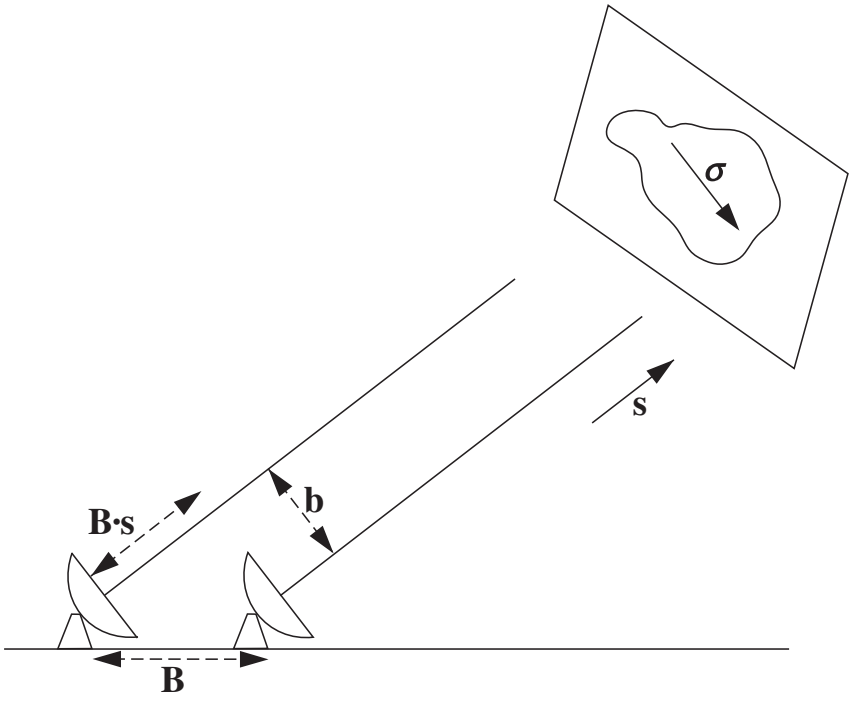

Figure 4.1 Configuration of a radio interferometer with two antennas. **B** is the baseline vector between the antennas; **s** is the vector of the line of sight towards the source, perpendicular to the plane of the sky; **b** is the vector of the projected baseline as seen from the source, in a plane parallel to the plane of the sky; and $\boldsymbol{\sigma}$ is a vector in the plane of the source.

If we define $\boldsymbol{\sigma}$ as a vector in the plane of the source, we can decompose it as $\boldsymbol{\sigma} = \sigma_x \mathbf{i} + \sigma_y \mathbf{j}$, where $\mathbf{i}$ and $\mathbf{j}$ are unit vectors in the east-west and north-south directions, respectively. Likewise, we can define the projected baseline vector as $\mathbf{b}$, and decompose it as $\mathbf{b} = u\mathbf{i} + v\mathbf{j}$, so that $\mathbf{b} \cdot \boldsymbol{\sigma} = ux + vy$. The response of the projected interferometer then becomes

$$R(u,v) = \int\int I(x,y) e^{2\pi i(ux+vy)} dxdy, \tag{4.1}$$

which is a 2D Fourier transform. Note that u and v are defined in units of wavelength.

Of the whole Fourier transform of the source that would form in the $u-v$ plane, only the position at the end of each projected baseline is sampled (for each possible baseline, a receptor is chosen as reference and located at the center of the $u-v$ plane, and the

other receptor is at the end of their projected baseline vector **b**). In order to sample the largest area of the $u-v$ plane possible, other than to have a huge extension of the Earth completely covered with antennas, one can have a limited number of receptors (but as large as possible, since the number of baselines goes as $n(n-1)/2$, for n telescopes), but keep observing the source for many hours. As the Earth rotates, the projected positions of the receptors will describe ellipses in the $u-v$ plane, increasing the coverage. If the emission from the source does not vary a lot in different radio wavelengths, another way is to increase the bandwidth of the observations, provided that it remains divided in many separate channels (otherwise the visibility of the fringes away from the center of the $u-v$ plane will decrease and the field of view will be diminished). Since u and v are in units of wavelength, the projected baselines will have different lengths in each channel, thus widening the swaths that are being covered. Also, the receptors must be located in such a way as to ensure coverage at both short and large projected baselines, since the global structure will be lost if only long baselines are chosen, and the same will happen with the finer details with only short baselines.

In order to reconstruct an image $I(x,y)$ of the source from our observations, we would ideally transform the full u,v response function $I(u,v)$:

$$I(x,y) = \int\int I(u,v)e^{2\pi i(ux+vy)}dudv, \tag{4.2}$$

but a sampling function $S(u,v)$ intervenes, which is 1 in the sampled positions and zero in the unsampled ones. So instead we have the "dirty image"

$$I_D(x,y) = \int\int I(u,v)S(u,v)e^{2\pi i(ux+vy)}dudv, \tag{4.3}$$

which thanks to the convolution theorem we can write as

$$I_D(x,y) = I(x,y) * B(x,y), \tag{4.4}$$

where

$$B(x,y) = \int\int S(u,v)e^{2\pi i(ux+vy)}dudv, \tag{4.5}$$

is the "dirty beam", the Fourier transform of the sampling function. Since the sampling function is accurately known, we can recover the image $I(x,y)$ by performing a classical deconvolution, provided that we supply some additional information.

One of the most commonly used procedures to do this deconvolution is the CLEAN algorithm (Högbom 1974), in which the extra information consists of assuming that the source brightness distribution consists of a small number of point sources. Here, the dirty beam is subtracted from the brightest point of the dirty image while remembering the

position and amount of brightness subtracted, and then the process is repeated iteratively with the residuals until the resulting map consists only of noise. Then, the subtracted fluxes are convolved with a restoring beam to generate the "CLEAN map", where the side lobes of the dirty beam have been removed.

In order to know when to stop iterating to avoid interpreting features in the noise as structure on the source, the theoretical noise level of the interferometer (or sensitivity, S) can be calculated as

$$S = \frac{\sqrt{2} k_B T_{\text{sys}}}{A\eta\sqrt{n_b \Delta_\nu \, t_{\text{int}}}}, \tag{4.6}$$

where k_B is the Boltzmann constant, T_{sys} is the system temperature, A is the area of each antenna, η is the aperture efficiency, n_b is the number of baselines, Δ_ν is the observing bandwith, and t_{int} is the integration time.

4.2.3 Atmosphere, interference and bad data

When radio waves reach Earth, their phase can fluctuate due to perturbations by the ionosphere (at low frequencies) or water vapor (at higher frequencies), which can also affect even the observed amplitudes. With a bright source (so the signal-to-noise ratio is low), if the errors are separable by telescope, the phase fluctuations can be cancelled out with a minimum of three telescopes and the amplitude fluctuations with four, but in general the data will need calibration. If the source contains a point source visible in all baselines at $> 3\sigma$ in one coherence time, a self-calibration can be performed (Cornwell & Wilkinson 1981) at the cost of losing information about the absolute position of the source. A more direct way, however, is to periodically observe a calibrator source of known structure, that can then be Fourier transformed and removed from the response function, thus allowing to interpolate and remove the residual atmospheric phase structure. The flux can also be calibrated by observing a known source with constant flux, as one would do when performing single-telescope observations.

Radio interference from artificial sources can also be a problem. Since the intensity of the interference can be much higher than the observed astronomical object, it can create spikes in the $u - v$ plane that get Fourier transformed into stripes on the reconstructed image, or can make it hard for the calibration procedures to work properly. Finally, another cause of noise and bad data can be the interferometer itself, where some antennas, correlators or other electronic components could not be functioning properly or optimally. The solution for these kinds of interference is to flag or remove all bad or dubious data from the observation altogether, before proceeding to the calibration and analysis.

4.3 Sample and observations

4.3.1 Sample selection

Our target sample includes all known gravitational lens systems with four lensed images, no detected radio emission above the ∼1 mJy level reached in large-scale sky surveys such as the FIRST and NVSS 1.4-GHz surveys (Becker et al. 1995; Condon et al. 1998), and with declination $> -20°$ for accessibility to the VLA and e-MERLIN radio arrays. There are 13 of these in current compilations such as the CASTLES (Kochanek et al. 1998) and Masterlens (Moustakas et al. 2012) lists, which represents a potential factor of 3 improvement in statistics if radio flux densities can be measured for all of them. One of these objects, SDSS J1004+4112, was already detected by Jackson (2011) using the VLA in the lower resolution C-configuration. This is a wide-separation object (Inada et al. 2003b) resulting from the lensing action of a cluster, whose mass distribution is correspondingly more difficult to model. Most such objects, however, are lensed by individual galaxies; we have in this preliminary phase used the VLA (resolution ∼0.″3 at 5 GHz) to investigate the wider-separation objects within this sample. A further object, RXJ 1131-1231, was previously detected by Wucknitz & Volino (2008) in archival VLA data, and subsequently with the VLA and MERLIN (although not with VLBI). Table 4.1 shows a summary of the lens systems observed (including, for completeness, SDSS J1004+4112) together with the source and lens redshifts and other observational information.

Object	$z_{\rm lens}$	$z_{\rm source}$	Separation (arcsec)	References	VLA Obs. date (2012)	Freq. (GHz)	Exp. time (h)	noise (μJy/b)
HE 0435−1223	0.46	1.69	2.5	W02,M05,O06	Oct 26, Nov 9	5	6	3
HS 0810+2554	?	1.50	0.9	R02	Oct 22, Nov 8,24	8.4	7.5	3
RX J0911+0551	0.77	2.80	3.2	B97,B98,K00	Oct 31. Nov 6,24	5	7.5	3
SDSS J0924+0219	0.39	1.52	1.8	I03A,E06,O06	Nov 5	5	3	3
SDSS J1004+4112	0.68	1.73	14.6	I03B	See Jackson 2011	5	6	3

Table 4.1 Basic information for the systems studied, including the redshifts of lens and source (where known), maximum separation of the lensed images, observation time and frequency, and achieved noise level in the maps. References are given to the discovery papers for each lens, and to the sources for the measurements of the redshifts. In each case the on-source integration time is approximately 75% of the total exposure time. Key to references: W02 = Wisotzki et al. 2002, M05 = Morgan et al. 2005, R02 = Reimers et al. 2002, B97 = Bade et al. 1997, B98 = Burud et al. 1998, K00 = Kneib et al. 2000, I03A = Inada et al. 2003a, I03B = Inada et al. 2003b, E06 = Eigenbrod et al. 2006, O06 = Ofek et al. 2006.

Object	Phase calibrator	Date	Exposure	Frequency
HS 0810+2554	JVAS 0813+2435	31/03/2014	8h	1287-1799MHz
RXJ0911+0551	SDSS J0901+0448	26/04/2014	8h	1287-1799MHz

Table 4.2 Details of the e-MERLIN observations of two of the sources.

4.3.2 Observations and data reduction

4.3.2.1 VLA observations

Objects were observed with a total bandwidth of 2 GHz in 16 IFs of 128 MHz over the frequency range 4488-6512 MHz (C-band). The exception was HS 0810+2554 which was observed at X-band, with a similar spectral arrangement over the frequency range 7988-10036 MHz, in order to achieve the resolution needed for the smaller spatial scale of this source. Integration times were generally a few hours (Table 4.1) and observations were taken at various times during the autumn of 2012. Although the individual 3 or 1.5-hour observations were taken at different times, we do not detect variability in any case between individual epochs. All new observations were taken in A-configuration, which has a maximum baseline of 36 km and a theoretical resolution of $0\farcs35$ at 5 GHz and $0\farcs22$ at 8.4 GHz. Data were taken in spectral-line mode, with 2-MHz channels, although this was reduced in subsequent processing as only a small area of sky was required.

Nearby phase calibrators were observed at regular intervals, with a pattern of 1 minute on the calibrator and 5 minutes on source, in order to calibrate the instrumental and atmospheric phases. Sources of known flux density, either 3C138 or 3C286, were observed in order to fix the flux density to the Baars et al. (1977) scale.

Data analysis was performed using the NRAO AIPS package. The data were fringe fitted to remove instrumental delays using the phase calibrator observations, and a phase and amplitude solution was performed using the phase calibrator and a point source model. Maps were also made of the phase calibrator and used where necessary to iterate the phase and amplitude calibration, and the flux density solution was transferred from the flux calibrators. The resulting calibration was then applied to the target sources, which were imaged using natural weighting in order to achieve the best possible signal-to-noise. In general we obtain image noise levels close to the theoretical value, usually about 3μJy/beam for 6 hours of on-source time.

In the particular case of HS 0810+2554, the object was observed, together with JVAS 0802+2509 as a phase calibrator and 3C138 as the flux calibrator, in October 22nd and November 8th and 24th of 2012, for about 3 hours each day. Since one of the goals was to measure the flux ratios of the lensed images in radio wavelengths, special care

was put into flagging and removing as much interference as possible by visual inspection instead of just clipping the data to some value to remove unwanted peaks. This included removing the data from all baselines and times in the frequency range 9346-9368 MHz due to the presence of an intermittent interference peak around 9.36 GHz that would reach up to 5 mJy in some channels, probably coming from airborne weather radars. Also, the appearance of some stripes in the final image, a completely undesired feature when measuring flux differences between different positions, was traced to bad data coming from antennas 8, 15, 20 and 28 (N16, W72, N72 and N40, respectively), which had to be completely removed from the analysis. The remaining 23 antennas provided a lower number of baselines and this resulted in a small loss of resolution, but was compensated by the low levels of noise achieved in the final image.

4.3.2.2 e-MERLIN observations

Two of the objects (HS 0810+2554 and RX J0911+0551) were also observed with the e-MERLIN array (Table 2). The observations were carried out at L-band, with a bandwidth covering the wavelength range 1287-1799 MHz. In addition to the target sources, observations of nearby phase calibrators were carried out, with a cycle of 7 minutes on the target and 3 on the phase calibrator. Additional observations of 3C286 were carried out in order to set the flux scale, and of the bright point source OQ208 in order to calibrate the bandpass. Data reduction followed standard procedures (Argo 2014) including fringe fitting to all calibrator sources to determine delays, phase and amplitude calibration using the nearby phase calibrator, and determination of the flux scale and bandpass calibration, with allowance for the spectral index of the calibrator. The telescope weights were modified using standard values for L-band provided by the observatory, and final maps were made in the AIPS software package distributed by NRAO. Mapping in the case of HS 0810+2554 was complicated by the presence of a 200-mJy confusing source $6'$ from the target; this source was mapped simultaneously with the target, and was also used to refine the phase calibration of these observations. Noise levels achieved in these observations were about 15-30μJy, depending on the details of the mapping strategy.

4.4 Results and models

All four objects were detected in these observations, of which all but SDSS J0924+0219 have individually measured flux densities for each lensed image. We discuss the results for each object separately, before making more general remarks about the measurements. The radio flux densities are given in Table 4.3.

The approach to modelling the observations is the same in each case. First, we make a preliminary assessment of whether the radio map is consistent with lensing of a point

Object	Type	Cpt.	Flux density (radio,μJy)
HE 0435−1223	Cross	A	36.0 ± 2.1
		B	26.4 ± 2.1
		C	34.3 ± 2.1
		D	16.1 ± 2.1
HS 0810+2554	Fold	A	85.1 ± 3.7
		B	83.7 ± 3.7
		C	60.0 ± 3.7
		D	49.1 ± 3.7
RX J0911+0551	Cusp	A	26.9 ± 2.2
		B	53.2 ± 2.2
		C	19.7 ± 2.2
		D	9.4 ± 3.0
		G	18.3 ± 2.2

Table 4.3 Radio flux measurements for the sample of four-image lens systems observed with the VLA/e-MERLIN, in which fluxes can be measured. For HS 0810+2554 the flux densities are from the VLA map at 8.4 GHz; the corresponding flux densities in the e-MERLIN image are (161,173,129,216) for A,B,C and D respectively, with errors of approximately 30μJy in each case.

source into point images. We do this by modelling the structure, in each case, with four point-spread functions (PSFs; Table 4.3), whose extent is known accurately from the radio CLEAN procedure. In this model, we fix the separation between the four individual components using measurements from archive HST images as reported by the CASTLES astrometry (which are accurate to a few milliarcseconds), but the overall registration of the image has been allowed to vary. There are thus six free parameters in the model, two for the registration, and four from the flux densities of the individual points. Second, we make a lens model using constraints from the image-plane radio map; for this, we assume a singular isothermal mass distribution (except in the case of HE 0435−1223) for the lenses together with a contribution from external shear. The source is assumed to be of Gaussian profile, and the resulting image plane is compared to the data, optimising the lens galaxy parameters together with the source position, flux density, size and ellipticity. We note that modern wide-bandwidth interferometers at centimetre wavelengths, such as the VLA and e-MERLIN, come close to filling the $u - v$ plane. Because of this virtually filled aperture, there is no need to fit the data directly in the $u - v$ plane. This contrasts with the situation in early Atacama Large Millimetre Array (ALMA) datasets used to map sub-millimetre lenses (e.g. Hezaveh et al. 2013).

4.4.1 HS 0810+2554

HS 0810+2554 was discovered by Reimers et al. (2002) and consists of four images with the two southwestern, bright images in a merging pair configuration. In HST imaging (Reimers et al. 2002) the lensing galaxy is detected, with an unknown redshift (it is estimated as 0.89 by Mosquera & Kochanek 2011 from the separation and the redshift distribution of existing lenses). These images also show a 0.7-magnitude difference in brightness between the components of the merging pair, contrary to the expectations of simple models, but this is likely to be due to microlensing in the lens galaxy. The source is a narrow absorption line quasar, with relativistic outflows detected using X-ray absorption spectra (Chartas et al. 2014). These high velocity outflows may be magnetically driven.

Our radio maps from the VLA and e-MERLIN are shown in Fig. 4.2. The components in the VLA image appear extended, and a faint arc is visible around the bright merging pair. This extension can be quantified by attempting to model the lensed structure only with point sources, with separations fixed to that of archival HST data. The best fit shows significant residuals, in particular around the bright merging components, but also at a lower level around the line connecting images B and C (Fig. 4.3). It is obvious from visual inspection that the shape of the A-B complex in the data is significantly different from that of a two-Gaussian realisation. We therefore conclude that the source is likely to be extended and model it as such.

In order to model the extended source, we have assumed a simple lens model (singular isothermal ellipsoid plus external shear) and treated the source as an ellipse with a flux density, axial ratio, position and orientation which are free to vary. For each iteration of the model, the source is projected through the lens model, and the result convolved with the PSF of the radio map. Minimisation of the χ^2 between the model image and data is carried out, where the χ^2 value is determined from a comparison of the model with the image in all regions where either model or image contains flux above 2σ. Correlations between pixels are neglected. The position of the galaxy is fixed by the use of the Hubble Space Telescope (HST) image during this process. In practice, the quality of the fit does not depend significantly on this quantity, provided that the source is allowed to move to keep the same distance between it and the galaxy. An acceptable fit of χ^2=1.6 is obtained with such a procedure; the parameters of this fit are given in Table 4.4 and shown in Fig. 4.4 and 4.5. The two close images, A and B, are of approximately the same flux density, as expected in the absence of millilensing-scale substructure and in contrast to the measurements in the optical and near infrared. The model implies a magnification of about 25 for the brightest image, yielding an intrinsic flux density of 3.5 μJy for the source. The implied magnification is a factor of 2 less than that of the model by Assef et al. (2011), but HS 0810+2554 is in the high-magnification regime where the source is

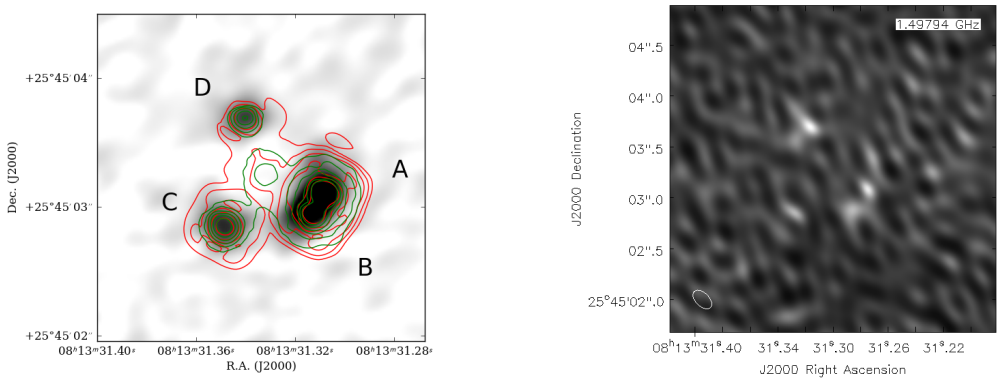

Figure 4.2 Left: VLA greyscale radio map of HS 0810+2554 at 8.4 GHz. The beam is of full width at half maximum (FWHM) 300×240 mas in position angle −65.17°. Archival HST Near-Infrared Camera and Multi-Object Spectrometer (NICMOS, red) and Advanced Camera for Surveys (ACS, green) contours have been performed using image C. The conventional nomenclature of the images (Reimers et al. 2002) is that the merging complex in the southwest consists of images A and B, with A being further north. Right: e-MERLIN image of HS 0810+2554 at approximately the same resolution, but a frequency of 1.6 GHz. The noise level is approximately 29μJy/beam; all the images are detected at $> 5\sigma$ significance.

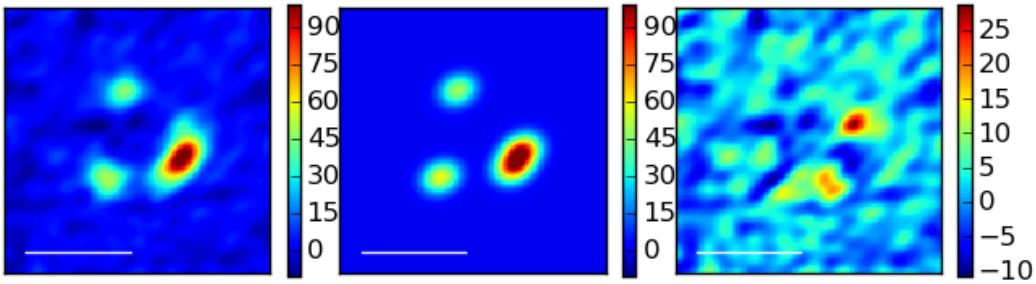

Figure 4.3 Model of HS0810+2554, using a point-source model fit (see text). The data, model, and residual are plotted; unlike the case with the extended source model, there appear to be significant features in the residual. Note that in this case, and unlike the case of the extended source model, the overall shape of the A-B complex is not well reproduced. The bar in each panel represents 1″, and the colour scales in the sidebars are in units of μJy/beam.

Quantity	HS0810+2554	HE0435−1223	RXJ0911+0551
Source position/mas	0.1 E, 13.0 S	-68 E, 18 S	468 E, 28 S
Source FWHM along major axis/mas	12±1	80^{+5}_{-5}	131^{+15}_{-11}
Source flux/μJy	3.6±0.2	$2.9^{+0.3}_{-0.4}$	$3.7^{+0.3}_{-0.2}$
Source b/a	$0.66^{+0.06}_{-0.09}$	≡1.0	≡1.0
Source position angle	(47±5)°	–	–
Galaxy critical radius/mas	473±10	1138^{+19}_{-6}	1047^{+11}_{-38}
Density slope (2 = isothermal)	≡2.0	$2.00^{0.08}_{-0.06}$	≡2.0
Galaxy ellipticity	0.0003±0.0003	0.26±0.02	$0.15^{+0.03}_{-0.09}$
External shear	0.023±0.006, (29±4)°	$0.039^{+0.004}_{-0.011}$, (−30±7)°	$0.373^{+0.033}_{-0.011}$, (9±2)°

Table 4.4 Model fitting results for the three lens systems for which lens modelling is possible (all observed lenses except SDSS 0924+0219). The source position is quoted relative to the galaxy position, and all distances are given in units of milliarcseconds. For HE0435−1223 and RXJ0911+0551, the galaxy critical radius corresponds to the Einstein radius measured along the major axis.

contained within a very small astroid caustic, and minor movements in the source position produce major changes in the implied magnification.

In order to derive uncertainties, the parameters have been run through a Markov Chain Monte Carlo (MCMC) process using the publicly available EMCEE routine (Foreman-Mackey et al. 2013). We have assumed a number of hard priors, namely limits of 0″–1″ for the Einstein radius of the galaxy, limits of $0 < \gamma < 0.5$ for the external shear contribution, a requirement that the source flux and source width are positive, and that ellipticities of the source and galaxy must be <1. Finally, we have imposed a Gaussian prior on the position of the lens galaxy, based on the measured position in the HST image and with a width of 10 mas. The results (Table 4.4) make it clear that the source is extended by approximately 10 mas in the source plane, corresponding to about 70 pc in physical scale, at a position angle of approximately 50°. As usual with strong lens systems, we obtain a relatively accurate measurement of the Einstein radius of the lens galaxy, which is modelled as being almost circular. This is consistent with its appearance on archival HST images.

Although the existing e-MERLIN images do not have very high signal-to-noise, they do allow us to measure an approximate overall spectral index, because the resolution of the e-MERLIN 1.6-GHz image is very similar to that of the VLA at 8.4 GHz. This spectral index is moderately steep, at -0.55 ± 0.1.

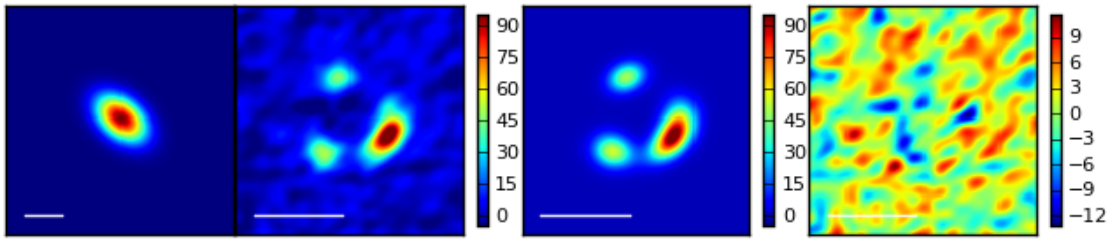

Figure 4.4 Models of HS0810+2554, using a singular isothermal sphere model plus external shear (see text) together with a best-fit extended source. The reconstructed source, data, model, and residual are plotted. The white bar represents 10 mas in the panel of the reconstructed source, and 1″ in all other cases. In these and subsequent figures, the data and model are plotted on the same colour scale, and the residuals are scaled to the minimum/maximum of the residual map. The colour-bars represent flux densities in μJy/beam; the colour scale of the source is arbitrary, but its parameters are given in Table 4.4. A good fit is obtained with an unlensed source size of between 10-15 mas.

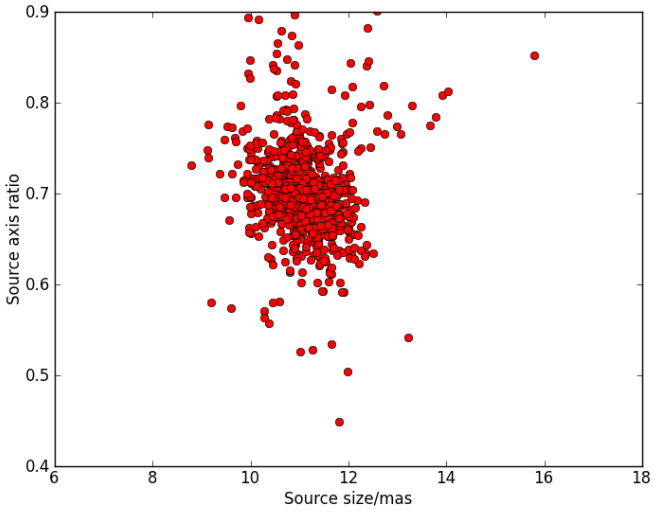

Figure 4.5 MCMC realisations of the model of HS 0810+2554, plotted as probability density of source size against source axis ratio. The preferred source size corresponds to a linear scale of approximately 100 pc, a unique resolution for such a faint radio source.

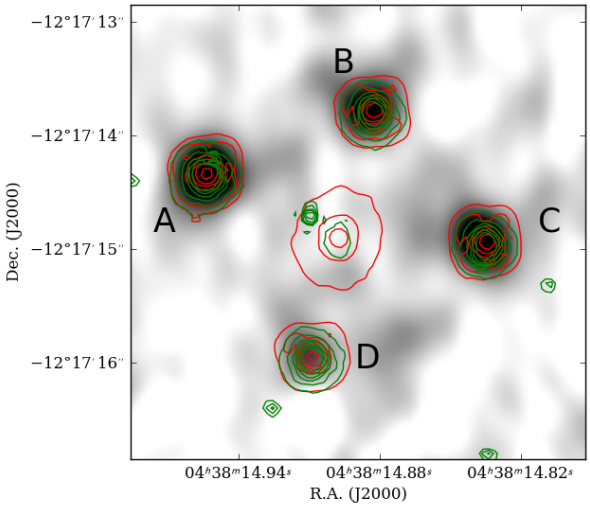

Figure 4.6 VLA radio map of HE 0435−1223. The greyscale runs from 0 to 20μJy/beam. The beam is circular, and of FWHM 0.″45. Archival NICMOS (red contours) and ACS (green contours) images are overlaid. Registration of these images has been performed using image A. The conventional nomenclature of the images is that A is the easternmost and B,C,D proceed clockwise around the lens galaxy.

4.4.2 HE 0435−1223

HE 0435−1223 was discovered by Wisotzki et al. (2002) and identified as a four-image system with an early-type lens galaxy. The lens redshift was obtained by Morgan et al. (2005), who also found that the lens is part of a group of galaxies. Microlensing was detected in a subsequent monitoring campaign (Kochanek et al. 2006) which probably affects the A component most strongly (Courbin et al. 2011; Ricci et al. 2011), and it has also been shown that the broad-line region in this object is subject to microlensing (Sluse et al. 2012a; Braibant et al. 2014). Modelling of the lens is able to reproduce well the positions of the lensed images, using only a single-galaxy deflector model (Sluse et al. 2012b). Fadely & Keeton (2012) examined and modelled this object extensively in a search for evidence of substructure in the lensing galaxy, using their L'-band mid-infrared fluxes of the four components as inputs for the modelling. Since much of the quasar mid-infrared emission comes from a circumnuclear torus, this may be immune to microlensing as the torus is likely to be relatively large.

Our radio map (Fig. 4.6) shows all four lensed images, at positions negligibly different from those of the optical and infrared HST images (obtained from the HST archive). Once again, therefore, we have modelled the radio map assuming that it consists of four

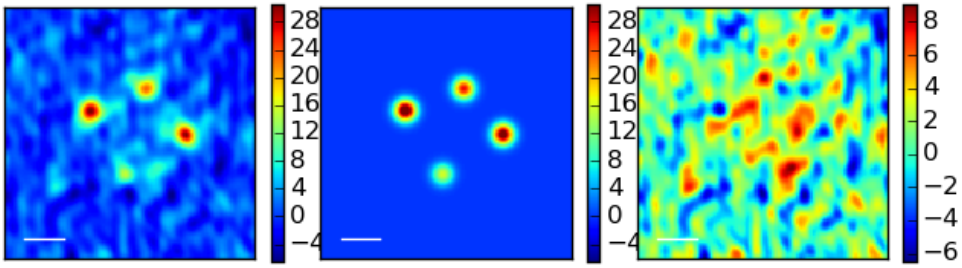

Figure 4.7 Models of HE 0435−1223, using a point-source model fit (see text). The data, model, and residual are plotted; unlike the case with the extended source model, there appear to be significant features in the residual. The bar in each panel represents 1″. The numbers on each colourbar are in units of μJy/beam.

point sources, whose separation is determined by the HST optical image. The results of this procedure are shown in Fig. 4.7. There are hints of emission outside the four point sources, particularly close to image C, but these are at the 2-σ level and would need deeper observations to confirm or rule out. The image fluxes are given in Table 4.3, and, with a ratio of 1.05:0.77:1.00:0.47 between A:B:C:D images, differ significantly from the L' ratios 1.71:0.99:1.00:0.81 of Fadely & Keeton (2012). In particular, the A/C and C/D ratios differ by about 3σ between the two sets of observations, the difference in C/D ratio being particularly obvious from Fig. 4.6.

This difference in flux density ratios, and its explanation, is a difficult and intriguing problem. Fadely & Keeton (2012) undertook extensive modelling of this system using a softened power-law for the primary galaxy, together with a singular isothermal model for the nearby galaxy, G22, which is about four arcseconds to the SW. They also included a shear component, to account for the more general shear field of the cluster. Smooth models with a slightly shallower slope than isothermal failed to reproduce the infrared fluxes, and further analysis showed that the Bayesian evidence favoured a contribution due to substructure around A. The observation driving this conclusion was the A/C ratio, which smooth models preferred to be between 1.4 and 1.5, as opposed to the higher value in the infrared data. Our radio data, on the other hand, prefer a much lower value for the A/C ratio, together with a much fainter D component. Since the radio is almost certainly not affected by microlensing, this is a puzzling result.

In our next step of modelling the data, we assume the source is point-like and include the observed time delays (Courbin et al. 2011) as additional constraints. Modelling the lens as an ellipsoidal power-law with external shear and a SIS at the position of G22 ($z = 0.78$, Chen et al. 2014), realistic, smooth models are unable to reproduce the data. The best model, further constrained using strong Gaussian priors on the positions

(1σ=10 mas) of the galaxies, agrees with those observed time delays within the errors but not with the image fluxes, yielding a χ^2 of 14.9 for four degrees of freedom.[1] In particular, the predicted B/C and D/C ratios are in disagreement at the 1.3σ and 3σ levels, respectively. For the main lensing galaxy, the best model prefers an ellipticity of $e \approx 0.28$ and power-law slope of $\gamma' \approx 2.24$. We note that the steep density slope may be driven by the model trying to fit the flux ratios.

The flux ratio anomaly seen with the smooth model could be explained by invoking substructure. To explore this possibility, we follow the approach of Fadely & Keeton (2012). Briefly, substructure clumps are modelled using a pseudo-Jaffe profile, and a wide range of masses are considered, whose masses enclosed within the Einstein radii range from $10^4 - 10^9$ $M_\odot$. Modelling the smooth lens component as before, we find that clumps placed near images A, B, or C do not improve the fit. However, clumps over a large range of masses placed near image D can bring the model into good agreement with the data, yielding a χ^2 of 1.5 for one degree of freedom.[1] Like Fadely & Keeton (2012), we find that more massive clumps can be placed farther away from the image, while less massive clumps must be placed nearer. Furthermore, the clumps cannot lie within approximately two Einstein radii of image D. Otherwise, image splitting can magnify the image, making matters worse. As for the main lensing galaxy, ellipticities of $e \approx 0.33$ and steeper-than-isothermal power-law slopes of $\gamma' \approx 2.33$ are preferred.

Alternatively, if we do not invoke substructure, another possible solution arises if the radio emission region is extended and differentially magnified (see e.g. Serjeant 2012). Because the size of the caustic is less than approximately 400 mas, a wide range of source sizes below this scale can reproduce the data. We again use a two-deflector model, including the main lensing galaxy as an ellipsoidal power-law with a contribution from external shear and G22 as a SIS. The source is modelled as a spherical Gaussian. Owing to the large number of image pixels (3150 pixels) used to constrain the model, including time delay constraints for a point source at the position of the source does not significantly affect our results, and so we include them for consistency with the previous analyses. Additionally, to try to account for the noise correlation in the data and to be conservative in our parameter inference, we follow the suggestion of Riechers et al. (2008) and increase the input noise level by a factor dependent on the noise correlation length scale (a factor of three, in this case). Our best model achieves a χ^2 of 854 for 3141 degrees of freedom.[1] After marginalizing over all lens model parameters, our MCMC analysis finds that an isothermal slope is preferred for the main lensing galaxy ($\gamma' = 2.00^{+0.08}_{-0.06}$) and that the source is of FWHM 80^{+5}_{-5} mas. This optimal source size leads to an image-plane model

[1]Because of the intrinsic nonlinearity of the lens modelling and the strong Gaussian priors placed on the galaxy positions, calculating the the number of degrees of freedom is nontrivial. Thus, we have chosen to count each galaxy position parameter as half a degree of freedom, and so the "true" number of degrees of freedom may be ± 2 of the number we quote here.

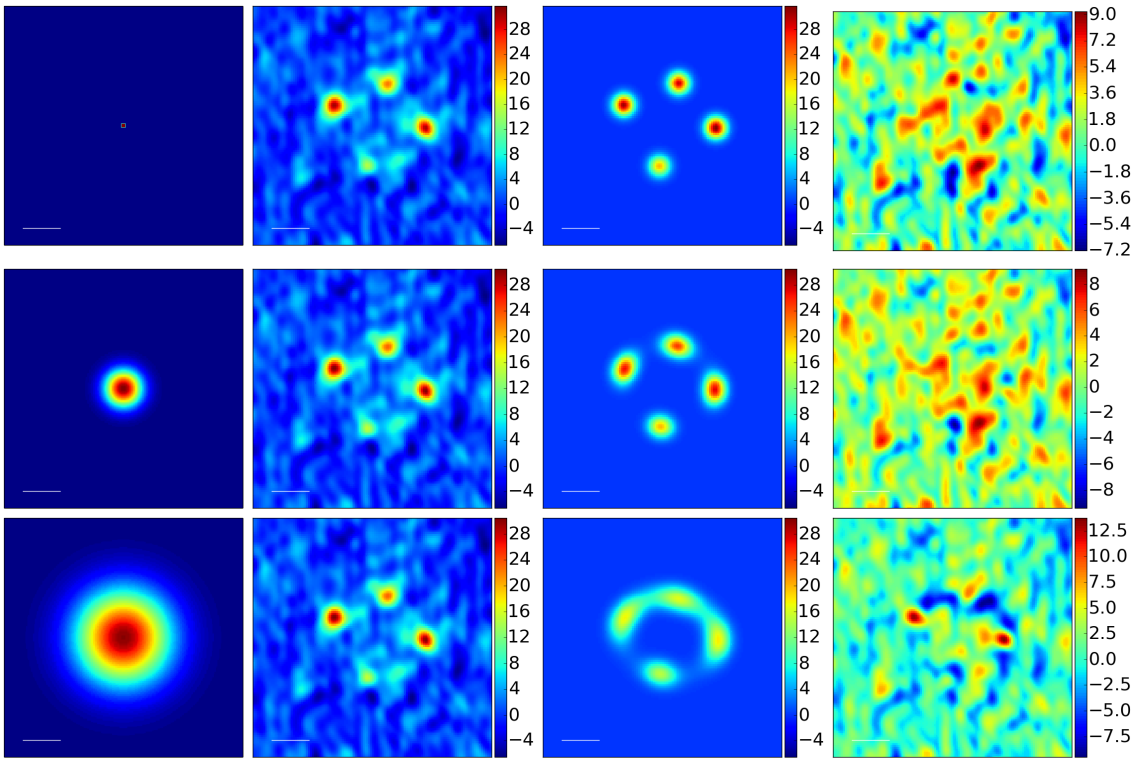

Figure 4.8 Models of HE 0435−1223/ From left to right: source model; data; image-plane model; residual. The white bars represent 100 mas in the source plane (left panel) and 1 arcsecond in all other panels. Three different fits are shown: (top) small 3 mas source, (middle) optimal 80 mas source, (bottom) large 200 mas source. Although the 80 mas source is preferred by our MCMC analysis, smaller sources provide an equally good visual fit, while larger sources lead to significant model residuals. The colour-bars represent flux densities in μJy/beam; the colour scale of the source is arbitrary, but its parameters are given in Table 4.4.

that shows discernible extended structure (Fig. 4.8). By visual inspection, we find that source sizes more than an order of magnitude smaller[1] can also fit the data reasonably well but result in point-like images at these resolutions and leave larger model residuals. Sources a factor of two larger, on the other hand, are clearly unfavorable by both visual inspection and the MCMC analysis.

Of the possible choices for explaining the data, we prefer the option that the source is extended and differentially magnified. As radio sources are likely to be more extended than their optical or mid-infrared counterparts, this seems to be the most natural choice. Furthermore, finite source size effects would likely be required in order to simultaneously explain the flux ratio anomalies in the mid-IR as well. We note, however, that due to the non-Gaussianity and correlation of the noise in the immediate regions surrounding the lensed images, we do not strictly limit our conclusions by the results of the MCMC analysis. Instead, we provide a conservative upper limit of 200 mas for the source size. For sources larger than this, a visual inspection of the model residuals clearly shows that the source has become too large.

4.4.3 RX J0911+0551

RX J0911+0551 (Bade et al. 1997) is a cusp-configuration lens system, with three close images (A, B and C) and a fourth image some distance to the west. The mass environment is relatively complicated; the lens lies close to a massive cluster about 40″ away and in addition to the primary galaxy, a second galaxy lies close to the system, complicating the process of mass modelling. Our VLA 5-GHz image is shown in Fig. 4.9 and has a noise level of just under 2μJy/beam. All four lensed images are clearly detected in the radio map, and in addition we detect radio emission at the position of the lensing galaxy. We do not detect any of the components in the e-MERLIN 1.5 GHz image, which has a noise level of 16μJy/beam.

To quantify the non-detection, and thus derive limits on spectral index between the e-MERLIN and VLA observations, the e-MERLIN observation was conservatively simulated with four components of the size of the VLA beam ($\sim$500 mas), whose flux densities were given by the VLA map. Gaussian noise was added to the map at the same level as the observations (i.e. RMS 16μJy). The components were used to generate a $u-v$ dataset with the sampling function and noise level of the actual e-MERLIN observations. This was imaged and the lower limit on the spectral index resulted from the input fluxes for which the components could just not be recovered from the simulated image by model fitting. The lower limit on the spectral index was found to be $\alpha = -0.5$.

[1]The image plane is appropriately oversampled to ensure that fluxes are calculated accurately.

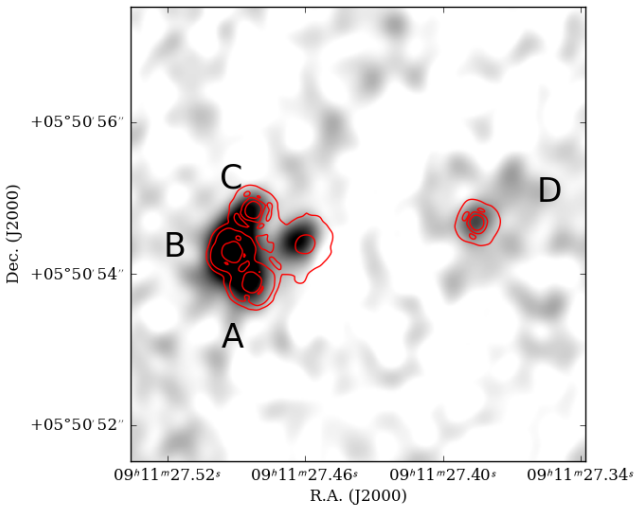

Figure 4.9 JVLA radio map of RX J0911+0551 (greyscaled from 0 to 20μJy) with contours from archival HST/NICMOS data superimposed, aligned on image D. The beam is of FWHM 560×390 mas in position angle −39.2°. The three close images to the left are A,B,C (from south to north), and image D is at the right of the picture. The lensing galaxy (between the images) is radio-loud, with a flux density of about 16μJy.

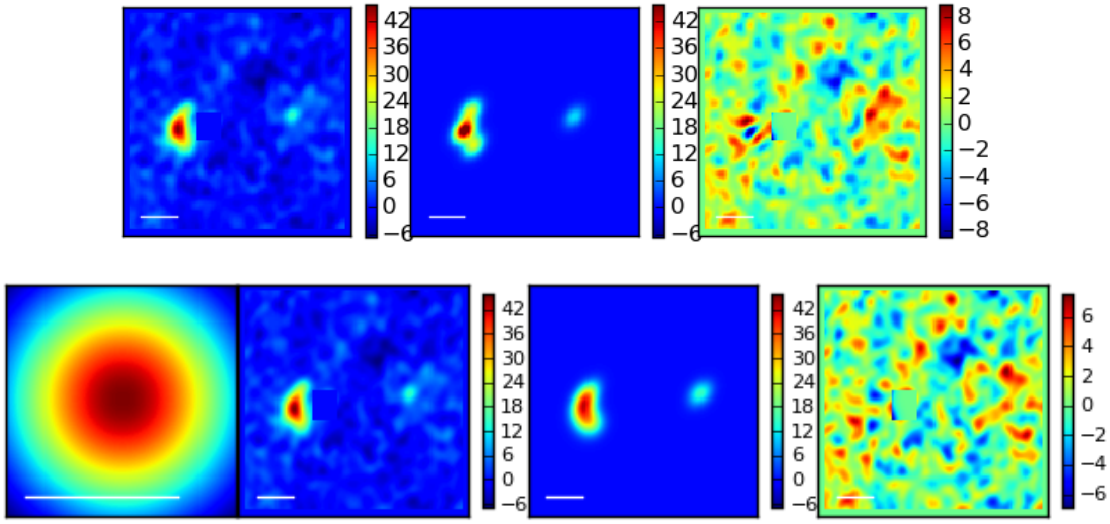

Figure 4.10 Models of RXJ 0911+0551, using a point-source model fit (above, see text). The data, model, and residual are plotted. In this case, the point-image model appears to have significant difficulty in fitting the A-B-C complex at the eastern end of the system. The bar in each panel represents 1″. Model using an extended source (below). The panels contain the source plane, the data, the model and the residual. The area around the galaxy has been blanked and excluded from the fit. In all cases the numbers on the colourbars are in μJy/beam; the source panel colourscale is arbitrary, but the source parameters are given in Table 4.4.

We have again attempted to model the image plane, represented by the VLA map, as a sum of point spread functions whose relative position is determined by the HST astrometry (Fig. 4.10). Here it does appear that point models have difficulty in reproducing the structure, in particular the shape of the A-B-C complex, although we recover good estimates for the flux densities of each image (Table 4.3). The flux densities of the A,B and C images in the radio have a ratio very close to 1:2:1, close to that expected by the cusp relation and suggesting that substructure does not need to be invoked in this case. This contrasts with the optical flux densities, and in particular with the flux density ratio 2:2:1 between A, B and C measured by Burud et al. (1998). Hence the optical measurements are almost certainly affected by microlensing. By contrast, Sluse et al. (2012a) model this lens using astrometric constraints and a model consisting of a singular isothermal ellipsoid plus shear. They obtain image flux ratios (A:B:C:D) of 1:1.87:0.88:0.34. Our corresponding values are 1:2.05:0.73:0.35, consistent within the errors with Sluse et al.'s model. The source flux density predicted by this lens model is about 5μJy.

Motivated by the residuals observed in the point-source model, we have again fitted a model in which a Gaussian-shaped extended source is lensed. Provided that the source size is not very small, neither it nor the source shape is well constrained (Table 4.4). The modelled shear is large, suggesting that we are seeing the influence of the cluster to the south. The good overall fit to the data, χ^2=3518 for 2290 degrees of freedom, gives no significant evidence for effects of substructure in the lens galaxy.

4.4.4 SDSS J0924+0219

SDSS J0924+0219 (Inada et al. 2003a) is a very interesting object because it has such a large optical flux anomaly, almost certainly as a result of microlensing (Morgan et al. 2008). This anomaly decreases with increasing observation wavelength (Floyd et al. 2009) allowing the size of the accretion disk to be measured, but the anomaly persists over a period of ∼7 years (Faure et al. 2011) raising the possibility that some of it may be due to the effects of lensing by substructure.

Although we detect the object at a reasonable level of significance (Fig. 4.11), we unfortunately do not have sufficient signal-to-noise, in the three hours of observation time allocated to this object, to measure the flux densities separately. At a total flux density of $\sim 15\mu$Jy, this is by far the weakest of the objects studied. Using an isothermal model, plus external shear, fitted to the positions reported by Inada et al. (2003a), we obtain magnifications for the four components (A, B, C and D) of approximately 13, 5, 5 and 11. Our overall flux density of $\sim 50\,\mu$Jy implies an unlensed source flux density of about 1.5μJy. This is the second faintest radio source yet detected, the faintest being SDSS J1004+4112 (Jackson 2011); further observations of the sample of radio-quiet quasars are likely to yield the first detected nano-Jy radio source.

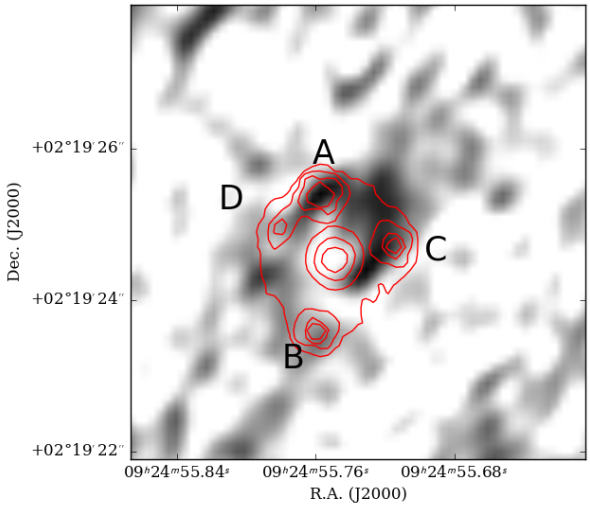

Figure 4.11 VLA radio map of SDSS J0924+0219, with greyscale from 0 to 20μJy/beam, and a restoring beam of 696×416 mas in PA −43°. The object is detected, but individual flux densities for the images are impossible to measure. Image registration to archival HST/NICMOS data (contours) has been done by eye, but this procedure is not well-defined to better than the absolute astrometry of the HST image.

4.5 Discussion and conclusions

4.5.1 Radio properties of the lensing galaxies

We detect the lensing galaxy in only one of the four objects: RX J0911+0551, at a level of 18μJy. The radio flux density of the lensing galaxies in the other three objects is $< 6 - 8\mu$Jy (3σ).

The lensing galaxy flux density in RX J0911+0551 corresponds to a luminosity of 5×10^{22} W Hz^{-1}, which is at the top of the range that can plausibly be attributed to star formation; this range is bounded by the 10^{21} W Hz^{-1} of the Milky Way and 10^{23} W Hz^{-1} for extreme star-forming galaxies. It is also close to the boundary between star-forming radio emitters and AGNs found by Kimball et al. (2011) in their study of radio luminosity functions of nearby ($z \sim 0.2$) AGN. There is no evidence for ongoing star formation in the lens galaxy, which seems to be an early-type galaxy, in other wavebands. For example, Burud et al. (1998) conducted optical and near-IR imaging and found that the lensing galaxy has a similar red colour to that of nearby members of the cluster of which it is part.

4.5.2 The nature of radio-quiet quasars

This work has resulted in the measurement of radio flux densities, and in some cases resolved radio structure, in a significant number of radio-"quiet" lensed quasar systems. Such radio sources, if unlensed, would be beyond the reach of current instruments in all but exceptional observing times, and are objects whose study will only become routine with the SKA. The luminosity of an object of intrinsic flux density of 1μJy and flat spectral index is about 1.0×10^{21}WHz^{-1} at $z = 0.5$, 5×10^{21}WHz^{-1} at $z = 1$ and 30×10^{21}WHz^{-1} at $z = 2$, orders of magnitude below what is typically accessible with current surveys except at low redshift (e.g. fig. 4 of Condon et al. 2013). Previous studies of radio-quiet quasars have focused on optically bright quasars, such as the Palomar Green sample (Kellermann et al. 1994). In accordance with the radio-optical correlation noticed by White et al. (2007), these objects have typical radio flux densities of a few hundred μJy, two orders of magnitude brighter than the intrinsic flux densities of the objects studied here.

We have observed four of the 15 known optically-selected, four-image quasar lenses with $\delta > -20°$, and all of them have intrinsic radio flux density of between 1 and 5μJy. Of the other nine, three are known to have significant radio emission. PG1115+080 has VLA archival data at 8.4 GHz taken in the compact (D) configuration, which yield a total radio flux density of 153$\pm$17 μJy, although the resolution of a few arcseconds does not allow the flux density of individual components to be determined. However, the likely magnifications in this lens system suggest that the intrinsic flux density of the source

is also a few μJy. A similar result can be derived for the lens system RX J1131−1321, which was found to have significant radio emission by Wucknitz & Volino (2008). Finally, H1413+117 is a radio-intermediate object which has been studied with the VLA by Kayser et al. (1990). Further lenses from the COSMOS survey (Faure et al. 2008; Jackson 2008) do not have significant radio emission (Schinnerer et al. 2007, 2010) in the VLA-COSMOS survey, and three quad lens systems from the Sloan Quasar Lens Search (SDSS J1138+0314, SDSS J1251+2935, SDSS J1330+1810) do not yet have deep radio imaging. It is therefore likely that at least half of optically-selected quasar lens systems will show radio emission at the micro-Jansky level, if examined carefully, and a more complete census will be the focus of future work.

The existing data are plotted in Fig. 4.12. The radio fluxes have been derived from the literature (see the figure caption), with in some cases a limit of 1 mJy inferred from their absence from the FIRST 1.4-GHz catalogue. The current sample is small. However, we note that the median radio flux density inferred by White et al. (2007) from their stacking analysis is about 50-70 μJy at $20 < I < 21$. This, combined with the distribution of detections in our optically-selected sample, suggests that there is a large scatter in radio flux densities at this optical magnitude, if not an outright bimodality.

There are a number of theoretical models for the origin of radio emission in radio quiet quasars, each of which makes rather different predictions for what should be observed. The first possibility is that of a smaller version of a radio-loud quasar, where a flat-spectrum radio core and steeper-spectrum radio jet emission are present in some ratio (Urry & Padovani 1995, Ulvestad et al. 2005). In this case, we would expect steep-spectrum emission on scales of parsecs to tens of parsecs in addition to a compact, flat-spectrum radio core. A second possibility is the emission from radio starbursts in a similar manner to nearby examples such as M82 (e.g. Condon et al. 2013). This emission is expected to be optically thin synchrotron from supernova remnants, but should extend over most of the galaxy disk and therefore have a characteristic size of about 1 arcsecond, or 5-10 kpc; studies of star-forming radio sources in the *Hubble Deep Field* (HDF), with mean redshifts around 1, have shown that the radio emission nearly always displays a similar characteristic size (Muxlow et al. 2005). Alternatively, the radio emission could be produced by thermal processes close to the accretion disk. Suggestions for this include optically thin free-free emission from a disk wind (Blundell & Kuncic 2007) and emission from magnetically-heated coronae (Laor & Behar 2008). In both cases the emission would be expected to originate close to the centre. In the case of disk winds, this scale is likely to be at least 0.1–1pc, but for magnetically heated coronae the scale would be smaller. In both these cases, however, the radio spectral index should be approximately flat.

We can use our data to confront the models in a number of ways. The first relevant result is the source sizes implied by our lens modelling, which are of the order of 70 pc in

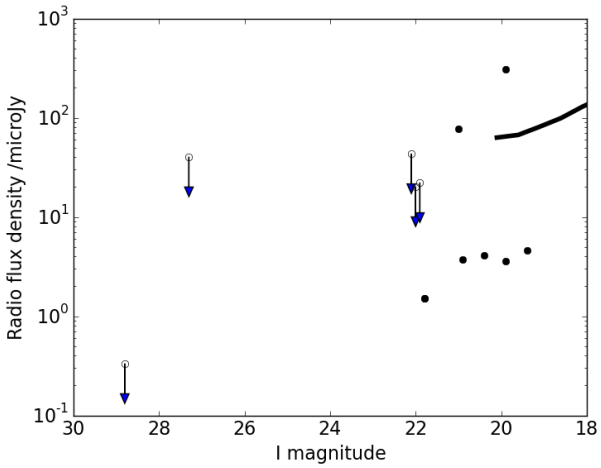

Figure 4.12 Intrinsic radio flux densities versus intrinsic I-band magnitudes for a sample of optically-selected quasar lenses. Both radio and optical flux densities have been demagnified using lens models. Data and models have been derived from Ratnatunga et al. 1999, Wisotzki et al. 2002, Reimers et al. 2002, Burud et al. 1998, Inada et al. 2003a,b, Ghosh & Narasimha 2009, Anguita et al. 2009, Jackson 2011, Wucknitz & Volino 2008, Kayo et al. 2007, Oguri et al. 2008, Assef et al. 2011, in some case supplemented by further modelling. The locus of radio vs. optical flux densities reported by White et al. (2007) is sketched near the top right.

HS 0810+2554. In HE 0435−1223 we find a characteristic size which is more uncertain, but probably greater than a few milliarcseconds and certainly less than 200 mas (<2 kpc). In RX J0911+0551 we again detect a significantly extended source, but whose size is likely to be 100-150mas (∼1 kpc) rather than the larger values which would be expected for a typical star-forming region in a radio source. Either we have an unrepresentative sample, or the star-formation model is disfavoured compared to the non-thermal AGN hypothesis. This is in contrast to the inference of star-formation as the cause of the radio emission, made by Wucknitz & Volino in the case of RX J1131−1231. A definitive test should be available using VLBI, as a non-thermal source should contain high-brightness emission at the μJy level which is detectable with current VLBI sensitivities.

A second, although rather more equivocal, result concerns the measured spectral indices. The spectral index of the radio emission in HS 0810+2554 appears to be steep, consistent with synchrotron emission from either a non-thermal source or a star-forming component. Both the spectral index and the characteristic size disfavour coronal emission and emission from disk winds, which would be expected to be relatively flat-spectrum and to be emitted from a smaller region. However, the VLA and e-MERLIN observations of RX J0911+0551 may be consistent with such models. Because the spectral index limit is currently relatively loose ($\alpha > -0.5$), further e-MERLIN observations are needed to make a more definite statement.

4.5.3 Substructure in lensing galaxies

Radio flux densities in four-image lens systems are important because they potentially give indications of substructure in lensing galaxies (or along the line of sight), in the form of flux anomalies (Mao & Schneider 1998; Dalal & Kochanek 2002). In particular, violations of the cusp and fold relation allow us to quantify the levels of substructure present (e.g. Xu et al. 2015, 2009). Flux ratios between images can also be affected by propagation effects (scattering in the case of the radio waveband), microlensing (in the case when the source is smaller than the intrinsic size of the Einstein radius of stars in the lensing galaxy, or about 1 μarcsec), variability (in the case of a source which varies significantly over the time delay between the images) and source size (which can affect flux ratios, e.g. Amara et al. 2006; Metcalf & Amara 2012). The use of cusp and fold relations, rather than the observation of disagreement with a smooth model, is important because otherwise the effect of substructure on the image flux ratios can be partially absorbed by varying the smooth model.

We detect no new evidence in our objects for substructure. Indeed, the flux ratios of RX J0911+0551 obey the cusp relation within the errors of the measured radio flux densities. The flux ratios of the fold system HS 0810+2554 are also consistent with a smooth model, as the brightnesses of the merging images are equal to within the er-

rors, unlike the optical case in which microlensing affects one of the images. The case of HE 0435−1223 is more interesting. Here we obtain flux density ratios which are inconsistent with not only the optical, but also the mid-IR bands. There are a number of explanations for this which we do not favour. Radio microlensing could affect the radio flux densities, but would require a very small radio source size (microarcseconds rather than milliarcseconds). Variability of the radio source, together with a time-delay, is also possible. However, intrinsic variations in typical radio-faint quasars are on timescales of several weeks to months with fluctuations at the $10 - 20\%$ level (Barvainis et al. 2005). In order to reproduce these observations, a variation in the source flux of $\sim$40% would be required within the time-delay scales measured by Courbin et al. (2011) (-6.5 and -14.3 days for B-D and C-D respectively). Flux anomalies due to variations in the mid-IR are still less likely, because the L'-band is expected to have a significant contribution from a dusty torus, whose size is $\gtrsim$ 1pc, implying a light crossing-time of several years or more. Differential extinction due to dust at non-radio wavelengths is not a likely culprit, as the colours (Wisotzki et al. 2002) and the continuum slopes (Morgan et al. 2005; Wisotzki et al. 2004) are nearly identical for the four lensed images. While substructure can be used to explain the various flux ratio anomalies seen in the optical, mid-IR, and radio, it may prove difficult and would perhaps require fine-tuning to simultaneously explain all the observations with substructure alone. Instead, at least some of the explanation is likely to be the effects of finite source sizes; especially given the results in the other objects, an intrinsic radio source size of order a few parsecs is the explanation that we favour.

Chapter 5

Dark matter subhaloes as millilenses

We use 13 gravitational lens systems with quadruply imaged QSOs and their observed flux ratio anomalies obtained using data in mid-infrared, radio or spectral narrow lines as a baseline, to estimate the amount of substructure in the dark matter halo of lens galaxies. We assume that the smooth gravitational potential of the galaxies is well modeled by a Singular Isothermal Ellipsoid (SIE) plus external shear (gamma) along with an additional Singular Isothermal Sphere (SIS) in some cases, and that the cause of the flux ratio anomalies is dark matter subhalos described by pseudo-Jaffe density profiles. After excluding 5 of the systems from the analysis due to various concerns, our Bayesian estimate for the Einstein radius of the subhalos (as a fraction of the Einstein radius of their corresponding lens galaxy) is $b = 0.0003^{+0.0005}_{-0.0002}$, and their abundance (as a fraction of the total surface density of the lens galaxy at the image positions) is $\alpha = 0.075^{+0.030}_{-0.021}$.

5.1 Introduction

As seen in previous chapters, and explained in detail in Section 1.3.2, cosmological simulations in the Cold Dark Matter (CDM) paradigm predict an amount of substructure in the dark matter haloes of galaxies in the form of a number of subhaloes or satellites that is much higher than the number of luminous satellites observed around the Milky Way and other galaxies. In the inner regions of the galaxy haloes, about 1% of the mass is expected to remain in satellites that survived tidal effects, with the fraction rising to about 10% when we consider the total mass of the dark matter halo (e.g. Zentner & Bullock 2003). The number of satellites in each galactic halo is predicted to be in the hundreds or even thousands, and the absence of such high numbers of dwarf galaxies around larger ones is known as the dark matter satellites problem.

One of the possible explanations is that these subhaloes do indeed exist, but baryonic processes have depleted them of most or all of their luminous matter. If this is the case, then they would only be detectable via their gravitational interactions, and gravitational lensing becomes an important tool when attempting to solve this problem. The presence of a distribution of such clumps of matter has an effect in the lens potential, and quasar lensing could be used to probe it. As explained in Section 1.1.2, the magnification of each of the multiple images generated of a lensed QSO is sensitive to the second derivative of the lens potential, so the presence of substructure could alter their flux ratios.

Indeed, observations of lensed quasars in wavelengths that should not be affected by differential extinction or microlensing have shown fluxes that are hard to explain by modeling the smooth potential of the lens (Kochanek 1991). Many studies have been performed using these anomalies to probe for the presence of these dark matter subhaloes, but the results are still inconclusive. While some claim a consistency between the CDM model and the observations (e.g. Bradač et al. 2004; Dalal & Kochanek 2002; Dobler & Keeton 2006; Metcalf & Amara 2012), others find that the anomalies present are too large to be explained by CDM (Amara et al. 2006; Chen et al. 2011; Macciò & Miranda 2006; Macciò et al. 2006; Mao et al. 2004; Xu et al. 2009, 2010), perhaps due to poor estimations of the lens models or other effects unaccounted for.

In this chapter we will compile a sample of lens systems with quadruply imaged QSOs that have observations of their flux ratios in optical narrow lines, mid-IR or radio, and use it to derive the abundance and average mass of dark matter subhaloes in galaxies from the flux ratio anomalies. While keeping possible drawbacks in mind, we will assume that the mass distribution of the lens galaxies is well described by simple models consisting on Singular Isothermal Ellipsoids plus external shear (SIE + γ) and an extra Singular Isothermal Sphere (SIS) in some cases. Another assumption will be that the anomalies of the observed flux ratios when compared to the predictions of these models are only due to millilensing caused by the dark matter satellites. In Section 5.2 we describe the sample of lens systems used in this work, in Section 5.3 we explain the procedure followed in our calculations, and show our results in Section 5.4. We discuss our findings in Section 5.5, and then in Section 5.6 we explain the possible drawbacks of the assumptions we employed and the future work needed for a more robust study.

5.2 Our sample of lens systems

Given that our goal is to compare the flux ratios observed in lens systems with the ones predicted by smooth models of their mass distribution, we need models that do not use the flux ratios as constraints but are still sufficiently constrained to give useful predictions. Therefore, in this work we only use lens systems where the source quasar is quadruply

imaged (also referred to as 'quads'). Out of these, we select those that already had been observed in wavelengths that would be emitted by regions of the source too big to be affected by stellar microlensing, which are spectral lines in visible light or near infrared which would come from the narrow-line region of the AGN, mid-infrared light that would have been emitted from the dusty torus, or radio waves from the jet or other large regions. Mid-infrared and radio wavelengths are also unaffected by extinction in the interstellar medium, and extinction in the optical would affect both the narrow lines and the continuum and it can be accounted for, so we can assume that these observations provide the true flux ratios between the quasar images. Whenever possible, we use mass models for these systems from Sluse et al. (2012a), Schechter et al. (2014) or Xu et al. (2015). The paper by Schechter et al. (2014) is particularly useful because it provides the convergence (κ) and shear (γ) of the potential at the locations of the quasar images that we need to generate magnification maps, so we use their models even if other fits are available in other sources. Our sample of lens systems is listed in Table 5.1 with the predicted and observed flux ratios in the different wavelengths, as well as the flux anomalies derived and expressed in magnitudes. Despite obtaining flux ratios also for HS 0810+2554 in Chapter 4, it was excluded from our data due to the undoubtedly extended size of the source and the absence of a redshift for its lens galaxy.

5.3 Methods

Once we have the predictions for the flux ratios in each system given by the mass models, and the flux anomalies from the difference between these and the observations, we assume for our calculations that the anomalies are entirely due to the presence of a distribution of dark matter subhaloes acting as "millilenses". We then try to estimate the mean Einstein radius b of these subhaloes, and their abundance α expressed as the fraction of the lensing convergence κ that is present as subhaloes instead of a smooth potential.

In this work we follow a procedure with some similarities to the one used in chapters 2 and 3 when estimating the size of the accretion disk. We will calculate the effect of a distribution of lenses in the flux ratios of the system by generating magnification maps for each of the quasar images, compare the predictions to the observations, and then obtain probability density functions (PDFs) by repeating the process to cover the range of parameters that we want to study. The main difference, however, is that this time our goal is not to estimate the properties of the source but of the structure of the galaxy lens itself. When estimating the scale radius and the exponent of the quasar accretion disk, we kept the distribution of stars fixed for all cases, and only four magnification maps had to be produced (one for each of the quasar images), which could then be convolved with the source intensity profile corresponding to each set of parameters to perform all the necessary calculations. This time we keep the size of the source fixed and it is the

Table 5.1. Predicted and observed flux ratios in our sample of lens systems

Object	Model (constraints)	Ratios	Model	Line	IR	Radio	Δm_{lin}	Δm_{IR}	Δm_{radio}
B 0128+437[0,3]	SIE + γ	B/A	0.72	—	—	0.58	—	—	0.23
	($\vec{x}_i$, $\vec{x}_{G1}$)	C/A	0.40	—	—	0.52	—	—	-0.28
		D/A	0.48	—	—	0.51	—	—	-0.07
MG 0414+0534[1,4]	SIE + γ + SIS	A2/A1	1.03	—	0.90	0.90	—	0.14	0.14
	($\vec{x}_i$, $\vec{x}_{G1}$, $\vec{x}_{GX}$)	B/A1	0.29	—	0.36	0.37	—	-0.25	-0.28
		C/A1	0.15	—	0.12	0.15	—	0.22	0.00
HE 0435-1223[1,5,6]	SIE + γ	A/C	0.94	1.41	—	1.05	-0.44	—	-0.12
	($\vec{x}_i$, $\vec{x}_{G1}$)	B/C	1.02	1.08	—	0.77	-0.06	—	0.31
		D/C	0.61	0.79	—	0.47	-0.28	—	0.28
B 0712+472[2,3]	SIE + γ	B/A	1.08	—	—	0.84	—	—	0.27
	($\vec{x}_i$, $\vec{x}_{G1}$)	C/A	0.27	—	—	0.42	—	—	-0.48
		D/A	0.06	—	—	0.08	—	—	-0.36
RX J0911+0551[1,6]	SIE + γ + SIS	B/A	1.85	—	—	1.98	—	—	0.08
	($\vec{x}_i$, $\vec{x}_{G1}$)	C/A	0.85	—	—	0.73	—	—	-0.17
		D/A	0.34	—	—	0.35	—	—	0.03
SDSS J0924+0219[1,7]	SIE + γ	B/A	0.43	0.38	—	—	0.13	—	—
	($\vec{x}_i$, $\vec{x}_{G1}$)	C/A	0.43	0.18	—	—	0.95	—	—
		D/A	0.90	0.10	—	—	2.39	—	—
PG 1115+080[1,8]	SIS + SIS	A2/A1	0.95	1.00	0.93	—	-0.05	0.03	—
	($\vec{x}_i$, $\vec{x}_{G1}$)								
RXS J1131-1231[1,9]	SIE + γ	A/B	1.62	1.97	—	—	-0.21	—	—
	($\vec{x}_i$, $\vec{x}_{G1}$)	C/B	0.94	1.33	—	—	-0.38	—	—
B J1422+231[1,3,10]	SIE + γ	B/A	1.18	1.11	0.85	1.06	0.07	0.36	0.11
	($\vec{x}_i$, $\vec{x}_{G1}$)	C/A	0.62	0.54	0.57	0.55	0.15	0.09	0.13
		D/A	0.05	0.03	—	0.02	0.54	—	0.49
B 1555+375[2,3]	SIE + γ	B/A	0.96	—	—	0.62	—	—	0.47
	($\vec{x}_i$, $\vec{x}_{G1}$)	C/A	0.43	—	—	0.51	—	—	-0.18
		D/A	0.25	—	—	0.09	—	—	1.17
B 1608+656[0,11]	SIE + γ + SIS	A/B	1.95	—	—	2.04	—	—	-0.05
	($\vec{x}_i$, $\vec{x}_{G1}$, $\vec{x}_{G2}$)	C/B	0.81	—	—	1.04	—	—	-0.27
		D/B	0.17	—	—	0.35	—	—	-0.79
WFI J2033-4723[1,12]	SIE + γ + SIS	A1/B	1.56	1.48	—	—	0.06	—	—
	($\vec{x}_i$, $\vec{x}_{G2}$)	A2/B	0.92	1.05	—	—	-0.14	—	—
		C/B	0.62	1.39	—	—	-0.88	—	—
Q 2237+0305[13]	SIE + γ	B/A	0.89	0.81	0.97	1.08	0.10	-0.09	-0.21
	($\vec{x}_i$, $\vec{x}_{G1}$)	C/A	0.45	0.88	0.51	0.55	-0.73	-0.13	-0.22
		D/A	0.82	1.09	0.92	0.77	-0.31	-0.13	0.07

[0]Model ratios from Sluse et al. (2012a).

[1]Model ratios from Schechter et al. (2014).

[2]Model ratios from Xu et al. (2015).

[3]Radio flux ratios from Koopmans et al. (2003).

[4]Mid-IR flux ratios from Minezaki et al. (2009), radio flux ratios from Rumbaugh et al. (2015).

[5]Emission line flux ratios from Table 3 of Wisotzki et al. (2003).

[6]Radio flux ratios from Jackson et al. (2015).

[7]Lyα flux ratios from Keeton et al. (2006).

[8]Optical emission line flux ratios from Popović & Chartas (2005). Mid-IR data from Chiba et al. (2005).

[9][OIII] emission line flux ratios from Sluse et al. (2007).

[10]Optical emission line flux ratios from Impey et al. (1996). Mid-IR data from Chiba et al. (2005).

[11]Radio flux ratios from Fassnacht et al. (1999b).

[12]Optical emission line flux ratios from Morgan et al. (2004).

[13][OIII] emission line flux ratios from Wayth et al. (2005). Mid-IR and model flux ratios from Vives-Arias et al. (2016). Radio flux ratios from Falco et al. (1996).

distribution of lenses what has to vary for each set of parameters, which means a new magnification map is needed each time the input parameters change.

There are some special cases that arise with this method and have to be taken into consideration:

- *Subhaloes are too big.* Since one of the parameters we vary is the Einstein radius of the millilenses, there are cases at the high-mass end in which only part of the caustics pattern of each subhalo will fit in the map, at most. The size of the maps cannot be increased indefinitely, because the local approximation of using only the convergence and shear to characterize the global potential would break down, and also the region has to be small enough for the millilensing magnification maps associated with each image to be statistically independent. The alternative is to generate a large number of maps of a given size in order to achieve good statistics.

- *Not enough subhaloes.* Likewise, low values of α for the high-mass lenses could cause a situation in which there are so few millilenses that there are barely any or even no caustics in the map, or perhaps zero subhaloes placed in the lens plane to begin with. In these cases, aside from the higher number of maps, the area in which the lenses are placed has to be enlarged so that at least two subhaloes cause deflection in each light ray, even from afar. This is important for an accurate calculation of the smooth regions of the map between caustics, which will dominate the magnification probabilities.

- *Too many subhaloes.* Finally, with high abundances of substructure with lenses of the lowest masses we can be in the opposite situation, with far too many millilenses that would have to be taken into account when calculating the deflection of every single light ray to generate the map. One way of solving this problem is to produce a higher number of smaller maps instead of fewer large ones, because even though the total cumulative area in the source plane might be the same, a fewer number of lenses are deflecting each ray and computations will be much faster.

The need to generate a large number of maps of different sizes for each quasar image makes it impractical to calculate the probability of reproducing the observations by using the exact same procedure as when calculating the size of the accretion disk with stellar microlensing (selecting a random location in each of the four magnification maps, obtaining the probability of reproducing the observations by computing the χ^2 of the flux ratios between those locations to the observed ones, adding that probability to the total and iterating the process). The large areas would be poorly sampled by a random selection of locations in the maps when few caustics are present, so we would have to greatly increase the number of positions used in the calculation and then use the same large number in the cases with a lot of caustics to keep the probabilities consistent, even though they would

have been properly sampled with a number of points several orders of magnitude lower. Also, we would have to store in memory all the maps generated for the four images of the system for each pair of parameters, and guarantee that the random selection of points takes place in all possible combinations between the high number of maps generated for each of the images.

Given the limitations stated above, we take a more computationally efficient approach to estimate the probability of observing millilensing magnifications Δm_I^{obs} ($I = \{A, B, C, D\}$) conditioned to the parameters α and b that is not based on the χ^2 test but on the definition of probability of independent events, directly. We define:

$$P(\Delta m_I^{obs}|\alpha, b) = \prod_{I=A,B,C,D} P_I(\Delta m_I|\alpha, b), \tag{5.1}$$

where $P_I(\Delta m_I|\alpha, b)$ are the individual PDFs for each image calculated from the millilensing magnification maps. Millilensing magnifications are not directly measureable, but they can be written as

$$\Delta m_I^{obs} = m_I - m_0 - \mu_I \tag{5.2}$$

where m_0 is the unknown intrinsic magnitude of the source, m_I is the observed magnitude of image I and μ_I is the macrolensing magnification for that image. From the equations for the four images we can derive three constraints,

$$\Delta m_I^{obs} - \Delta m_A^{obs} = m_I - m_A - (\mu_I - \mu_A), \tag{5.3}$$

and equation 5.1 can be rewritten like

$$P(\Delta m_I^{obs}|\alpha, b) = P_A(\Delta m_A|\alpha, b) \prod_{I=B,C,D} P_I(m_I - m_A - (\mu_I - \mu_A) + \Delta m_A|\alpha, b). \tag{5.4}$$

We can now marginalize over the unknown variable, Δm_A, and define:

$$P_{marg}(m_I - m_A - (\mu_I - \mu_A)|\alpha, b) = \int P_A(\Delta m_A|\alpha, b) \prod_{I=B,C,D} P_I(m_I - m_A - (\mu_I - \mu_A) + \Delta m_A|\alpha, b) d(\Delta m_A). \tag{5.5}$$

It is easy to check, by direct substitution of A by any other image, that this probability does not depend on the choice of reference image in equations 5.3. In fact, in equation 5.5 we integrate over all the domain of a dummy variable the product of the PDFs of A, B, C, and D, with relative displacements between each (I, K) pair of $(m_I - m_K) - (\mu_I - \mu_K)$, independent of the choice of reference image.

On the other hand, an equation equivalent to Eq. 5.5 is obtained by substituting equations 5.2 in 5.1 and marginalizing with respect to the intrinsic magnification:

$$P_{marg}(m_I - \mu_I|\alpha, b) = \int \prod_{I=A,B,C,D} P_I(m_I - m_0 - \mu_I|\alpha, b) dm_0 \tag{5.6}$$

The problem with Eq. 5.5 appears (exactly as in the case of the χ^2 approach) when we take into account the errors. In principle, to obtain the error-corrected PDF for each image we only need to convolve the PDF without considering errors, $p_I^0(\Delta m|\alpha, b)$, with a normal distribution of variance σ_I^2:

$$P_I(\Delta m|\alpha, b) = P_I^0(\Delta m|\alpha, b) * N(0, \sigma_I^2). \tag{5.7}$$

However, in Eq. 5.5, what we have are the PDFs of the differences of two random variables, $(m_I - m_A)$. These PDFs can be obtained from the convolution of the PDFs of each individual random variable but, when the errors are taken into account, they can no longer be considered independent (the same thing happens in the case of the χ^2 approach), and then the product of the PDFs should be conditional (the non-diagonal terms of the covariance matrix are not null in the χ^2 approach).

We can circumvent this problem going back to Eq. 5.6, that is free from it (at the cost of assuming that m_0 is uniformly distributed). Taking into account that, in absence of errors, Eqs. 5.5 and 5.6 are fully equivalent, we can have reasonable expectations that Eq. 5.6 will lead to the same results as the χ^2 approach but with a huge saving in computational time.

The dark matter subhaloes are modelled using spherical pseudo-Jaffe density profiles of the form $\rho \propto r^{-2}(r^2 + a^2)^{-1}$, see Muñoz et al. (2001), with a total mass of $M = \pi b a \Sigma_{cr}$ each. We set the scale a as the tidal radius of the subhalo, $a = \sqrt{b\, b_0}$ (Dalal & Kochanek 2002), where b_0 is the Einstein radius of the lens galaxy. Given the large size expected for the components of the AGN that emit mid-IR, radio waves or narrow spectral lines in the systems of our sample, we generate magnification maps with a pixel scale of 1000 light-days to save time in the calculations by not convolving the maps with a brightness profile for the source. In order to keep them statistically independent of each other with pixels that large, their maximum size will not exceed 200×200 pixels. The values we use for the satellite mass fractions and the Einstein radii of the satellites are, respectively, $\alpha_j = 2^{-j}$ for $j = 2, \cdots, 8$ and $b_i = 10^{-4} \times 2^i$ for $i = 0, \cdots, 7$.

The implementation of the method proceeds as follows:

1. For quasar image I of a system in the sample, we set the input values for κ and γ of the lens potential at the image position, the Einstein radius b_0 of the lens galaxy, the

angular diameter cosmological distances D_{OS}, D_{OL} and D_{LS} for this system (used to calculate Σ_{cr}), and the physical distance corresponding to 1 arcsecond at the lens (all these sizes and distances for each system are shown in Table 5.2). For a given pair of values α and b, we calculate the amount of satellites that would be placed in a standard 200×200 map, and use this number to choose the factors by which the sizes of the map and the area to place the lenses have to be corrected, as well as the number of maps to be calculated in order to achieve good statistics.

2. We create a loop in which each iteration places the appropriate number of millilenses in a random distribution, computes a magnification map using the Inverse Polygon Mapping algorithm (Mediavilla et al. 2006, 2011a), divides it by the macromodel magnification given by κ and γ, expresses the result in magnitudes to obtain the millilensing anomalies Δm, and generates a histogram of the number of pixels with each millilensing anomaly in bins of 0.05 mag from -5 mag to $+5$ mag. The histograms of all iterations are added together to obtain the PDF for each case, $P_I(\Delta m_I|\alpha, b)$, by normalizing the distribution.

3. Once we have $P_I(\Delta m_I|\alpha, b)$ for all the images of the quasar and a set of parameters α and b, we calculate the probability of reproducing the observed flux ratios by multiplying these PDFs after displacing them by the observed flux ratio anomalies (shown in Table 5.1), and then integrating over the whole range of Δm (Eq. 5.5). Since the relative values for $m_I - \mu_I$ are taken into account and different values of m_0 would only change the origin of coordinates for the Δm axis, integrating over all Δm is equivalent to integrating over all m_0 if we assume it is uniformly distributed (Eq. 5.6). We repeat the process over the whole range of parameters α and b to obtain the 2D PDF for each system. When the flux ratios observed at different wavelengths for the same system differ from each other, we have chosen in this preliminary work to combine the probabilities obtained in both cases by multiplying the resulting 2D PDFs together.

5.4 Results

As a preliminary analysis, we compute the probability density functions for the abundance α and Einstein radius b of the subhaloes using ten of the systems in our sample. We left out RX J0911+0551 because its radio emission could also come from an extended region of the source rather than the few central parsecs, SDSS J0924+0219 due to the unusually large flux anomaly that could indicate the mass model used is not appropriate for this system, and B 1555+375 because a redshift of $z = 0.6$ was assumed for the lens in the calculations but it lacks an actual measurement. In the case of Q 2237+0305, we decided to only use the mid-IR flux ratios and PDF derived in Chapter 3 from observations in multiple epochs as the true flux ratio for the system, instead of combining them

Table 5.2. Angular diameter distances, physical sizes corresponding to one arcsecond, and Einstein radii of the lenses.

Object	D_{OS} (Mpc)	D_{OL} (Mpc)	D_{LS} (Mpc)	kpc / "	b_0 (")
B 0128+437	1604.5	1741.9	698.5	8.44	0.22
MG 0414+0534	1684.8	1680.6	779.8	8.15	1.11
HE 0435-1223	1765.1	1197.6	1114.8	5.82	1.20
B 0712+472	1777.0	1158.1	1079.1	5.61	0.68
RX J0911+0551	1656.8	1570.0	925.5	7.61	0.95
SDSS J0924+0219	1792.0	1124.1	1173.0	5.45	0.87
PG 1115+080	1790.4	968.4	1324.0	4.70	1.03
RXS J1131-1231	1478.2	935.9	747.1	4.54	1.78
B J1422+231	1527.1	1030.2	1228.3	4.99	0.74
B 1555+375	1790.4	1418.0	914.5	6.87	0.23
B 1608+656	1782.4	1449.9	794.9	7.03	0.71
WFI J2033-4723	1792.2	1480.1	868.6	7.18	1.06
Q 2237+0305	1788.8	164.5	1725.3	0.80	0.86

with the ratios from narrow spectral lines and radio observations, because of their higher uncertainties and the possibility that they come from regions much larger than the source size considered in our method. The resulting PDFs for the ten systems are shown in Figure 5.1, and the Bayesian estimates for the two parameters in each case are listed in Table 5.3.

The next step is to combine the systems in our sample so that we can obtain a statistical estimation for the abundance of subhaloes in galaxies and their average Einstein radius. In this work we perform a preliminary analysis by simply multiplying the PDFs of the different systems as they are, but keeping in mind that the Einstein radius of the subhaloes does not correspond to the same subhalo mass at different redshifts, and therefore the combination of PDFs might not provide an accurate value. However, the flux ratios alone are not expected to be enough to properly constrain the subhalo masses, and this effect can be seen in Figure 5.1, where in most cases the 1σ contours cover the entire range of b considered. Therefore, we do not expect the estimation to change by much were we to shift the PDFs to match the subhalo masses before combining them. It can also be seen that two of the systems, B 1608+656 and WFI J2033-4723, have a very high estimated abundance of substructure, and this raises some concerns regarding their use in a combined PDF because they already have abundances too high when compared to CDM predictions. The lens galaxy in B 1608+656 has two components that are likely

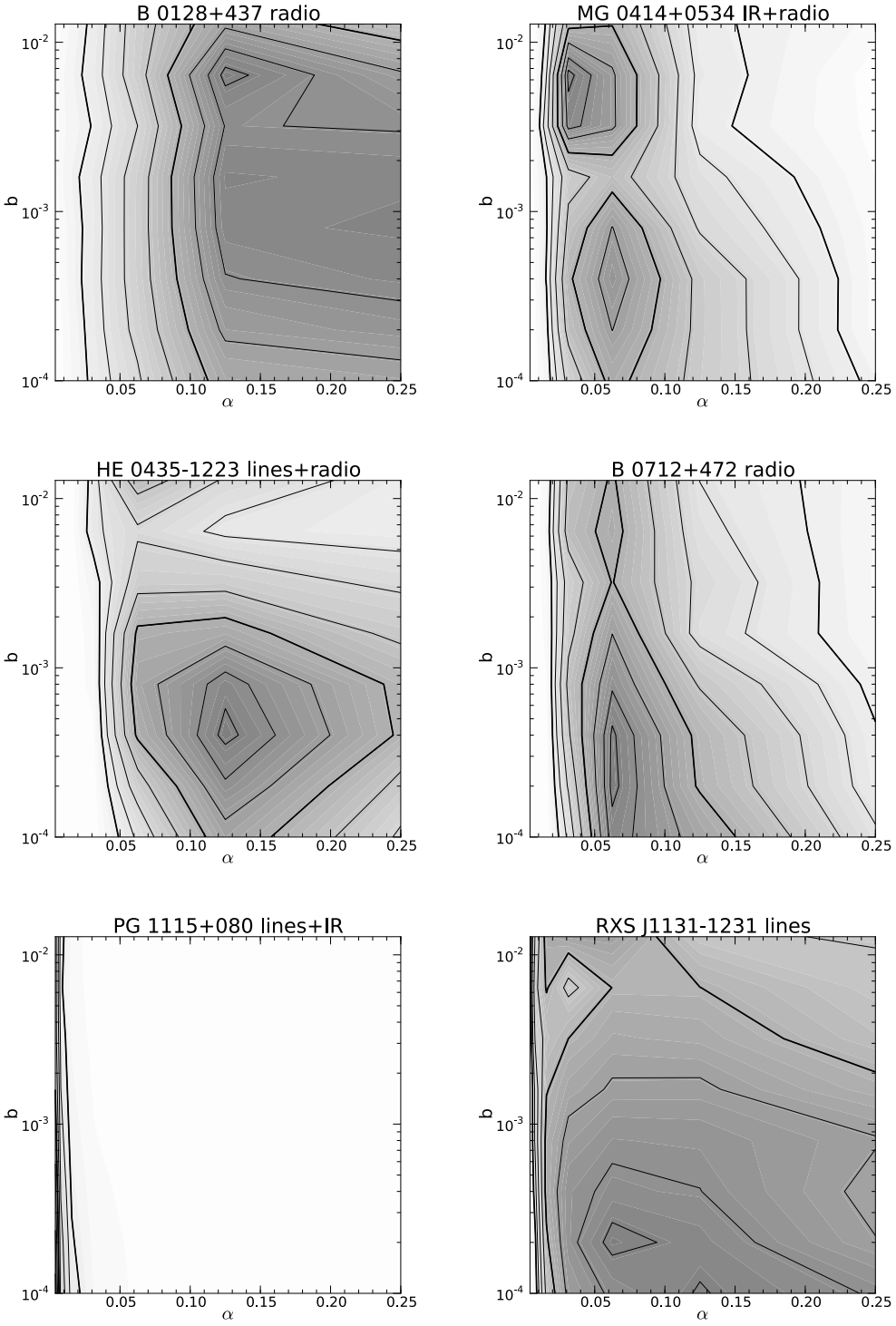

Figure 5.1 Probability density functions for the Einstein radius b (in arcseconds) and abundance α of dark matter subhaloes in gravitational lens systems necessary to reproduce the observed flux ratios in radio, mid-IR or narrow spectral lines, as indicated next to the name of each system.

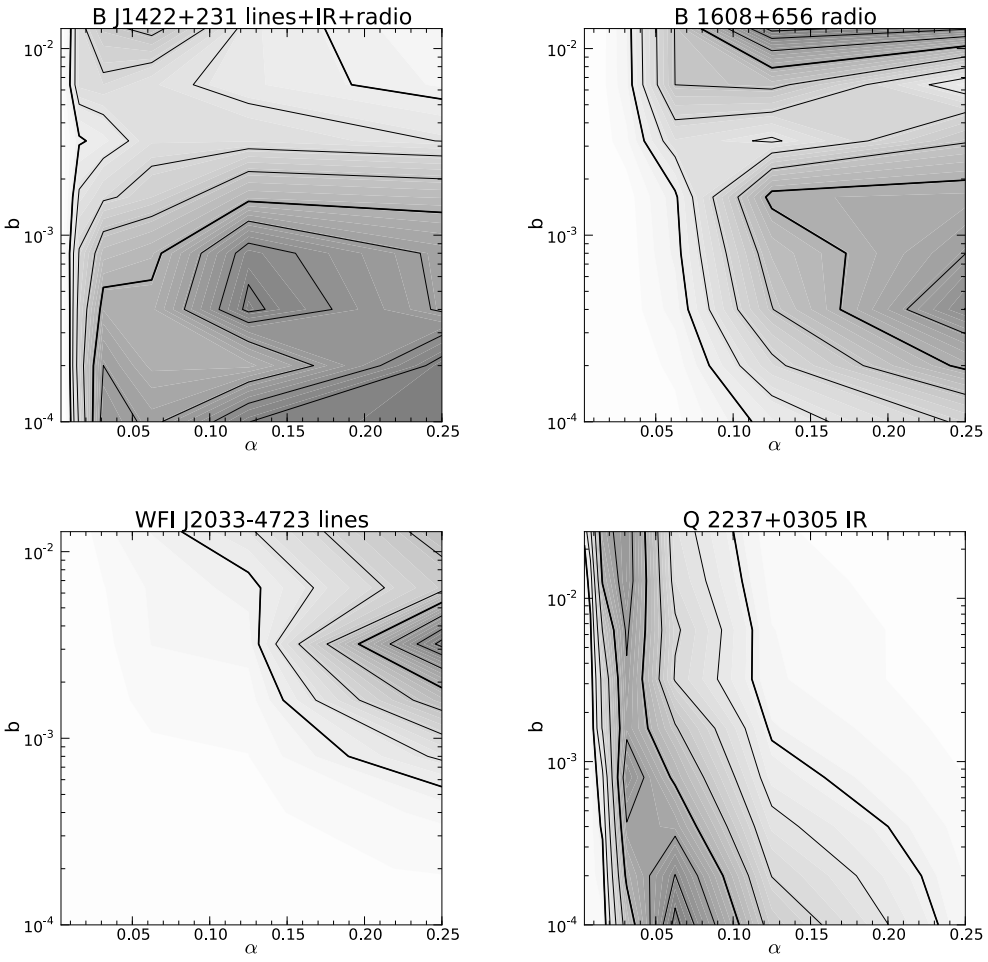

Figure 5.1 Probability density functions for the Einstein radius b (in arcseconds) and abundance α of dark matter subhaloes in gravitational lens systems necessary to reproduce the observed flux ratios in radio, mid-IR or narrow spectral lines, as indicated next to the name of each system.

Table 5.3. Bayesian estimates for the average abundance and Einstein radius of dark matter subhaloes in the lens systems.

Object	Source of ratios	α	b (")
B 0128+437	radio	$0.11^{+0.16}_{-0.06}$	$0.0011^{+0.0040}_{-0.0009}$
MG 0414+0534	IR, radio	$0.05^{+0.05}_{-0.02}$	$0.0012^{+0.0044}_{-0.0009}$
HE 0435-1223	lines, radio	$0.11^{+0.09}_{-0.05}$	$0.0009^{+0.0029}_{-0.0007}$
B 0712+472	radio	$0.07^{+0.06}_{-0.03}$	$0.0009^{+0.0034}_{-0.0007}$
PG 1115+080	lines, IR	$0.006^{+0.008}_{-0.003}$	$0.0007^{+0.0027}_{-0.0006}$
RXS J1131-1231	lines	$0.05^{+0.11}_{-0.04}$	$0.0010^{+0.0037}_{-0.0008}$
B J1422+231	lines, IR, radio	$0.07^{+0.12}_{-0.04}$	$0.0006^{+0.0020}_{-0.0005}$
B 1608+656	radio	$0.14^{+0.12}_{-0.07}$	$0.0017^{+0.0066}_{-0.0014}$
WFI J2033-4723	lines	$0.18^{+0.15}_{-0.08}$	$0.0035^{+0.0062}_{-0.0022}$
Q 2237+0305	IR	$0.033^{+0.046}_{-0.019}$	$0.0016^{+0.0084}_{-0.0013}$

interacting and this might mean that the system is not completely relaxed, so modeling it with two separate isothermal potentials could yield flux ratios that are quite different than the ones produced by the actual mass distribution. In the case of WFI J2033-4723, there are other galaxies projected at a small angular distance from the lens (i.e. typically < 10 arcsec) that were not taken into account in the modeling and might be causing extra anomalies. We therefore exclude these two galaxies, and only combine the PDFs of the eight remaining systems to produce the PDF shown in Figure 5.2. The Bayesian estimates that we obtain are an average Einstein radius $b = 0.0003^{+0.0005}_{-0.0002}$ and an abundance $\alpha = 0.075^{+0.030}_{-0.021}$.

5.5 Discussion and conclusions

In all the systems analyzed, a degeneracy between the abundance and the mass of the subhaloes can be seen. This is to be expected, as the more massive the millilenses are, the fewer of them are needed to produce flux anomalies of the magnitudes observed. Using only the magnification produced by the millilenses, this degeneracy is very hard to break, and as a result, in most of the systems the average mass of the dark matter subhaloes is practically unconstrained, with their uncertainties encompassing nearly all of the studied range. The abundances, that is, the fraction of the lensing potential that remains in the form of subhaloes, can be better analyzed. The central values of the estimations

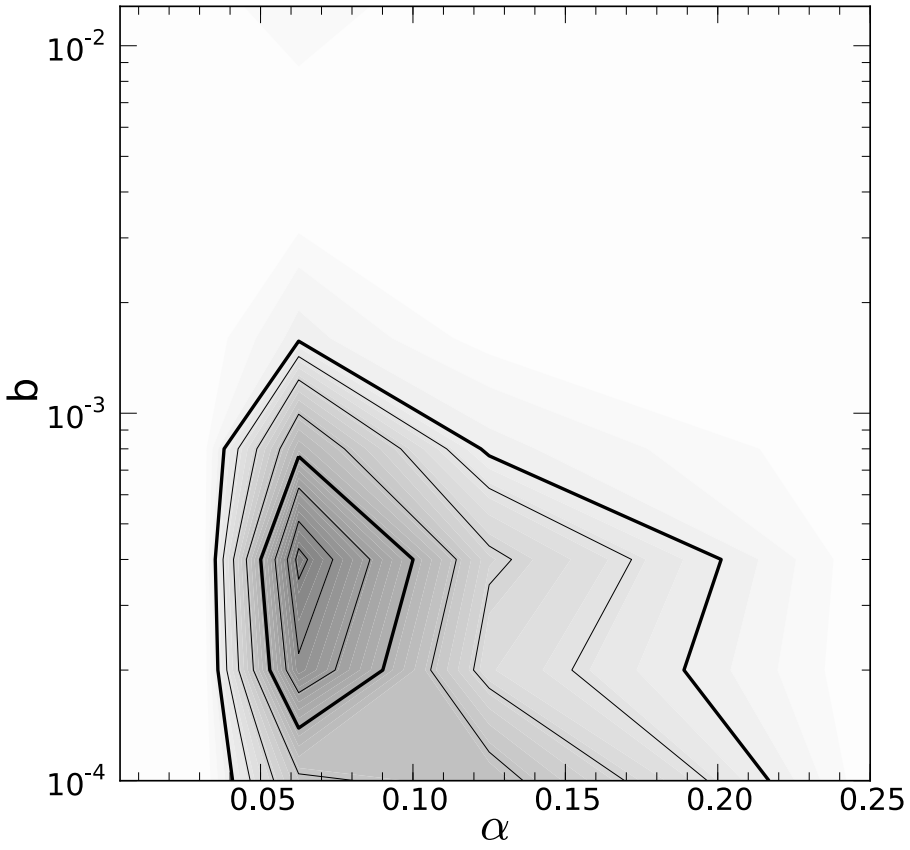

Figure 5.2 Combined probability density function for the Einstein radius b and abundance α of dark matter subhaloes in galaxies using the gravitational lens systems B 0128+437, MG 0414+0534, HE 0435-1223, B 0712+472, PG 1115+080, RXS J1131-1231, B J1422+231 and Q 2237+0305.

obtained (Table 5.3) are all roughly between 1% and 15%, or about 11% once we remove the two systems with the higher values due to suspected non-applicability of the simple smooth macromodels applied to predict the flux ratios with no millilensing. Not counting PG 1115+080, with only two images with observed fluxes and anomalies at our resolution limit in magnitues, all of these values are higher than the prediction by CDM simulations of $\alpha \sim 1\%$. Going back to Section 3.6, we can see that just by fitting a more elaborate model to the positions of the lensed images the flux anomalies and therefore the amount of substructure needed can be reduced to match the simulations. The use of only singular isothermal ellipsoids and external shear plus at most one extra singular isothermal sphere in our macromodels reduces the number of parameters and allows us to avoid including the flux ratios in the mass modeling, and therefore on the prediction of the flux ratios with no substructure, but might be causing an overestimation of the flux anomalies. It is also important to remember that our observed mid-IR fluxes for Q 2237+0305 were the latest in a series of observations with varying results that we were only comfortable using as the weighted average of all of them. A similar problem might be affecting the other systems where mid-IR fluxes were only observed in one epoch and thus giving the impression of higher anomalies in the "true" flux ratios than might actually be present. Our α values should probably only be interpreted as upper limits for the amount of substructure in each system.

If we still go ahead and combine the results for B 0128+437, MG 0414+0534, HE 0435-1223, B 0712+472, PG 1115+080, RXS J1131-1231, B J1422+231 and Q 2237+0305, the expected value of the Einstein radius that we estimate corresponds to a subhalo mass of $\sim 10^6\,\mathrm{M}_\odot$, not far from the CDM predictions, although the uncertainties are usually high. The abundance α is higher than the predictions of CDM simulations, but still marginally compatible at 2σ. As before, it must be kept in mind that for this study we assumed that the galaxies are well modelled with SIE + γ (+ SIS) profiles, and that the flux ratios are unaffected by systematics, extinction, microlensing or other perturbations. These are all factors that might lead to an overestimation of the anomalies, so the value obtained should probably be regarded as an upper limit only. Future work with more detailed mass models and a larger sample of systems will help constrain the actual values of the mass fraction that remains as satellites in the dark matter haloes of galaxies.

5.6 Caveats and future work

It must be noted that all of the results obtained in this chapter are preliminary, and more work is necessary in order to consider them final. It can be seen in Section 5.3 that the errors in the observed flux ratios are not included in the calculations. Besides hiding the true uncertainties in the final results, this can lead to an overestimation of the flux anomalies, since in the case of faint lensed images, a model prediction that is different

than the observed value but within the margin of error might be counted as a large flux anomaly when expressing the ratio in magnitudes. One way to include these errors while still considering our mathematical derivation valid would be to convolve the PDF of the individual images with their uncertainty distribution as in Eq. 5.7, before multiplying them together and integrating in Eq. 5.6.

Another issue is the source size. For this preliminary work we have assumed that the mid-IR, radio and narrow line emitting regions in the lensed sources have all a characteristic size of 1000 light-days even though this might not be true (the dusty torus could be smaller in lower luminosity AGNs, and the radio jet and NLR are generally quite larger). Given that the magnitude of the microlensing (or millilensing) effects depends on the relative sizes of the source and the Einstein radius of the distribution of lenses, the smallest millilenses will be unable to produce large anomalies on the fluxes from a large source. Failure to address this effect will assign a higher probability of reproducing the observations to a range of parameters that might not actually be able to. Also, if the source size becomes too large to allow for the use of magnification maps with a reasonable minimum number of pixels, the source size should perhaps be included as a convolution of the maps instead of using pixels with the size of the source, despite the increase on the calculation times that this would convey.

As discussed in previous sections, one of the main sources of overestimation of the anomalies is probably the use of SIE + γ (+ SIS) profiles to model the lenses, since they may not reproduce the smooth distribution of mass with the needed accuracy. However, more complicated models usually require extra constraints to avoid overfitting, and these constraints might include the flux ratios themselves. If we obtain detailed models that take the flux ratios into account but assume that the flux anomalies are only the residual differences between the predictions of these models and the observations (if there are any), we might be underestimating the impact on the fluxes caused by dark matter subhaloes, if effects like extinction and microlensing are accounted for. We could nonetheless repeat the calculations using these kinds of detailed mass models and use the results as lower limits for the abundance of substructure. This would then allow us to constrain the actual amount of subhaloes when combined with the upper limits given by the calculations using SIE + γ (+ SIS) profiles.

Finally, when using the whole sample of systems to improve the statistics of the final result, the combination of the PDFs could be performed in several different ways. Instead of just obtaining the Einstein radius of the subhaloes, that axis could be scaled in each system so that we obtain an average mass of the subhalos, or a scaled value as a function of the mass of the host halo. Instead of combined in a single estimation, the results from individual systems (once the better estimations described above have been performed) could be used to probe the abundance of subhaloes as a function of the distance to the

center of the halo, the mass of the host halo, or its redshift. All of these estimations are to be performed in future work (Vives-Arias & et al. 2016).

Chapter 6

General conclusions

In this PhD thesis we have used gravitational lens systems to study the structure of both the lensed quasars and the distribution of matter in the lens galaxies themselves. We have estimated the size and temperature profile of the accretion disk of the quasar in Q 2237+0305 as well as the minimum size of its mid-IR emitting region, and also of the radio source in the case of the radio-quiet quasars HS 0810+2554, HE 0435−1223 and RX J0911+0551. We have then tried to estimate the amount of substructure present in these systems with different methods, that will still require future work.

The different estimations for the size of the accretion disk in Q 2237+0305 at the rest wavelength $\lambda_1 = 1736$ Å are $R_{1/2} = (8.5^{+7.5}_{-4.0}, 3.4^{+5.3}_{-2.1}, 6.2^{+7.4}_{-3.4})\sqrt{\langle M \rangle / 0.3\,\mathrm{M}_\odot}$ light-days when using respectively as a baseline the mid-IR fluxes from Minezaki et al. (2009), our own measurements with GTC, and the weighted average of all mid-IR observations of the system. They are mutually consistent within the errors and larger than the prediction of ∼1 light-day given by the thin disk model based on the flux (Mosquera & Kochanek 2011). We also demonstrate that different source profiles give the same estimation for $R_{1/2}$ in this kind of microlensing studies. These results for the accretion disk size agree with previous estimations by Poindexter & Kochanek (2010a), Sluse et al. (2011), and Mosquera et al. (2013), which use different microlensing methods that do not analyze individual high magnification events (since they tend to be biased to smaller sizes). Also, our estimation is in agreement with the results from other lenses (Edelson et al. 2015; Fausnaugh et al. 2015; Morgan et al. 2010; Shappee et al. 2014), even when not using microlensing to determine the accretion disk size.

The values we obtain for the exponent p, which scales the temperature profile of the disk as $r_s(\lambda_2) = (\lambda_2/\lambda_1)^p r_s(\lambda_1)$, are all lower than the $p = 4/3$ prediction of the standard thin disk model, and therefore steeper. However, except when using a Gaussian intensity profile for the source, they are all compatible with that value at the 1σ level. More observations will be needed to determine whether there is a significant difference from the theoretical model in this aspect, but the size problem might definitely require the

presence of additional physical mechanisms to explain it.

We have also used our GTC observations of Q 2237+0305 to perform a size estimation of the mid-IR emitting region. We observe a variability in the determination of the flux ratios of the system in different mid-IR observations over the years that could be due to systematics or perhaps microlensing. If we assume it is the latter and use the weighted average of all the observations as the non-microlensed baseline, we obtain a lower limit for the source size of $R_{1/2} \gtrsim 200 \sqrt{\langle M \rangle / 0.3\,\mathrm{M}_{\odot}}$ light-days. It is very unlikely that this variability is due to microlensing of the dusty torus, because dust would not survive at that distance from an accretion disk with the luminosity of this quasar, and the time scales for the variability in such source would be in the order of decades or more, instead of years (Stalevski et al. 2012). It is possible that there is an extra mid-IR emitting component slightly larger than the optical size of the accretion disk (Sluse et al. 2013), and in this case its small size would be more affected by microlensing and would reduce the estimated size of the global mid-IR emission region when modeled as a single object.

The mid-IR flux ratios of Q 2237+0305 can also be used to test for the presence of substructure in the lens galaxy in the form of dark matter subhaloes as predicted by CDM simulations. Through simple smooth models for the mass distribution of the lens galaxy (SIE + γ and NFW + de Vaucouleurs + γ), we calculate the effects of different abundances of subhaloes of different sizes to see in which cases they would best reproduce the weighted average of the mid-IR fluxes for the system. As expected for this method, we cannot constrain the size of the individual subhaloes, but we obtain abundances of $\alpha = 0.033^{+0.046}_{-0.019}$ for the SIE + γ model and $\alpha = 0.013^{+0.019}_{-0.008}$ for the NFW + de Vaucouleurs + γ. These abundances are expressed as the fraction of the surface mass density that remain in subhaloes, and are close to the value of $\sim 1\%$ predicted for the central regions of dark matter haloes. The fact that the accurate mid-IR flux ratios were hard to fit with smooth models without reaching solutions with ellipticities for the dark matter halo that were too high to be physical, but were easily reproduced with a modest amount of dark matter substructure, hints to the actual presence of these subhaloes.

We then try to increase the sample of gravitational lens systems that have flux ratios measured in radio by observing systems with radio-quiet quasars, that should nonetheless present faint radio emission at some level. We achieve detections for all four of our targets, HS 0810+2554, HE 0435−1223, RX J0911+0551 and SDSS J0924+0219, and a sufficient signal-to-noise ratio to measure the flux ratios in the first three. We find, however, that the best explanation for any flux anomalies in these sources when compared to the predictions of smooth models is that the source is extended, with no need to invoke dark matter substructure.

These radio observations also allow us to gather some information regarding the emis-

sion mechanisms of radio-quiet quasars. The extended size of the sources, of the order of 70 pc in HS 0810+2554 and up to ∼1 kpc in HE 0435−1223 and RX J0911+0551, do not support the hypotheses of free-free emission from a disk wind (Blundell & Kuncic 2007) or emission from magnetically-heated coronae (Laor & Behar 2008), since the source sizes in that case would be about 1 pc or smaller. We also get spectral indices of -0.55 ± 0.1 for HS 0810+2554 and a lower limit of -0.5 for RX J0911+0551, and their steepness is consistent both with star formation in the quasar host galaxy and with a smaller version of the relativistic jets that produce the radio emission in radio-loud quasars. If the emission mechanism is star formation, however, we would expect it to be extended over most of the galaxy and therefore have a characteristic size of 5-10 kpc, so perhaps with further observations of more systems this possibility could be excluded.

Finally, we have compiled a sample of quadruply imaged quasars that have flux ratios measured in the literature at optical and near-IR narrow spectral lines and mid-IR and radio wavelengths, that should be unaffected by microlensing or extinction effects and therefore be close to the "true" flux ratios caused by the mass distribution in the lens galaxy. We develop a procedure to estimate the size and abundance of dark matter subhaloes that would be needed to reproduce the observed flux ratios in the systems, assuming that the predictions given by smooth mass models for the lenses are accurate, and that the fluxes are not affected by any other phenomenon unaccounted for. After excluding the most problematic systems we arrive to a preliminary estimation of $\sim 10^6\,\mathrm{M}_\odot$ for the average subhalo mass and an abundance $\alpha = 0.075^{+0.030}_{-0.021}$. The value of the abundance is high when compared to CDM predictions, but still marginally compatible at 2σ. This is most likely due to the use of oversimplified mass models and inaccurate assumptions about the source sizes that will be the focus of future work.

In the coming years, new facilities and observatories will make it possible to continue and expand the type of studies described in this thesis. The Large Synoptic Survey Telescope (LSST), by photographing the entire available sky every few nights and in six different filters, will discover thousands of new gravitational lens systems that will be monitored regularly (Ivezic et al. 2008; Marshall et al. 2010). The study of the microlensing detections in such a large sample of quasar images will become instrumental in determining the size and temperature profile of their accretion disks and therefore provide huge improvements in our knowledge of the physics of this process. The size of the accretion disks could be also correlated with the mass of their central supermassive black holes with greater statistical power as an additional constraint to test the physical models for the disk. New mid-IR instruments in ground-based facilities like NOMIC at the Large Binocular Telescope Interferometer (LBTI) will allow to obtain flux ratios in more systems at these wavelengths (Hoffmann et al. 2014), and the Mid-Infrared Instrument (MIDI) at the space-based James Webb Space Telescope (JWST) could complement these observations without atmospheric interference, although at slightly lower resolutions (Bouchet et al.

2015). In radio wavelengths, there are high expectations for the Square Kilometre Array (SKA), which will be able to perform routine observations with more sensitivity and the sub-arcsecond resolutions required to obtain the flux ratios between the multiple images in gravitational lens systems. These measurements, aside from the insights they will provide into the structure of the dusty tori and radio emitting regions of quasars, will greatly increase the sample of quadruply imaged quasars with anomalous fluxes that can be used to explore the substructure in the mass distribution in lens galaxies. Therefore, they will bring us closer to the solution for the missing satellites problem in the Cold Dark Matter paradigm.

References

Agol, E., Jones, B. & Blaes, O. (2000). Keck Mid-Infrared Imaging of QSO 2237+0305. *ApJ*, **545**, 657–663. xiv, xv, 27, 30, 41, 44, 49, 51

Agol, E., Wyithe, S., Jones, B. & Fluke, C. (2001). Mid-Infrared Imaging of the Einstein Cross QSO. *PASA*, **18**, 166–168. xiv, xv, 41, 44, 49, 51

Agol, E., Gogarten, S.M., Gorjian, V. & Kimball, A. (2009). Spitzer Observations of a Gravitationally Lensed Quasar, QSO 2237+0305. *ApJ*, **697**, 1010–1019. xiv, xv, 26, 41, 44, 49, 50, 51

Akerib, D.S., Alsum, S., Araújo, H.M., Bai, X., Bailey, A.J., Balajthy, J., Beltrame, P., Bernard, E.P., Bernstein, A., Biesiadzinski, T.P., Boulton, E.M., Bramante, R., Brás, P., Byram, D., Cahn, S.B., Carmona-Benitez, M.C., Chan, C., Chiller, A.A., Chiller, C., Currie, A., Cutter, J.E., Davison, T.J.R., Dobi, A., Dobson, J.E.Y., Druszkiewicz, E., Edwards, B.N., Faham, C.H., Fiorucci, S., Gaitskell, R.J., Gehman, V.M., Ghag, C., Gibson, K.R., Gilchriese, M.G.D., Hall, C.R., Hanhardt, M., Haselschwardt, S.J., Hertel, S.A., Hogan, D.P., Horn, M., Huang, D.Q., Ignarra, C.M., Ihm, M., Jacobsen, R.G., Ji, W., Kamdin, K., Kazkaz, K., Khaitan, D., Knoche, R., Larsen, N.A., Lee, C., Lenardo, B.G., Lesko, K.T., Lindote, A., Lopes, M.I., Manalaysay, A., Mannino, R.L., Marzioni, M.F., McKinsey, D.N., Mei, D.M., Mock, J., Moongweluwan, M., Morad, J.A., Murphy, A.S.J., Nehrkorn, C., Nelson, H.N., Neves, F., O'Sullivan, K., Oliver-Mallory, K.C., Palladino, K.J., Pease, E.K., Phelps, P., Reichhart, L., Rhyne, C., Shaw, S., Shutt, T.A., Silva, C., Solmaz, M., Solovov, V.N., Sorensen, P., Stephenson, S., Sumner, T.J., Szydagis, M., Taylor, D.J., Taylor, W.C., Tennyson, B.P., Terman, P.A., Tiedt, D.R., To, W.H., Tripathi, M., Tvrznikova, L., Uvarov, S., Verbus, J.R., Webb, R.C., White, J.T., Whitis, T.J., Witherell, M.S., Wolfs, F.L.H., Xu, J., Yazdani, K., Young, S.K. & Zhang, C. (2016). Results from a search for dark matter in the complete LUX exposure. *ArXiv e-prints*. 21

Alcock, C., Allsman, R.A., Alves, D.R., Axelrod, T.S., Becker, A.C., Bennett, D.P., Cook, K.H., Dalal, N., Drake, A.J., Freeman, K.C., Geha, M., Griest, K., Lehner, M.J., Marshall, S.L., Minniti, D., Nelson, C.A., Peterson, B.A., Popowski, P., Pratt, M.R., Quinn, P.J., Stubbs, C.W., Sutherland, W., Tomaney, A.B., Vandehei, T. & Welch, D. (2000). The MACHO Project: Microlensing Results from 5.7 Years of Large Magellanic Cloud Observations. *ApJ*, **542**, 281–307. 20

Alcock, C., Allsman, R.A., Alves, D.R., Axelrod, T.S., Becker, A.C., Bennett, D.P., Cook, K.H., Drake, A.J., Freeman, K.C., Geha, M., Griest, K., Lehner, M.J., Marshall, S.L., Minniti, D., Nelson, C.A., Peterson, B.A., Popowski, P., Pratt, M.R., Quinn, P.J., Stubbs, C.W., Sutherland, W., Tomaney, A.B., Vandehei, T. & Welch, D. (2001). The MACHO Project: Microlensing Detection Efficiency. *ApJS*, **136**, 439–462. 20

Amara, A., Metcalf, R.B., Cox, T.J. & Ostriker, J.P. (2006). Simulations of strong gravitational lensing with substructure. *MNRAS*, **367**, 1367–1378. 23, 60, 86, 90

Anguita, T., Schmidt, R.W., Turner, E.L., Wambsganss, J., Webster, R.L., Loomis, K.A., Long, D. & McMillan, R. (2008). The multiple quasar Q2237+0305 under a microlensing caustic. *A&A*, **480**, 327–334. 27, 34

Anguita, T., Faure, C., Kneib, J.P., Wambsganss, J., Knobel, C., Koekemoer, A.M. & Limousin, M. (2009). COSMOS 5921+0638: characterization and analysis of a new strong gravitationally lensed AGN. *A&A*, **507**, 35–46. xvii, 85

Antonucci, R. (1993). Unified models for active galactic nuclei and quasars. *ARA&A*, **31**, 473–521. 14

Argo, M. (2014). e-MERLIN data reduction pipeline. Astrophysics Source Code Library. 68

Assef, R.J., Denney, K.D., Kochanek, C.S., Peterson, B.M., Kozłowski, S., Ageorges, N., Barrows, R.S., Buschkamp, P., Dietrich, M., Falco, E., Feiz, C., Gemperlein, H., Germeroth, A., Grier, C.J., Hofmann, R., Juette, M., Khan, R., Kilic, M., Knierim, V., Laun, W., Lederer, R., Lehmitz, M., Lenzen, R., Mall, U., Madsen, K.K., Mandel, H., Martini, P., Mathur, S., Mogren, K., Mueller, P., Naranjo, V., Pasquali, A., Polsterer, K., Pogge, R.W., Quirrenbach, A., Seifert, W., Stern, D., Shappee, B., Storz, C., Van Saders, J., Weiser, P. & Zhang, D. (2011). Black Hole Mass Estimates Based on C IV are Consistent with Those Based on the Balmer Lines. *ApJ*, **742**, 93. xvii, 26, 34, 70, 85

Baars, J.W.M., Genzel, R., Pauliny-Toth, I.I.K. & Witzel, A. (1977). The absolute spectrum of CAS A - an accurate flux density scale and a set of secondary calibrators. *A&A*, **61**, 99–106. 67

Bade, N., Siebert, J., Lopez, S., Voges, W. & Reimers, D. (1997). RX J0911.4+0551: A new multiple QSO selected from the ROSAT All-Sky Survey. *A&A*, **317**, L13–L16. xix, 66, 78

Bartelmann, M. (2010). TOPICAL REVIEW Gravitational lensing. *Classical and Quantum Gravity*, **27**, 233001. 58

Barvainis, R. (1987). Hot dust and the near-infrared bump in the continuum spectra of quasars and active galactic nuclei. *ApJ*, **320**, 537–544. 40

Barvainis, R., Lehár, J., Birkinshaw, M., Falcke, H. & Blundell, K.M. (2005). Radio Variability of Radio-quiet and Radio-loud Quasars. *ApJ*, **618**, 108–122. 59, 87

Bate, N.F., Floyd, D.J.E., Webster, R.L. & Wyithe, J.S.B. (2008). A microlensing study of the accretion disc in the quasar MG 0414+0534. *MNRAS*, **391**, 1955–1960. 27

Becker, R.H., White, R.L. & Helfand, D.J. (1995). The FIRST Survey: Faint Images of the Radio Sky at Twenty Centimeters. *ApJ*, **450**, 559. 58, 66

Belokurov, V., Zucker, D.B., Evans, N.W., Wilkinson, M.I., Irwin, M.J., Hodgkin, S., Bramich, D.M., Irwin, J.M., Gilmore, G., Willman, B., Vidrih, S., Newberg, H.J., Wyse, R.F.G., Fellhauer, M., Hewett, P.C., Cole, N., Bell, E.F., Beers, T.C., Rockosi, C.M., Yanny, B., Grebel, E.K., Schneider, D.P., Lupton, R., Barentine, J.C., Brewington, H., Brinkmann, J., Harvanek, M., Kleinman, S.J., Krzesinski, J., Long, D., Nitta, A., Smith, J.A. & Snedden, S.A. (2006). A Faint New Milky Way Satellite in Bootes. *ApJ*, **647**, L111–L114. 21, 41, 60

Benson, A.J., Frenk, C.S., Lacey, C.G., Baugh, C.M. & Cole, S. (2002). The effects of photoionization on galaxy formation - II. Satellite galaxies in the Local Group. *MNRAS*, **333**, 177–190. 21

Biggs, A.D., Browne, I.W.A., Jackson, N.J., York, T., Norbury, M.A., McKean, J.P. & Phillips, P.M. (2004). Radio, optical and infrared observations of CLASS B0128+437. *MNRAS*, **350**, 949–961. 59

Blackburne, J.A., Pooley, D., Rappaport, S. & Schechter, P.L. (2011). Sizes and Temperature Profiles of Quasar Accretion Disks from Chromatic Microlensing. *ApJ*, **729**, 34. 27, 34, 59

Blackburne, J.A., Kochanek, C.S., Chen, B., Dai, X. & Chartas, G. (2014). The Optical, Ultraviolet, and X-Ray Structure of the Quasar HE 0435-1223. *ApJ*, **789**, 125. 27

Blackburne, J.A., Kochanek, C.S., Chen, B., Dai, X. & Chartas, G. (2015). The Structure of HE 1104-1805 from Infrared to X-Ray. *ApJ*, **798**, 95. 27

Blundell, K.M. & Beasley, A.J. (1998). The central engines of radio-quiet quasars. *MNRAS*, **299**, 165–170. 59

Blundell, K.M. & Kuncic, Z. (2007). On the Origin of Radio Core Emission in Radio-quiet Quasars. *ApJ*, **668**, L103–L106. 59, 84, 107

Bouchet, P., García-Marín, M., Lagage, P.O., Amiaux, J., Auguéres, J.L., Bauwens, E., Blommaert, J.A.D.L., Chen, C.H., Detre, Ö.H., Dicken, D., Dubreuil, D., Galdemard, P., Gastaud, R., Glasse, A., Gordon, K.D., Gougnaud, F., Guillard, P., Justtanont, K., Krause, O., Leboeuf, D., Longval, Y., Martin, L., Mazy, E., Moreau, V., Olofsson, G., Ray, T.P., Rees, J.M., Renotte, E., Ressler, M.E., Ronayette, S., Salasca, S., Scheithauer, S., Sykes, J., Thelen, M.P., Wells, M., Wright, D. & Wright, G.S. (2015). The Mid-Infrared Instrument for the James Webb Space Telescope, III: MIRIM, The MIRI Imager. *PASP*, **127**, 612–622. 107

Bovill, M.S. & Ricotti, M. (2009). Pre-Reionization Fossils, Ultra-Faint Dwarfs, and the Missing Galactic Satellite Problem. *ApJ*, **693**, 1859–1870. 21

Bradač, M., Schneider, P., Lombardi, M., Steinmetz, M., Koopmans, L.V.E. & Navarro, J.F. (2004). The signature of substructure on gravitational lensing in the ΛCDM cosmological model. *A&A*, **423**, 797–809. 23, 60, 90

Braibant, L., Hutsemékers, D., Sluse, D., Anguita, T. & García-Vergara, C.J. (2014). Microlensing of the broad-line region in the quadruply imaged quasar HE0435-1223. *A&A*, **565**, L11. 74

Browne, I.W.A., Wilkinson, P.N., Jackson, N.J.F., Myers, S.T., Fassnacht, C.D., Koopmans, L.V.E., Marlow, D.R., Norbury, M., Rusin, D., Sykes, C.M., Biggs, A.D., Blandford, R.D., de Bruyn, A.G., Chae, K.H., Helbig, P., King, L.J., McKean, J.P., Pearson, T.J., Phillips, P.M., Readhead, A.C.S., Xanthopoulos, E. & York, T. (2003). The Cosmic Lens All-Sky Survey - II. Gravitational lens candidate selection and follow-up. *MNRAS*, **341**, 13–32. 58

Bullock, J.S., Kravtsov, A.V. & Weinberg, D.H. (2000). Reionization and the Abundance of Galactic Satellites. *ApJ*, **539**, 517–521. 21

Burtscher, L., Meisenheimer, K., Tristram, K.R.W., Jaffe, W., Hönig, S.F., Davies, R.I., Kishimoto, M., Pott, J.U., Röttgering, H., Schartmann, M., Weigelt, G. & Wolf, S. (2013). A diversity of dusty AGN tori. Data release for the VLTI/MIDI AGN Large Program and first results for 23 galaxies. *A&A*, **558**, A149. 17, 50

Burud, I., Courbin, F., Lidman, C., Jaunsen, A.O., Hjorth, J., Østensen, R., Andersen, M.I., Clasen, J.W., Wucknitz, O., Meylan, G., Magain, P., Stabell, R. & Refsdal, S. (1998). High-Resolution Optical and Near-Infrared Imaging of the Quadruple Quasar RX J0911.4+0551. *ApJ*, **501**, L5–L10. xvii, xix, 66, 81, 83, 85

Burud, I., Courbin, F., Magain, P., Lidman, C., Hutsemékers, D., Kneib, J.P., Hjorth, J., Brewer, J., Pompei, E., Germany, L., Pritchard, J., Jaunsen, A.O., Letawe, G. & Meylan, G. (2002). An optical time-delay for the lensed BAL quasar HE 2149-2745. *A&A*, **383**, 71–81. 59

Chang, K. & Refsdal, S. (1979). Flux variations of QSO 0957+561 A, B and image splitting by stars near the light path. *Nature*, **282**, 561–564. 27

Chang, K. & Refsdal, S. (1984). Star disturbances in gravitational lens galaxies. *A&A*, **132**, 168–178. 27

Chartas, G., Hamann, F., Eracleous, M., Misawa, T., Cappi, M., Giustini, M., Charlton, J.C. & Marvin, M. (2014). Magnified Views of the Ultrafast Outflow of the z = 1.51 Active Galactic Nucleus HS 0810+2554. *ApJ*, **783**, 57. 70

Chen, H.W., Gauthier, J.R., Sharon, K., Johnson, S.D., Nair, P. & Liang, C.J. (2014). Spatially resolved velocity maps of halo gas around two intermediate-redshift galaxies. *MNRAS*, **438**, 1435–1450. 75

Chen, J., Koushiappas, S.M. & Zentner, A.R. (2011). The Effects of Halo-to-halo Variation on Substructure Lensing. *ApJ*, **741**, 117. 23, 90

Chiba, M., Minezaki, T., Kashikawa, N., Kataza, H. & Inoue, K.T. (2005). Subaru Mid-Infrared Imaging of the Quadruple Lenses PG 1115+080 and B1422+231: Limits on Substructure Lensing. *ApJ*, **627**, 53–61. 41, 60, 92

Clowe, D., Bradač, M., Gonzalez, A.H., Markevitch, M., Randall, S.W., Jones, C. & Zaritsky, D. (2006). A Direct Empirical Proof of the Existence of Dark Matter. *ApJ*, **648**, L109–L113. 20

Condon, J.J., Cotton, W.D., Greisen, E.W., Yin, Q.F., Perley, R.A., Taylor, G.B. & Broderick, J.J. (1998). The NRAO VLA Sky Survey. *AJ*, **115**, 1693–1716. 66

REFERENCES

Condon, J.J., Kellermann, K.I., Kimball, A.E., Ivezić, Ž. & Perley, R.A. (2013). Active Galactic Nucleus and Starburst Radio Emission from Optically Selected Quasi-stellar Objects. *ApJ*, **768**, 37. 59, 83, 84

Congdon, A.B., Keeton, C.R. & Nordgren, C.E. (2008). Analytic relations for magnifications and time delays in gravitational lenses with fold and cusp configurations. *MNRAS*, **389**, 398–406. 60

Cooper, A.P., Cole, S., Frenk, C.S., White, S.D.M., Helly, J., Benson, A.J., De Lucia, G., Helmi, A., Jenkins, A., Navarro, J.F., Springel, V. & Wang, J. (2010). Galactic stellar haloes in the CDM model. *MNRAS*, **406**, 744–766. 21

Cornwell, T.J. & Wilkinson, P.N. (1981). A new method for making maps with unstable radio interferometers. *MNRAS*, **196**, 1067–1086. 65

Corrigan, R.T., Irwin, M.J., Arnaud, J., Fahlman, G.G., Fletcher, J.M., Hewett, P.C., Hewitt, J.N., Le Fevre, O., McClure, R., Pritchet, C.J., Schneider, D.P., Turner, E.L., Webster, R.L. & Yee, H.K.C. (1991). Initial light curve of Q2237 + 0305. *AJ*, **102**, 34–40. 26

Courbin, F., Saha, P. & Schechter, P.L. (2002). Quasar Lensing. In F. Courbin & D. Minniti, eds., *Gravitational Lensing: An Astrophysical Tool*, vol. 608 of *Lecture Notes in Physics, Berlin Springer Verlag*, 1. 58

Courbin, F., Chantry, V., Revaz, Y., Sluse, D., Faure, C., Tewes, M., Eulaers, E., Koleva, M., Asfandiyarov, I., Dye, S., Magain, P., van Winckel, H., Coles, J., Saha, P., Ibrahimov, M. & Meylan, G. (2011). COSMOGRAIL: the COSmological MOnitoring of GRAvItational Lenses. IX. Time delays, lens dynamics and baryonic fraction in HE 0435-1223. *A&A*, **536**, A53. 74, 75, 87

Dai, X., Chartas, G., Agol, E., Bautz, M.W. & Garmire, G.P. (2003). Chandra Observations of QSO 2237+0305. *ApJ*, **589**, 100–110. 26

Dai, X., Kochanek, C.S., Chartas, G., Kozłowski, S., Morgan, C.W., Garmire, G. & Agol, E. (2010). The Sizes of the X-ray and Optical Emission Regions of RXJ 1131-1231. *ApJ*, **709**, 278–285. 27

Dalal, N. & Kochanek, C.S. (2002). Direct Detection of Cold Dark Matter Substructure. *ApJ*, **572**, 25–33. 23, 41, 52, 54, 60, 86, 90, 95

De Lucia, G., Kauffmann, G., Springel, V., White, S.D.M., Lanzoni, B., Stoehr, F., Tormen, G. & Yoshida, N. (2004). Substructures in cold dark matter haloes. *MNRAS*, **348**, 333–344. 23

Dobler, G. & Keeton, C.R. (2006). Finite source effects in strong lensing: implications for the substructure mass scale. *MNRAS*, **365**, 1243–1262. 23, 90

Dye, S. & Warren, S.J. (2005). Decomposition of the Visible and Dark Matter in the Einstein Ring 0047-2808 by Semilinear Inversion. *ApJ*, **623**, 31–41. 61

Edelson, R., Gelbord, J.M., Horne, K., McHardy, I.M., Peterson, B.M., Arévalo, P., Breeveld, A.A., De Rosa, G., Evans, P.A., Goad, M.R., Kriss, G.A., Brandt, W.N., Gehrels, N., Grupe, D., Kennea, J.A., Kochanek, C.S., Nousek, J.A., Papadakis, I., Siegel, M., Starkey, D., Uttley, P., Vaughan, S., Young, S., Barth, A.J., Bentz, M.C., Brewer, B.J., Crenshaw, D.M., Dalla Bontà, E., De Lorenzo-Cáceres, A., Denney, K.D., Dietrich, M., Ely, J., Fausnaugh, M.M., Grier, C.J., Hall, P.B., Kaastra, J., Kelly, B.C., Korista, K.T., Lira, P., Mathur, S., Netzer, H., Pancoast, A., Pei, L., Pogge, R.W., Schimoia, J.S., Treu, T., Vestergaard, M., Villforth, C., Yan, H. & Zu, Y. (2015). Space Telescope and Optical Reverberation Mapping Project. II. Swift and HST Reverberation Mapping of the Accretion Disk of NGC 5548. *ApJ*, **806**, 129. 27, 37, 105

Eigenbrod, A., Courbin, F., Dye, S., Meylan, G., Sluse, D., Vuissoz, C. & Magain, P. (2006). COSMOGRAIL: the COSmological MOnitoring of GRAvItational Lenses. II. SDSS J0924+0219: the redshift of the lensing galaxy, the quasar spectral variability and the Einstein rings. *A&A*, **451**, 747–757. xix, 66

Eigenbrod, A., Courbin, F., Meylan, G., Agol, E., Anguita, T., Schmidt, R.W. & Wambsganss, J. (2008). Microlensing variability in the gravitationally lensed quasar QSO 2237+0305 ≡ the Einstein Cross. II. Energy profile of the accretion disk. *A&A*, **490**, 933–943. xiv, 27, 34, 36

Einstein, A. (1911). Über den Einfluß der Schwerkraft auf die Ausbreitung des Lichtes. *Annalen der Physik*, **340**, 898–908. 2

Einstein, A. (1915). Erklärung der Perihelbewegung des Merkur aus der allgemeinen Relativitätstheorie. *Sitzungsberichte der Königlich Preußischen Akademie der Wissenschaften (Berlin), Seite 831-839.*. 2

Elíasdóttir, Á., Hjorth, J., Toft, S., Burud, I. & Paraficz, D. (2006). Extinction Curves of Lensing Galaxies out to z = 1. *ApJS*, **166**, 443–469. 40, 60

Fadely, R. & Keeton, C.R. (2011). Near-infrared K and L' Flux Ratios in Six Lensed Quasars. *AJ*, **141**, 101. 60

Fadely, R. & Keeton, C.R. (2012). Substructure in the lens HE 0435-1223. *MNRAS*, **419**, 936–951. 60, 74, 75, 76

Falco, E.E., Lehar, J., Perley, R.A., Wambsganss, J. & Gorenstein, M.V. (1996). VLA Observations of the Gravitational Lens System Q2237+0305. *AJ*, **112**, 897. xv, 50, 51, 92

Falco, E.E., Impey, C.D., Kochanek, C.S., Lehár, J., McLeod, B.A., Rix, H.W., Keeton, C.R., Muñoz, J.A. & Peng, C.Y. (1999). Dust and Extinction Curves in Galaxies with z0: The Interstellar Medium of Gravitational Lens Galaxies. *ApJ*, **523**, 617–632. 28, 40, 60

Fassnacht, C.D., Blandford, R.D., Cohen, J.G., Matthews, K., Pearson, T.J., Readhead, A.C.S., Womble, D.S., Myers, S.T., Browne, I.W.A., Jackson, N.J., Marlow, D.R., Wilkinson, P.N., Koopmans, L.V.E., de Bruyn, A.G., Schilizzi, R.T., Bremer, M. & Miley, G. (1999a). B2045+265: A New Four-Image Gravitational Lens from CLASS. *AJ*, **117**, 658–670. 60

Fassnacht, C.D., Pearson, T.J., Readhead, A.C.S., Browne, I.W.A., Koopmans, L.V.E., Myers, S.T. & Wilkinson, P.N. (1999b). A Determination of H_0 with the CLASS Gravitational Lens B1608+656. I. Time Delay Measurements with the VLA. *ApJ*, **527**, 498–512. 92

Faure, C., Kneib, J.P., Covone, G., Tasca, L., Leauthaud, A., Capak, P., Jahnke, K., Smolcic, V., de la Torre, S., Ellis, R., Finoguenov, A., Koekemoer, A., Le Fevre, O., Massey, R., Mellier, Y., Refregier, A., Rhodes, J., Scoville, N., Schinnerer, E., Taylor, J., Van Waerbeke, L. & Walcher, J. (2008). First Catalog of Strong Lens Candidates in the COSMOS Field. *ApJS*, **176**, 19–38. 84

Faure, C., Sluse, D., Cantale, N., Tewes, M., Courbin, F., Durrer, P. & Meylan, G. (2011). VLT adaptive optics search for luminous substructures in the lens galaxy towards SDSS J0924+0219. *A&A*, **536**, A29. 81

Fausnaugh, M.M., Denney, K.D., Barth, A.J., Bentz, M.C., Bottorff, M.C., Carini, M.T., Croxall, K.V., De Rosa, G., Goad, M.R., Horne, K., Joner, M.D., Kaspi, S., Kim, M., Klimanov, S.A., Kochanek, C.S., Leonard, D.C., Netzer, H., Peterson, B.M., Schnulle, K., Sergeev, S.G., Vestergaard, M., Zheng, W.K., Anderson, M.D., Arevalo, P., Bazhaw, C., Borman, G.A., Boroson, T.A., Brandt, W.N., Breeveld, A.A., Brewer, B.J., Cackett, E.M., Crenshaw, D.M., Dalla Bonta, E., De Lorenzo-Caceres, A., Dietrich, M., Edelson, R., Efimova, N.V., Ely, J., Evans, P.A., Filippenko, A.V., Flatland, K., Gehrels, N., Geier, S., Gelbord, J.M., Gonzalez, L., Gorjian, V., Grier, C.J., Grupe, D., Hall, P.B., Hicks, S., Horenstein, D., Hutchison, T., Im, M., Jensen, J.J., Jones, J., Kaastra, J., Kelly, B.C., Kennea, J.A., Kim, S.C., Korista, K.T., Kriss, G.A., Larionov, V.M., Lee,

J.C., Lira, P., MacInnis, F., Manne-Nicholas, E.R., Mathur, S., McHardy, I.M., Montouri, C., Musso, R., Nazarov, S.V., Norris, R.P., Nousek, J.A., Okhmat, D.N., Pancoast, A., Papadakis, I., Parks, J.R., Pei, L., Pogge, R.W., Pott, J.U., Rafter, S.E., Rix, H.W., Saylor, D.A., Schimoia, J.S., Siegel, M., Spencer, M., Starkey, D., Sung, H.I., Teems, K.G., Treu, T., Turner, C.S., Uttley, P., Villforth, C., Weiss, Y., Woo, J.H., Yan, H., Young, S. & Zu, Y. (2015). Space Telescope and Optical Reverberation Mapping Project. III. Optical Continuum Emission and Broad-Band Time Delays in NGC 5548. *ArXiv e-prints*. 27, 37, 105

Floyd, D.J.E., Bate, N.F. & Webster, R.L. (2009). The accretion disc in the quasar SDSS J0924+0219. *MNRAS*, **398**, 233–239. 27, 81

Font, A.S., Benson, A.J., Bower, R.G., Frenk, C.S., Cooper, A., De Lucia, G., Helly, J.C., Helmi, A., Li, Y.S., McCarthy, I.G., Navarro, J.F., Springel, V., Starkenburg, E., Wang, J. & White, S.D.M. (2011). The population of Milky Way satellites in the Λ cold dark matter cosmology. *MNRAS*, **417**, 1260–1279. 21

Foreman-Mackey, D., Hogg, D.W., Lang, D. & Goodman, J. (2013). emcee: The MCMC Hammer. *PASP*, **125**, 306–312. 72

Gao, L., White, S.D.M., Jenkins, A., Stoehr, F. & Springel, V. (2004). The subhalo populations of ΛCDM dark haloes. *MNRAS*, **355**, 819–834. 23

Ghosh, K.K. & Narasimha, D. (2009). A Quasi-Stellar Object Plus Host System Lensed into a 6" Einstein Ring by a Low-Redshift Galaxy. *ApJ*, **692**, 694–701. xvii, 85

Greenstein, J.L. & Matthews, T.A. (1963). Redshift of the Radio Source 3C 48. *AJ*, **68**, 279. 13

Greenstein, J.L. & Schmidt, M. (1964). The Quasi-Stellar Radio Sources 3c 48 and 3c 273. *ApJ*, **140**, 1. 13

Guo, Q., White, S., Boylan-Kolchin, M., De Lucia, G., Kauffmann, G., Lemson, G., Li, C., Springel, V. & Weinmann, S. (2011). From dwarf spheroidals to cD galaxies: simulating the galaxy population in a ΛCDM cosmology. *MNRAS*, **413**, 101–131. 21

Hainline, L.J., Morgan, C.W., MacLeod, C.L., Landaal, Z.D., Kochanek, C.S., Harris, H.C., Tilleman, T., Goicoechea, L.J., Shalyapin, V.N. & Falco, E.E. (2013). Time Delay and Accretion Disk Size Measurements in the Lensed Quasar SBS 0909+532 from Multiwavelength Microlensing Analysis. *ApJ*, **774**, 69. 27

Hawkins, M.R.S. (2015). A new look at microlensing limits on dark matter in the Galactic halo. *A&A*, **575**, A107. 20

Hazard, C., Mackey, M.B. & Shimmins, A.J. (1963). Investigation of the Radio Source 3C 273 By The Method of Lunar Occultations. *Nature*, **197**, 1037–1039. 13

Hewitt, J.N., Turner, E.L., Schneider, D.P., Burke, B.F. & Langston, G.I. (1988). Unusual radio source MG1131+0456 - A possible Einstein ring. *Nature*, **333**, 537–540. 58

Hewitt, J.N., Turner, E.L., Lawrence, C.R., Schneider, D.P. & Brody, J.P. (1992). A gravitational lens candidate with an unusually red optical counterpart. *AJ*, **104**, 968–979. 58

Hezaveh, Y.D., Marrone, D.P., Fassnacht, C.D., Spilker, J.S., Vieira, J.D., Aguirre, J.E., Aird, K.A., Aravena, M., Ashby, M.L.N., Bayliss, M., Benson, B.A., Bleem, L.E., Bothwell, M., Brodwin, M., Carlstrom, J.E., Chang, C.L., Chapman, S.C., Crawford, T.M., Crites, A.T., De Breuck, C., de Haan, T., Dobbs, M.A., Fomalont, E.B., George, E.M., Gladders, M.D., Gonzalez, A.H., Greve, T.R., Halverson, N.W., High, F.W., Holder, G.P., Holzapfel, W.L., Hoover, S., Hrubes, J.D., Husband, K., Hunter, T.R., Keisler, R., Lee, A.T., Leitch, E.M., Lueker, M., Luong-Van, D., Malkan, M., McIntyre, V., McMahon, J.J., Mehl, J., Menten, K.M., Meyer, S.S., Mocanu, L.M., Murphy, E.J., Natoli, T., Padin, S., Plagge, T., Reichardt, C.L., Rest, A., Ruel, J., Ruhl, J.E., Sharon, K., Schaffer, K.K., Shaw, L., Shirokoff, E., Stalder, B., Staniszewski, Z., Stark, A.A., Story, K., Vanderlinde, K., Weiss, A., Welikala, N. & Williamson, R. (2013). ALMA Observations of SPT-discovered, Strongly Lensed, Dusty, Star-forming Galaxies. *ApJ*, **767**, 132. 61, 69

Hoffmann, W.F., Hinz, P.M., Defrère, D., Leisenring, J.M., Skemer, A.J., Arbo, P.A., Montoya, M. & Mennesson, B. (2014). Operation and performance of the mid-infrared camera, NOMIC, on the Large Binocular Telescope. In *Ground-based and Airborne Instrumentation for Astronomy V*, vol. 9147 of *Proc. SPIE*, 91471O. 107

Högbom, J.A. (1974). Aperture Synthesis with a Non-Regular Distribution of Interferometer Baselines. *A&AS*, **15**, 417. 64

Hönig, S.F., Kishimoto, M., Tristram, K.R.W., Prieto, M.A., Gandhi, P., Asmus, D., Antonucci, R., Burtscher, L., Duschl, W.J. & Weigelt, G. (2013). Dust in the Polar Region as a Major Contributor to the Infrared Emission of Active Galactic Nuclei. *ApJ*, **771**, 87. 15

Huchra, J., Gorenstein, M., Kent, S., Shapiro, I., Smith, G., Horine, E. & Perley, R. (1985). 2237 + 0305: A new and unusual gravitational lens. *AJ*, **90**, 691–696. 25

Impey, C.D., Foltz, C.B., Petry, C.E., Browne, I.W.A. & Patnaik, A.R. (1996). Hubble Space Telescope Observations of the Gravitational Lens System B1422+231. *ApJ*, **462**, L53. 92

Inada, N., Becker, R.H., Burles, S., Castander, F.J., Eisenstein, D., Hall, P.B., Johnston, D.E., Pindor, B., Richards, G.T., Schechter, P.L., Sekiguchi, M., White, R.L., Brinkmann, J., Frieman, J.A., Kleinman, S.J., Krzesiński, J., Long, D.C., Neilsen, E.H., Jr., Newman, P.R., Nitta, A., Schneider, D.P., Snedden, S. & York, D.G. (2003a). SDSS J092455.87+021924.9: An Interesting Gravitationally Lensed Quasar from the Sloan Digital Sky Survey. *AJ*, **126**, 666–674. xvii, xix, 66, 81, 85

Inada, N., Oguri, M., Pindor, B., Hennawi, J.F., Chiu, K., Zheng, W., Ichikawa, S.I., Gregg, M.D., Becker, R.H., Suto, Y., Strauss, M.A., Turner, E.L., Keeton, C.R., Annis, J., Castander, F.J., Eisenstein, D.J., Frieman, J.A., Fukugita, M., Gunn, J.E., Johnston, D.E., Kent, S.M., Nichol, R.C., Richards, G.T., Rix, H.W., Sheldon, E.S., Bahcall, N.A., Brinkmann, J., Ivezić, Ž., Lamb, D.Q., McKay, T.A., Schneider, D.P. & York, D.G. (2003b). A gravitationally lensed quasar with quadruple images separated by 14.62arcseconds. *Nature*, **426**, 810–812. xvii, xix, 58, 66, 85

Irwin, M.J., Webster, R.L., Hewett, P.C., Corrigan, R.T. & Jedrzejewski, R.I. (1989). Photometric variations in the Q2237 + 0305 system - First detection of a microlensing event. *AJ*, **98**, 1989–1994. 26, 59

Ivezic, Z., Tyson, J.A., Abel, B., Acosta, E., Allsman, R., AlSayyad, Y., Anderson, S.F., Andrew, J., Angel, R., Angeli, G., Ansari, R., Antilogus, P., Arndt, K.T., Astier, P., Aubourg, E., Axelrod, T., Bard, D.J., Barr, J.D., Barrau, A., Bartlett, J.G., Bauman, B.J., Beaumont, S., Becker, A.C., Becla, J., Beldica, C., Bellavia, S., Blanc, G., Blandford, R.D., Bloom, J.S., Bogart, J., Borne, K., Bosch, J.F., Boutigny, D., Brandt, W.N., Brown, M.E., Bullock, J.S., Burchat, P., Burke, D.L., Cagnoli, G., Calabrese, D., Chandrasekharan, S., Chesley, S., Cheu, E.C., Chiang, J., Claver, C.F., Connolly, A.J., Cook, K.H., Cooray, A., Covey, K.R., Cribbs, C., Cui, W., Cutri, R., Daubard, G., Daues, G., Delgado, F., Digel, S., Doherty, P., Dubois, R., Dubois-Felsmann, G.P., Durech, J., Eracleous, M., Ferguson, H., Frank, J., Freemon, M., Gangler, E., Gawiser, E., Geary, J.C., Gee, P., Geha, M., Gibson, R.R., Gilmore, D.K.,

Glanzman, T., Goodenow, I., Gressler, W.J., Gris, P., Guyonnet, A., Hascall, P.A., Haupt, J., Hernandez, F., Hogan, C., Huang, D., Huffer, M.E., Innes, W.R., Jacoby, S.H., Jain, B., Jee, J., Jernigan, J.G., Jevremovic, D., Johns, K., Jones, R.L., Juramy-Gilles, C., Juric, M., Kahn, S.M., Kalirai, J.S., Kallivayalil, N., Kalmbach, B., Kantor, J.P., Kasliwal, M.M., Kessler, R., Kirkby, D., Knox, L., Kotov, I., Krabbendam, V.L., Krughoff, S., Kubanek, P., Kuczewski, J., Kulkarni, S., Lambert, R., Le Guillou, L., Levine, D., Liang, M., Lim, K., Lintott, C., Lupton, R.H., Mahabal, A., Marshall, P., Marshall, S., May, M., McKercher, R., Migliore, M., Miller, M., Mills, D.J., Monet, D.G., Moniez, M., Neill, D.R., Nief, J., Nomerotski, A., Nordby, M., O'Connor, P., Oliver, J., Olivier, S.S., Olsen, K., Ortiz, S., Owen, R.E., Pain, R., Peterson, J.R., Petry, C.E., Pierfederici, F., Pietrowicz, S., Pike, R., Pinto, P.A., Plante, R., Plate, S., Price, P.A., Prouza, M., Radeka, V., Rajagopal, J., Rasmussen, A., Regnault, N., Ridgway, S.T., Ritz, S., Rosing, W., Roucelle, C., Rumore, M.R., Russo, S., Saha, A., Sassolas, B., Schalk, T.L., Schindler, R.H., Schneider, D.P., Schumacher, G., Sebag, J., Sembroski, G.H., Seppala, L.G., Shipsey, I., Silvestri, N., Smith, J.A., Smith, R.C., Strauss, M.A., Stubbs, C.W., Sweeney, D., Szalay, A., Takacs, P., Thaler, J.J., Van Berg, R., Vanden Berk, D., Vetter, K., Virieux, F., Xin, B., Walkowicz, L., Walter, C.W., Wang, D.L., Warner, M., Willman, B., Wittman, D., Wolff, S.C., Wood-Vasey, W.M., Yoachim, P., Zhan, H. & for the LSST Collaboration (2008). LSST: from Science Drivers to Reference Design and Anticipated Data Products. *ArXiv e-prints*. 107

Jackson, N. (2008). Gravitational lenses and lens candidates identified from the COSMOS field. *MNRAS*, **389**, 1311–1318. 84

Jackson, N. (2011). The Faintest Radio Source Yet: Expanded Very Large Array Observations of the Gravitational Lens SDSS J1004+4112. *ApJ*, **739**, L28. xvii, 58, 66, 81, 85

Jackson, N. (2013). Quasar lensing. *Bulletin of the Astronomical Society of India*, **41**, 19. 58

Jackson, N., Xanthopoulos, E. & Browne, I.W.A. (2000). NICMOS images of JVAS/CLASS gravitational lens systems. *MNRAS*, **311**, 389–396. 60

Jackson, N., Tagore, A.S., Roberts, C., Sluse, D., Stacey, H., Vives-Arias, H., Wucknitz, O. & Volino, F. (2015). Observations of radio-quiet quasars at 10-mas resolution by use of gravitational lensing. *MNRAS*, **454**, 287–298. 92

Jiménez-Vicente, J., Mediavilla, E., Muñoz, J.A. & Kochanek, C.S. (2012). A Robust Determination of the Size of Quasar Accretion Disks Using Gravitational Microlensing. *ApJ*, **751**, 106. 27, 30

Jiménez-Vicente, J., Mediavilla, E., Kochanek, C.S., Muñoz, J.A., Motta, V., Falco, E. & Mosquera, A.M. (2014). The Average Size and Temperature Profile of Quasar Accretion Disks. *ApJ*, **783**, 47. 27

Jiménez-Vicente, J., Mediavilla, E., Kochanek, C.S. & Muñoz, J.A. (2015a). Dark Matter Mass Fraction in Lens Galaxies: New Estimates from Microlensing. *ApJ*, **799**, 149. 20

Jiménez-Vicente, J., Mediavilla, E., Kochanek, C.S. & Muñoz, J.A. (2015b). Probing the Dark Matter Radial Profile in Lens Galaxies and the Size of X-Ray Emitting Region in Quasars with Microlensing. *ApJ*, **806**, 251. 20

Kafle, P.R., Sharma, S., Lewis, G.F. & Bland-Hawthorn, J. (2014). On the Shoulders of Giants: Properties of the Stellar Halo and the Milky Way Mass Distribution. *ApJ*, **794**, 59. 23, 41, 60

Kayo, I., Inada, N., Oguri, M., Hall, P.B., Kochanek, C.S., Richards, G.T., Schneider, D.P., York, D.G. & Pan, K. (2007). A New Quadruply Lensed Quasar: SDSS J125107.57+293540.5. *AJ*, **134**, 1515–1521. xvii, 85

Kayser, R., Surdej, J., Condon, J.J., Kellermann, K.I., Magain, P., Remy, M. & Smette, A. (1990). New observations and gravitational lens models of the Cloverleaf quasar H1413 + 117. *ApJ*, **364**, 15–22. 84

Keeton, C.R. (2001). Computational Methods for Gravitational Lensing. *ArXiv Astrophysics e-prints*. 45

Keeton, C.R. (2011). GRAVLENS: Computational Methods for Gravitational Lensing. Astrophysics Source Code Library. 45

Keeton, C.R., Gaudi, B.S. & Petters, A.O. (2003). Identifying Lenses with Small-Scale Structure. I. Cusp Lenses. *ApJ*, **598**, 138–161. 23, 60

Keeton, C.R., Burles, S., Schechter, P.L. & Wambsganss, J. (2006). Differential Microlensing of the Continuum and Broad Emission Lines in SDSS J0924+0219, the Most Anomalous Lensed Quasar. *ApJ*, **639**, 1–6. 92

Kellermann, K.I., Sramek, R.A., Schmidt, M., Green, R.F. & Shaffer, D.B. (1994). The radio structure of radio loud and radio quiet quasars in the Palomar Bright Quasar Survey. *AJ*, **108**, 1163–1177. 83

Kimball, A.E., Kellermann, K.I., Condon, J.J., Ivezić, Ž. & Perley, R.A. (2011). The Two-component Radio Luminosity Function of Quasi-stellar Objects: Star Formation and Active Galactic Nucleus. *ApJ*, **739**, L29. 83

Klypin, A., Kravtsov, A.V., Valenzuela, O. & Prada, F. (1999). Where Are the Missing Galactic Satellites? *ApJ*, **522**, 82–92. 21, 41, 60

Kneib, J.P., Cohen, J.G. & Hjorth, J. (2000). RX J0911+05: A Massive Cluster Lens at z=0.769. *ApJ*, **544**, L35–L39. xix, 66

Kochanek, C.S. (1991). The implications of lenses for galaxy structure. *ApJ*, **373**, 354–368. 23, 90

Kochanek, C.S. (2004a). Part 2: Strong gravitational lensing. In G. Meylan, P. Jetzer, P. North, P. Schneider, C.S. Kochanek & J. Wambsganss, eds., *Saas-Fee Advanced Course 33: Gravitational Lensing: Strong, Weak and Micro*, Saas-Fee Advanced Course, 91–268, Springer-Verlag Berlin Heidelberg. 6, 17, 58

Kochanek, C.S. (2004b). Quantitative Interpretation of Quasar Microlensing Light Curves. *ApJ*, **605**, 58–77. 27, 32, 33, 34, 48

Kochanek, C.S. (2006). Part 2: Strong gravitational lensing. In G. Meylan, P. Jetzer, P. North, P. Schneider, C.S. Kochanek & J. Wambsganss, eds., *Saas-Fee Advanced Course 33: Gravitational Lensing: Strong, Weak and Micro*, 91–268. 40

Kochanek, C.S. & Dalal, N. (2004). Tests for Substructure in Gravitational Lenses. *ApJ*, **610**, 69–79. 40, 41

Kochanek, C.S., Falco, E.E., Impey, C.D., Lehár, J., McLeod, B.A., Rix, H.W., Keeton, C.R., Muñoz, J.A. & Peng, C.Y. (2000). The Fundamental Plane of Gravitational Lens Galaxies and The Evolution of Early-Type Galaxies in Low-Density Environments. *ApJ*, **543**, 131–148. 23

Kochanek, C.S., Morgan, N.D., Falco, E.E., McLeod, B.A., Winn, J.N., Dembicky, J. & Ketzeback, B. (2006). The Time Delays of Gravitational Lens HE 0435-1223: An Early-Type Galaxy with a Rising Rotation Curve. *ApJ*, **640**, 47–61. 74

Koopmans, L.V.E. (2005). Gravitational imaging of cold dark matter substructures. *MNRAS*, **363**, 1136–1144. 61

Koopmans, L.V.E. & de Bruyn, A.G. (2000). Microlensing of multiply-imaged compact radio sources. Evidence for compact halo objects in the disk galaxy of B1600+434. *A&A*, **358**, 793–811. 59

Koopmans, L.V.E., Biggs, A., Blandford, R.D., Browne, I.W.A., Jackson, N.J., Mao, S., Wilkinson, P.N., de Bruyn, A.G. & Wambsganss, J. (2003). Extrinsic Radio Variability of JVAS/CLASS Gravitational Lenses. *ApJ*, **595**, 712–718. 59, 92

Koposov, S.E., Belokurov, V., Torrealba, G. & Evans, N.W. (2015). Beasts of the Southern Wild : Discovery of nine Ultra Faint satellites in the vicinity of the Magellanic Clouds. *ApJ*, **805**, 130. 21, 41, 60

Koptelova, E.A., Oknyanskij, V.L. & Shimanovskaya, E.V. (2006). Determining time delay in the gravitationally lensed system QSO2237+0305. *A&A*, **452**, 37–46. 26

Kratzer, R.M., Richards, G.T., Goldberg, D.M., Oguri, M., Kochanek, C.S., Hodge, J.A., Becker, R.H. & Inada, N. (2011). Analyzing the Flux Anomalies of the Large-separation Lensed Quasar SDSS J1029+2623. *ApJ*, **728**, L18. 60

Kravtsov, A.V., Gnedin, O.Y. & Klypin, A.A. (2004). The Tumultuous Lives of Galactic Dwarfs and the Missing Satellites Problem. *ApJ*, **609**, 482–497. 21

Laor, A. & Behar, E. (2008). On the origin of radio emission in radio-quiet quasars. *MNRAS*, **390**, 847–862. 59, 84, 107

Lehár, J., Falco, E.E., Kochanek, C.S., McLeod, B.A., Muñoz, J.A., Impey, C.D., Rix, H.W., Keeton, C.R. & Peng, C.Y. (2000). Hubble Space Telescope Observations of 10 Two-Image Gravitational Lenses. *ApJ*, **536**, 584–605. 28

Leipski, C., Falcke, H., Bennert, N. & Hüttemeister, S. (2006). The radio structure of radio-quiet quasars. *A&A*, **455**, 161–172. 59

Lynden-Bell, D. (1969). Galactic Nuclei as Collapsed Old Quasars. *Nature*, **223**, 690–694. 14

Macciò, A.V. & Miranda, M. (2006). The effect of low-mass substructures on the cusp lensing relation. *MNRAS*, **368**, 599–608. 23, 90

Macciò, A.V., Moore, B., Stadel, J. & Diemand, J. (2006). Radial distribution and strong lensing statistics of satellite galaxies and substructure using high-resolution ΛCDM hydrodynamical simulations. *MNRAS*, **366**, 1529–1538. 23, 60, 90

MacLeod, C.L., Kochanek, C.S. & Agol, E. (2009). Detection of a Companion Lens Galaxy Using the Mid-Infrared Flux Ratios of the Gravitationally Lensed Quasar H1413+117. *ApJ*, **699**, 1578–1583. 41

MacLeod, C.L., Jones, R., Agol, E. & Kochanek, C.S. (2013). Detection of Substructure in the Gravitationally Lensed Quasar MG0414+0534 Using Mid-infrared and Radio VLBI Observations. *ApJ*, **773**, 35. 41

MacLeod, C.L., Morgan, C.W., Mosquera, A., Kochanek, C.S., Tewes, M., Courbin, F., Meylan, G., Chen, B., Dai, X. & Chartas, G. (2015). A Consistent Picture Emerges: A Compact X-Ray Continuum Emission Region in the Gravitationally Lensed Quasar SDSS J0924+0219. *ApJ*, **806**, 258. 27

Mao, S. & Schneider, P. (1998). Evidence for substructure in lens galaxies? *MNRAS*, **295**, 587. 60, 86

Mao, S., Jing, Y., Ostriker, J.P. & Weller, J. (2004). Anomalous Flux Ratios in Gravitational Lenses: For or against Cold Dark Matter? *ApJ*, **604**, L5–L8. 23, 90

Marshall, P.J., Bradac, M., Chartas, G., Dobler, G., Eliasdottir, A., Falco, E., Fassnacht, C.D., Jee, M.J., Keeton, C.R., Oguri, M., Tyson, J.A. & LSST Strong Lensing Science Collaboration (2010). Strong Gravitational Lensing with LSST. In *American Astronomical Society Meeting Abstracts #215*, vol. 42 of *Bulletin of the American Astronomical Society*, 219. 107

McLeod, B.A., Bernstein, G.M., Rieke, M.J. & Weedman, D.W. (1998). The Gravitational Lens MG 0414+0534: A Link between Red Galaxies and Dust. *AJ*, **115**, 1377–1382. 28

Mediavilla, E., Muñoz, J.A., Lopez, P., Mediavilla, T., Abajas, C., Gonzalez-Morcillo, C. & Gil-Merino, R. (2006). A Fast and Very Accurate Approach to the Computation of Microlensing Magnification Patterns Based on Inverse Polygon Mapping. *ApJ*, **653**, 942–953. 13, 30, 47, 96

Mediavilla, E., Mediavilla, T., Muñoz, J.A., Ariza, O., Lopez, P., Gonzalez-Morcillo, C. & Jimenez-Vicente, J. (2011a). New Developments on Inverse Polygon Mapping to Calculate Gravitational Lensing Magnification Maps: Optimized Computations. *ApJ*, **741**, 42. 13, 30, 47, 96

Mediavilla, E., Muñoz, J.A., Kochanek, C.S., Guerras, E., Acosta-Pulido, J., Falco, E., Motta, V., Arribas, S., Manchado, A. & Mosquera, A. (2011b). The Structure of the Accretion Disk in the Lensed Quasar SBS 0909+532. *ApJ*, **730**, 16. 27, 30

Metcalf, R.B. (2005). The Importance of Intergalactic Structure to Gravitationally Lensed Quasars. *ApJ*, **629**, 673–679. 60

Metcalf, R.B. & Amara, A. (2012). Small-scale structures of dark matter and flux anomalies in quasar gravitational lenses. *MNRAS*, **419**, 3414–3425. 23, 60, 86, 90

Metcalf, R.B. & Zhao, H. (2002). Flux Ratios as a Probe of Dark Substructures in Quadruple-Image Gravitational Lenses. *ApJ*, **567**, L5–L8. 60

Metcalf, R.B., Moustakas, L.A., Bunker, A.J. & Parry, I.R. (2004). Spectroscopic Gravitational Lensing and Limits on the Dark Matter Substructure in Q2237+0305. *ApJ*, **607**, 43–59. 54

Minezaki, T., Chiba, M., Kashikawa, N., Inoue, K.T. & Kataza, H. (2009). Subaru Mid-Infrared Imaging of the Quadruple Lenses. II. Unveiling Lens Structure of MG0414+0534 and Q2237+030. *ApJ*, **697**, 610–618. xiv, xv, 27, 32, 41, 44, 48, 49, 50, 51, 54, 92, 105

Mittal, R., Porcas, R., Wucknitz, O., Biggs, A. & Browne, I. (2006). VLBI phase-reference observations of the gravitational lens JVAS B0218+357. *A&A*, **447**, 515–524. 59

Moore, B., Ghigna, S., Governato, F., Lake, G., Quinn, T., Stadel, J. & Tozzi, P. (1999). Dark Matter Substructure within Galactic Halos. *ApJ*, **524**, L19–L22. 21, 41, 60

Morgan, C.W., Kochanek, C.S., Dai, X., Morgan, N.D. & Falco, E.E. (2008). X-Ray and Optical Microlensing in the Lensed Quasar PG 1115+080. *ApJ*, **689**, 755–761. 81

Morgan, C.W., Kochanek, C.S., Morgan, N.D. & Falco, E.E. (2010). The Quasar Accretion Disk Size-Black Hole Mass Relation. *ApJ*, **712**, 1129–1136. 27, 34, 105

Morgan, N.D., Caldwell, J.A.R., Schechter, P.L., Dressler, A., Egami, E. & Rix, H.W. (2004). WFI J2026-4536 and WFI J2033-4723: Two New Quadruple Gravitational Lenses. *AJ*, **127**, 2617–2630. 92

Morgan, N.D., Kochanek, C.S., Pevunova, O. & Schechter, P.L. (2005). The Lens Redshift and Galaxy Environment for HE 0435-1223. *AJ*, **129**, 2531–2541. xix, 66, 74, 87

Mortonson, M.J., Schechter, P.L. & Wambsganss, J. (2005). Size Is Everything: Universal Features of Quasar Microlensing with Extended Sources. *ApJ*, **628**, 594–603. 32, 34, 47

Mosquera, A.M. & Kochanek, C.S. (2011). The Microlensing Properties of a Sample of 87 Lensed Quasars. *ApJ*, **738**, 96. 27, 34, 70, 105

Mosquera, A.M., Muñoz, J.A. & Mediavilla, E. (2009). Detection of Chromatic Microlensing in Q 2237 + 0305 A. *ApJ*, **691**, 1292–1299. 27, 28, 40

Mosquera, A.M., Kochanek, C.S., Chen, B., Dai, X., Blackburne, J.A. & Chartas, G. (2013). The Structure of the X-Ray and Optical Emitting Regions of the Lensed Quasar Q 2237+0305. *ApJ*, **769**, 53. xiv, 26, 27, 34, 36, 54, 105

Motta, V., Mediavilla, E., Muñoz, J.A. & Falco, E. (2004). Study of the Extended Narrow-Line Region in the Host Galaxy of the Lensed QSO 2237+0305 (z = 1.69). *ApJ*, **613**, 86–94. 26

Motta, V., Mediavilla, E., Falco, E. & Muñoz, J.A. (2012). Measuring Microlensing Using Spectra of Multiply Lensed Quasars. *ApJ*, **755**, 82. 27

Moustakas, L.A. & Metcalf, R.B. (2003). Detecting dark matter substructure spectroscopically in strong gravitational lenses. *MNRAS*, **339**, 607–615. 61

Moustakas, L.A., Brownstein, J., Fadely, R., Fassnacht, C.D., Gavazzi, R., Goodsall, T., Griffith, R.L., Keeton, C.R., Kneib, J.P., Koekemoer, A., Koopmans, L.V.E., Marshall, P.J., Merten, J., Metcalf, R.B., Oguri, M., Papovich, C., Rein, H., Ryan, R., Stewart, K.R. & Treu, T. (2012). The Orphan Lenses Project. In *American Astronomical Society Meeting Abstracts #219*, vol. 219 of *American Astronomical Society Meeting Abstracts*, 146.01. 66

Muñoz, J.A., Kochanek, C.S. & Keeton, C.R. (2001). Cusped Mass Models of Gravitational Lenses. *ApJ*, **558**, 657–665. 52, 95

Muñoz, J.A., Falco, E.E., Kochanek, C.S., McLeod, B.A. & Mediavilla, E. (2004). The Extinction Law in High-Redshift Galaxies. *ApJ*, **605**, 614–619. 28, 40, 60

Muñoz, J.A., Mediavilla, E., Kochanek, C.S., Falco, E.E. & Mosquera, A.M. (2011). A Study of Gravitational Lens Chromaticity with the Hubble Space Telescope. *ApJ*, **742**, 67. 27, 30, 40, 59

Muñoz, J.A., Vives-Arias, H., Mosquera, A.M., Jiménez-Vicente, J., Kochanek, C.S. & Mediavilla, E. (2016). Structure of the Accretion Disk in the Lensed Quasar Q2237+0305 from Multi-epoch and Multi-wavelength Narrowband Photometry. *ApJ*, **817**, 155. xiv, 47, 48, 49, 54

Muxlow, T.W.B., Richards, A.M.S., Garrington, S.T., Wilkinson, P.N., Anderson, B., Richards, E.A., Axon, D.J., Fomalont, E.B., Kellermann, K.I., Partridge, R.B. & Windhorst, R.A. (2005). High-resolution studies of radio sources in the Hubble Deep and Flanking Fields. *MNRAS*, **358**, 1159–1194. 84

Myers, S.T., Jackson, N.J., Browne, I.W.A., de Bruyn, A.G., Pearson, T.J., Readhead, A.C.S., Wilkinson, P.N., Biggs, A.D., Blandford, R.D., Fassnacht, C.D., Koopmans, L.V.E., Marlow, D.R., McKean, J.P., Norbury, M.A., Phillips, P.M., Rusin, D., Shepherd, M.C. & Sykes, C.M. (2003). The Cosmic Lens All-Sky Survey - I. Source selection and observations. *MNRAS*, **341**, 1–12. 58

Nadeau, D., Yee, H.K.C., Forrest, W.J., Garnett, J.D., Ninkov, Z. & Pipher, J.L. (1991). Infrared and visible photometry of the gravitational lens systems 2237 + 030. *ApJ*, **376**, 430–438. 40

Narayan, R. & Bartelmann, M. (1997). Lectures on Gravitational Lensing. *ArXiv Astrophysics e-prints*. 2

Netzer, H. (2015). Revisiting the Unified Model of Active Galactic Nuclei. *ARA&A*, **53**, 365–408. 14

Nierenberg, A.M., Treu, T., Wright, S.A., Fassnacht, C.D. & Auger, M.W. (2014). Detection of substructure with adaptive optics integral field spectroscopy of the gravitational lens B1422+231. *MNRAS*, **442**, 2434–2445. 61

Novikov, I.D. & Thorne, K.S. (1973). Astrophysics of black holes. In C. Dewitt & B.S. Dewitt, eds., *Black Holes (Les Astres Occlus)*, 343–450. 26

Ofek, E.O., Maoz, D., Rix, H.W., Kochanek, C.S. & Falco, E.E. (2006). Spectroscopic Redshifts for Seven Lens Galaxies. *ApJ*, **641**, 70–77. xix, 66

Oguri, M., Inada, N., Blackburne, J.A., Shin, M.S., Kayo, I., Strauss, M.A., Schneider, D.P. & York, D.G. (2008). Mass models and environment of the new quadruply lensed quasar SDSS J1330+1810. *MNRAS*, **391**, 1973–1980. xvii, 85

Oke, J.B. (1963). Absolute Energy Distribution in the Optical Spectrum of 3C 273. *Nature*, **197**, 1040–1041. 13

Østman, L., Goobar, A. & Mörtsell, E. (2008). Extinction properties of lensing galaxies. *A&A*, **485**, 403–415. 60

PandaX-II Collaboration, :, Tan, A., Xiao, M., Cui, X., Chen, X., Chen, Y., Fang, D., Fu, C., Giboni, K., Giuliani, F., Gong, H., Hu, S., Huang, X., Ji, X., Ju, Y., Lei, S., Li, S., Li, X., Li, X., Liang, H., Lin, Q., Liu, H., Liu, J., Lorenzon, W., Ma, Y., Mao, Y., Ni, K., Ren, X., Schubnell, M., Shen, M., Shi, F., Wang, H., Wang, J., Wang, M., Wang, Q., Wang, S., Wang, X., Wang, Z., Wu, S., Xiao, X., Xie, P., Yan, B., Yang, Y., Yue, J., Zeng, X., Zhang, H., Zhang, H., Zhang, H., Zhang, T., Zhao, L., Zhou, J., Zhou,

N. & Zhou, X. (2016). Dark Matter Results from First 98.7-day Data of PandaX-II Experiment. *ArXiv e-prints*. 21

Phillips, P.M., Norbury, M.A., Koopmans, L.V.E., Browne, I.W.A., Jackson, N.J., Wilkinson, P.N., Biggs, A.D., Blandford, R.D., de Bruyn, A.G., Fassnacht, C.D., Helbig, P., Mao, S., Marlow, D.R., Myers, S.T., Pearson, T.J., Readhead, A.C.S., Rusin, D. & Xanthopoulos, E. (2000). A new quadruple gravitational lens system: CLASS B0128+437. *MNRAS*, **319**, L7–L11. 59

Planck Collaboration, Ade, P.A.R., Aghanim, N., Armitage-Caplan, C., Arnaud, M., Ashdown, M., Atrio-Barandela, F., Aumont, J., Baccigalupi, C., Banday, A.J. & et al. (2014). Planck 2013 results. XV. CMB power spectra and likelihood. *A&A*, **571**, A15. 20

Poindexter, S. & Kochanek, C.S. (2010a). Microlensing Evidence that a Type 1 Quasar is Viewed Face-On. *ApJ*, **712**, 668–673. xiv, 27, 34, 36, 54, 105

Poindexter, S. & Kochanek, C.S. (2010b). The Transverse Peculiar Velocity of the Q2237+0305 Lens Galaxy and the Mean Mass of Its Stars. *ApJ*, **712**, 658–667. 30, 34

Poindexter, S., Morgan, N. & Kochanek, C.S. (2008). The Spatial Structure of an Accretion Disk. *ApJ*, **673**, 34–38. 27, 40, 59

Pooley, D., Blackburne, J.A., Rappaport, S. & Schechter, P.L. (2007). X-Ray and Optical Flux Ratio Anomalies in Quadruply Lensed Quasars. I. Zooming in on Quasar Emission Regions. *ApJ*, **661**, 19–29. 27

Popović, L.Č. & Chartas, G. (2005). The influence of gravitational lensing on the spectra of lensed quasi-stellar objects. *MNRAS*, **357**, 135–144. 92

Ratnatunga, K.U., Griffiths, R.E. & Ostrander, E.J. (1999). The Top 10 List of Gravitational Lens Candidates from the HUBBLE SPACE TELESCOPE Medium Deep Survey. *AJ*, **117**, 2010–2023. xvii, 85

Reimers, D., Hagen, H.J., Baade, R., Lopez, S. & Tytler, D. (2002). Discovery of a new quadruply lensed QSO: HS 0810+2554 - A brighter twin to PG 1115+080. *A&A*, **382**, L26–L28. xvii, xix, 66, 70, 85

Reynolds, M.T., Walton, D.J., Miller, J.M. & Reis, R.C. (2014). A Rapidly Spinning Black Hole Powers the Einstein Cross. *ApJ*, **792**, L19. 26

Ricci, D., Poels, J., Elyiv, A., Finet, F., Sprimont, P.G., Anguita, T., Bozza, V., Browne, P., Burgdorf, M., Calchi Novati, S., Dominik, M., Dreizler, S., Glitrup, M., Grundahl, F., Harpsøe, K., Hessman, F., Hinse, T.C.,

Hornstrup, A., Hundertmark, M., Jørgensen, U.G., Liebig, C., Maier, G., Mancini, L., Masi, G., Mathiasen, M., Rahvar, S., Scarpetta, G., Skottfelt, J., Snodgrass, C., Southworth, J., Teuber, J., Thöne, C.C., Wambsganss, J., Zimmer, F., Zub, M. & Surdej, J. (2011). Flux and color variations of the quadruply imaged quasar HE 0435-1223. *A&A*, **528**, A42. 74

Riechers, D.A., Walter, F., Brewer, B.J., Carilli, C.L., Lewis, G.F., Bertoldi, F. & Cox, P. (2008). A Molecular Einstein Ring at z = 4.12: Imaging the Dynamics of a Quasar Host Galaxy Through a Cosmic Lens. *ApJ*, **686**, 851–858. 76

Rojas, K., Motta, V., Mediavilla, E., Falco, E., Jiménez-Vicente, J. & Muñoz, J.A. (2014). Strong Chromatic Microlensing in HE0047-1756 and SDSS1155+6346. *ApJ*, **797**, 61. 27

Rubin, V.C., Thonnard, N. & Ford, W.K., Jr. (1978). Extended rotation curves of high-luminosity spiral galaxies. IV - Systematic dynamical properties, SA through SC. *ApJ*, **225**, L107–L111. 19

Rubin, V.C., Ford, W.K.J. & . Thonnard, N. (1980). Rotational properties of 21 SC galaxies with a large range of luminosities and radii, from NGC 4605 /R = 4kpc/ to UGC 2885 /R = 122 kpc/. *ApJ*, **238**, 471–487. 19

Rumbaugh, N., Fassnacht, C.D., McKean, J.P., Koopmans, L.V.E., Auger, M.W. & Suyu, S.H. (2015). Radio monitoring campaigns of six strongly lensed quasars. *MNRAS*, **450**, 1042–1056. 92

Rusin, D., Kochanek, C.S., Falco, E.E., Keeton, C.R., McLeod, B.A., Impey, C.D., Lehár, J., Muñoz, J.A., Peng, C.Y. & Rix, H.W. (2003). The Evolution of a Mass-selected Sample of Early-Type Field Galaxies. *ApJ*, **587**, 143–159. 23

Sanders, D.B., Phinney, E.S., Neugebauer, G., Soifer, B.T. & Matthews, K. (1989). Continuum energy distribution of quasars - Shapes and origins. *ApJ*, **347**, 29–51. 17

Schechter, P.L., Pooley, D., Blackburne, J.A. & Wambsganss, J. (2014). A Calibration of the Stellar Mass Fundamental Plane at z ˜ 0.5 Using the Micro-lensing-induced Flux Ratio Anomalies of Macro-lensed Quasars. *ApJ*, **793**, 96. 91, 92

Schinnerer, E., Smolčić, V., Carilli, C.L., Bondi, M., Ciliegi, P., Jahnke, K., Scoville, N.Z., Aussel, H., Bertoldi, F., Blain, A.W., Impey, C.D., Koekemoer, A.M., Le Fevre, O. & Urry, C.M. (2007). The VLA-COSMOS Survey. II. Source Catalog of the Large Project. *ApJS*, **172**, 46–69. 84

Schinnerer, E., Sargent, M.T., Bondi, M., Smolčić, V., Datta, A., Carilli, C.L., Bertoldi, F., Blain, A., Ciliegi, P., Koekemoer, A. & Scoville, N.Z. (2010). The VLA-COSMOS Survey. IV. Deep Data and Joint Catalog. *ApJS*, **188**, 384–404. 84

Schmidt, M. (1963). 3C 273 : A Star-Like Object with Large Red-Shift. *Nature*, **197**, 1040. 13

Schmidt, R., Webster, R.L. & Lewis, G.F. (1998). Weighing a galaxy bar in the lens Q2237 + 0305. *MNRAS*, **295**, 488. 30

Schmidt, R.W. & Wambsganss, J. (2010). Quasar microlensing. *General Relativity and Gravitation*, **42**, 2127–2150. 17

Schneider, P. & Weiss, A. (1992). The gravitational lens equation near cusps. *A&A*, **260**, 1–13. 60

Schneider, P., Ehlers, J. & Falco, E.E. (1992). *Gravitational Lenses*. Springer, A&A Library. 9

Serjeant, S. (2012). Strong biases in infrared-selected gravitational lenses. *MNRAS*, **424**, 2429–2441. 76

Shakura, N.I. & Sunyaev, R.A. (1973). Black holes in binary systems. Observational appearance. *A&A*, **24**, 337–355. 15, 26

Shappee, B.J., Prieto, J.L., Grupe, D., Kochanek, C.S., Stanek, K.Z., De Rosa, G., Mathur, S., Zu, Y., Peterson, B.M., Pogge, R.W., Komossa, S., Im, M., Jencson, J., Holoien, T.W.S., Basu, U., Beacom, J.F., Szczygieł, D.M., Brimacombe, J., Adams, S., Campillay, A., Choi, C., Contreras, C., Dietrich, M., Dubberley, M., Elphick, M., Foale, S., Giustini, M., Gonzalez, C., Hawkins, E., Howell, D.A., Hsiao, E.Y., Koss, M., Leighly, K.M., Morrell, N., Mudd, D., Mullins, D., Nugent, J.M., Parrent, J., Phillips, M.M., Pojmanski, G., Rosing, W., Ross, R., Sand, D., Terndrup, D.M., Valenti, S., Walker, Z. & Yoon, Y. (2014). The Man behind the Curtain: X-Rays Drive the UV through NIR Variability in the 2013 Active Galactic Nucleus Outburst in NGC 2617. *ApJ*, **788**, 48. 27, 37, 105

Shields, G.A. (1978). Thermal continuum from acretion disks in quasars. *Nature*, **272**, 706–708. 15

Sluse, D., Claeskens, J.F., Hutsemékers, D. & Surdej, J. (2007). Multi-wavelength study of the gravitational lens system RXS J1131-1231. III. Long slit spectroscopy: micro-lensing probes the QSO structure. *A&A*, **468**, 885–901. 92

Sluse, D., Schmidt, R., Courbin, F., Hutsemékers, D., Meylan, G., Eigenbrod, A., Anguita, T., Agol, E. & Wambsganss, J. (2011). Zooming into the broad line region of the gravitationally lensed quasar QSO 2237 + 0305 ≡ the Einstein Cross. III. Determination of the size and structure of the C iv and C iii] emitting regions using microlensing. *A&A*, **528**, A100. xiv, 26, 27, 34, 36, 54, 105

Sluse, D., Chantry, V., Magain, P., Courbin, F. & Meylan, G. (2012a). COSMOGRAIL: the COSmological MOnitoring of GRAvItational Lenses. X. Modeling based on high-precision astrometry of a sample of 25 lensed quasars: consequences for ellipticity, shear, and astrometric anomalies. *A&A*, **538**, A99. 74, 81, 91, 92

Sluse, D., Hutsemékers, D., Courbin, F., Meylan, G. & Wambsganss, J. (2012b). Microlensing of the broad line region in 17 lensed quasars. *A&A*, **544**, A62. 74

Sluse, D., Kishimoto, M., Anguita, T., Wucknitz, O. & Wambsganss, J. (2013). Mid-infrared microlensing of accretion disc and dusty torus in quasars: effects on flux ratio anomalies. *A&A*, **553**, A53. 40, 48, 50, 54, 61, 106

Soldner, J.G.v. (1804). On the deflection of a light ray from its rectilinear motion, by the attraction of a celestial body at which it nearly passes by. *Berliner Astronomisches Jahrbuch*, 161–172. 2

Springel, V., Wang, J., Vogelsberger, M., Ludlow, A., Jenkins, A., Helmi, A., Navarro, J.F., Frenk, C.S. & White, S.D.M. (2008). The Aquarius Project: the subhaloes of galactic haloes. *MNRAS*, **391**, 1685–1711. 24

Stadel, J., Potter, D., Moore, B., Diemand, J., Madau, P., Zemp, M., Kuhlen, M. & Quilis, V. (2009). Quantifying the heart of darkness with GHALO - a multibillion particle simulation of a galactic halo. *MNRAS*, **398**, L21–L25. 21

Stalevski, M., Jovanović, P., Popović, L.Č. & Baes, M. (2012). Gravitational microlensing of active galactic nuclei dusty tori. *MNRAS*, **425**, 1576–1584. 40, 50, 106

Steenbrugge, K.C., Jolley, E.J.D., Kuncic, Z. & Blundell, K.M. (2011). Radio and X-ray emission from disc winds in radio-quiet quasars. *MNRAS*, **413**, 1735–1743. 59

Sugai, H., Kawai, A., Shimono, A., Hattori, T., Kosugi, G., Kashikawa, N., Inoue, K.T. & Chiba, M. (2007). Integral Field Spectroscopy of the Quadruply Lensed Quasar 1RXS J1131-1231: New Light on Lens Substructures. *ApJ*, **660**, 1016–1022. 61

Sykes, C.M., Browne, I.W.A., Jackson, N.J., Marlow, D.R., Nair, S., Wilkinson, P.N., Blandford, R.D., Cohen, J., Fassnacht, C.D., Hogg, D., Pearson, T.J., Readhead, A.C.S., Womble, D.S., Myers, S.T., de Bruyn, A.G., Bremer, M., Miley, G.K. & Schilizzi, R.T. (1998). The complex gravitational lens system B1933+503. *MNRAS*, **301**, 310–314. 40

Trott, C.M., Treu, T., Koopmans, L.V.E. & Webster, R.L. (2010). Stars and dark matter in the spiral gravitational lens 2237+0305. *MNRAS*, **401**, 1540–1551. 44, 45

Ulvestad, J.S., Wong, D.S., Taylor, G.B., Gallimore, J.F. & Mundell, C.G. (2005). VLBA Identification of the Milliarcsecond Active Nucleus in the Seyfert Galaxy NGC 4151. *AJ*, **130**, 936–944. 84

Urry, C.M. & Padovani, P. (1995). Unified Schemes for Radio-Loud Active Galactic Nuclei. *PASP*, **107**, 803. 14, 84

Urry, M. (2003). The AGN Paradigm for Radio-Loud Objects. In S. Collin, F. Combes & I. Shlosman, eds., *Active Galactic Nuclei: From Central Engine to Host Galaxy*, vol. 290 of *Astronomical Society of the Pacific Conference Series*, 3. 14

Vakulik, V., Schild, R., Dudinov, V., Nuritdinov, S., Tsvetkova, V., Burkhonov, O. & Akhunov, T. (2006). Observational determination of the time delays in gravitational lens system Q2237+0305. *A&A*, **447**, 905–913. 26

Vanden Berk, D.E., Richards, G.T., Bauer, A., Strauss, M.A., Schneider, D.P., Heckman, T.M., York, D.G., Hall, P.B., Fan, X., Knapp, G.R., Anderson, S.F., Annis, J., Bahcall, N.A., Bernardi, M., Briggs, J.W., Brinkmann, J., Brunner, R., Burles, S., Carey, L., Castander, F.J., Connolly, A.J., Crocker, J.H., Csabai, I., Doi, M., Finkbeiner, D., Friedman, S., Frieman, J.A., Fukugita, M., Gunn, J.E., Hennessy, G.S., Ivezić, Ž., Kent, S., Kunszt, P.Z., Lamb, D.Q., Leger, R.F., Long, D.C., Loveday, J., Lupton, R.H., Meiksin, A., Merelli, A., Munn, J.A., Newberg, H.J., Newcomb, M., Nichol, R.C., Owen, R., Pier, J.R., Pope, A., Rockosi, C.M., Schlegel, D.J., Siegmund, W.A., Smee, S., Snir, Y., Stoughton, C., Stubbs, C., SubbaRao, M., Szalay, A.S., Szokoly, G.P., Tremonti, C., Uomoto, A., Waddell, P., Yanny, B. & Zheng, W. (2001). Composite Quasar Spectra from the Sloan Digital Sky Survey. *AJ*, **122**, 549–564. 28

Vegetti, S. & Koopmans, L.V.E. (2009). Statistics of mass substructure from strong gravitational lensing: quantifying the mass fraction and mass function. *MNRAS*, **400**, 1583–1592. 61

Vegetti, S., Lagattuta, D.J., McKean, J.P., Auger, M.W., Fassnacht, C.D. & Koopmans, L.V.E. (2012). Gravitational detection of a low-mass dark satellite galaxy at cosmological distance. *Nature*, **481**, 341–343. 41, 61

Vegetti, S., Koopmans, L.V.E., Auger, M.W., Treu, T. & Bolton, A.S. (2014). Inference of the cold dark matter substructure mass function at z = 0.2 using strong gravitational lenses. *MNRAS*, **442**, 2017–2035. 54

Vives-Arias, H. & et al. (2016). *ApJ*, in preparation. 104

Vives-Arias, H., Muñoz, J.A., Kochanek, C.S., Mediavilla, E. & Jimenez-Vicente, J. (2016). Observations of the Lensed Quasar Q 2237+0305 with CanariCam at GTC. *ApJ*, **831**, 43. 61

Walsh, D., Carswell, R.F. & Weymann, R.J. (1979). 0957 + 561 A, B - Twin quasistellar objects or gravitational lens. *Nature*, **279**, 381–384. 58

Wambsganss, J. (2006). Part 4: Gravitational microlensing. In G. Meylan, P. Jetzer, P. North, P. Schneider, C.S. Kochanek & J. Wambsganss, eds., *Saas-Fee Advanced Course 33: Gravitational Lensing: Strong, Weak and Micro*, 453–540. 27

Wang, J., Frenk, C.S., Navarro, J.F., Gao, L. & Sawala, T. (2012). The missing massive satellites of the Milky Way. *MNRAS*, **424**, 2715–2721. 23, 41, 60

Wang, W., Han, J., Cooper, A.P., Cole, S., Frenk, C. & Lowing, B. (2015). Estimating the dark matter halo mass of our Milky Way using dynamical tracers. *MNRAS*, **453**, 377–400. 23

Warren, S.J. & Dye, S. (2003). Semilinear Gravitational Lens Inversion. *ApJ*, **590**, 673–682. 61

Wayth, R.B., O'Dowd, M. & Webster, R.L. (2005). A microlensing measurement of the size of the broad emission-line region in the lensed quasar QSO 2237+0305. *MNRAS*, **359**, 561–566. 26, 92

Webster, R.L., Ferguson, A.M.N., Corrigan, R.T. & Irwin, M.J. (1991). Interpreting the light curve of Q2237 + 0305. *AJ*, **102**, 1939–1945. 26

White, R.L., Helfand, D.J., Becker, R.H., Glikman, E. & de Vries, W. (2007). Signals from the Noise: Image Stacking for Quasars in the FIRST Survey. *ApJ*, **654**, 99–114. xvii, 58, 83, 84, 85

Winn, J.N., Morgan, N.D., Hewitt, J.N., Kochanek, C.S., Lovell, J.E.J., Patnaik, A.R., Pindor, B., Schechter, P.L. & Schommer, R.A. (2002). PMN J1632-0033: A New Gravitationally Lensed Quasar. *AJ*, **123**, 10–19. 58

Wisotzki, L., Koehler, T., Kayser, R. & Reimers, D. (1993). The new double QSO HE 1104-1805: Gravitational lens with microlensing or binary quasar? *A&A*, **278**, L15–L18. 58, 59

Wisotzki, L., Schechter, P.L., Bradt, H.V., Heinmüller, J. & Reimers, D. (2002). HE 0435-1223: A wide separation quadruple QSO and gravitational lens. *A&A*, **395**, 17–23. xvii, xix, 66, 74, 85, 87

Wisotzki, L., Becker, T., Christensen, L., Helms, A., Jahnke, K., Kelz, A., Roth, M.M. & Sanchez, S.F. (2003). Integral-field spectrophotometry of the quadruple QSO HE 0435-1223: Evidence for microlensing. *A&A*, **408**, 455–463. 92

Wisotzki, L., Becker, T., Christensen, L., Jahnke, K., Helms, A., Kelz, A., Roth, M.M. & Sánchez, S.F. (2004). Integral field spectrophotometry of gravitationally lensed QSOs with PMAS. *Astronomische Nachrichten*, **325**, 135–138. 87

Woźniak, P.R., Alard, C., Udalski, A., Szymański, M., Kubiak, M., Pietrzyński, G. & Zebruń, K. (2000). The Optical Gravitational Lensing Experiment Monitoring of QSO 2237+0305. *ApJ*, **529**, 88–92. 26, 30

Wucknitz, O. & Volino, F. (2008). The gravitational lens J1131-1231 — How to miss an opportunity and how to avoid it. In *The role of VLBI in the Golden Age for Radio Astronomy*, 102. xvii, 58, 66, 84, 85

Wyithe, J.S.B., Webster, R.L. & Turner, E.L. (2000). The distribution of microlensed light-curve derivatives: the relationship between stellar proper motions and transverse velocity. *MNRAS*, **312**, 843–852. 47

XENON100 Collaboration, Aprile, E., Aalbers, J., Agostini, F., Alfonsi, M., Amaro, F.D., Anthony, M., Arneodo, F., Barrow, P., Baudis, L., Bauermeister, B., Benabderrahmane, M.L., Berger, T., Breur, P.A., Brown, A., Brown, E., Bruenner, S., Bruno, G., Budnik, R., Bütikofer, L., Calvén, J., Cardoso, J.M.R., Cervantes, M., Cichon, D., Coderre, D., Colijn, A.P., Conrad, J., Cussonneau, J.P., Decowski, M.P., de Perio, P., Di Gangi, P., Di Giovanni, A., Diglio, S., Duchovni, E., Fei, J., Ferella, A.D., Fieguth, A., Franco, D., Fulgione, W., Gallo Rosso, A., Galloway, M., Gao, F., Garbini, M., Geis, C., Goetzke, L.W., Greene, Z., Grignon, C., Hasterok, C., Hogenbirk, E., Itay, R., Kaminsky, B., Kessler, G., Kish, A., Landsman, H., Lang, R.F., Lellouch, D., Levinson, L., Le Calloch, M., Levy, C., Lin, Q., Lindemann, S., Lindner, M., Lopes, J.A.M., Manfredini, A., Marrodán Undagoitia, T., Masbou, J., Massoli, F.V., Masson, D., Mayani, D., Meng, Y., Messina, M., Micheneau, K., Miguez,

B., Molinario, A., Murra, M., Naganoma, J., Ni, K., Oberlack, U., Orrigo, S.E.A., Pakarha, P., Pelssers, B., Persiani, R., Piastra, F., Pienaar, J., Piro, M.C., Plante, G., Priel, N., Rauch, L., Reichard, S., Reuter, C., Rizzo, A., Rosendahl, S., Rupp, N., dos Santos, J.M.F., Sartorelli, G., Scheibelhut, M., Schindler, S., Schreiner, J., Schumann, M., Scotto Lavina, L., Selvi, M., Shagin, P., Silva, M., Simgen, H., Sivers, M.v., Stein, A., Thers, D., Tiseni, A., Trinchero, G., Tunnell, C.D., Wall, R., Wang, H., Weber, M., Wei, Y., Weinheimer, C., Wulf, J. & Zhang, Y. (2016). XENON100 Dark Matter Results from a Combination of 477 Live Days. *ArXiv e-prints*. 21

Xu, D., Sluse, D., Gao, L., Wang, J., Frenk, C., Mao, S., Schneider, P. & Springel, V. (2015). How well can cold dark matter substructures account for the observed radio flux-ratio anomalies. *MNRAS*, **447**, 3189–3206. 60, 86, 91, 92

Xu, D.D., Mao, S., Wang, J., Springel, V., Gao, L., White, S.D.M., Frenk, C.S., Jenkins, A., Li, G. & Navarro, J.F. (2009). Effects of dark matter substructures on gravitational lensing: results from the Aquarius simulations. *MNRAS*, **398**, 1235–1253. 23, 60, 86, 90

Xu, D.D., Mao, S., Cooper, A.P., Wang, J., Gao, L., Frenk, C.S. & Springel, V. (2010). Substructure lensing: effects of galaxies, globular clusters and satellite streams. *MNRAS*, **408**, 1721–1729. 23, 90

Yee, H.K.C. (1988). High-resolution imaging of the gravitational lens system candidate 2237+030. *AJ*, **95**, 1331–1339. 25

Zackrisson, E. & Riehm, T. (2010). Gravitational Lensing as a Probe of Cold Dark Matter Subhalos. *Advances in Astronomy*, **2010**, 478910. 58

Zentner, A.R. & Bullock, J.S. (2003). Halo Substructure and the Power Spectrum. *ApJ*, **598**, 49–72. 21, 40, 54, 89

Zentner, A.R., Berlind, A.A., Bullock, J.S., Kravtsov, A.V. & Wechsler, R.H. (2005). The Physics of Galaxy Clustering. I. A Model for Subhalo Populations. *ApJ*, **624**, 505–525. 23

Zucker, D.B., Belokurov, V., Evans, N.W., Wilkinson, M.I., Irwin, M.J., Sivarani, T., Hodgkin, S., Bramich, D.M., Irwin, J.M., Gilmore, G., Willman, B., Vidrih, S., Fellhauer, M., Hewett, P.C., Beers, T.C., Bell, E.F., Grebel, E.K., Schneider, D.P., Newberg, H.J., Wyse, R.F.G., Rockosi, C.M., Yanny, B., Lupton, R., Smith, J.A., Barentine, J.C., Brewington, H., Brinkmann, J., Harvanek, M., Kleinman, S.J., Krzesinski, J., Long,

D., Nitta, A. & Snedden, S.A. (2006). A New Milky Way Dwarf Satellite in Canes Venatici. *ApJ*, **643**, L103–L106. 23, 41, 60

Zwicky, F. (1933). Die Rotverschiebung von extragalaktischen Nebeln. *Helvetica Physica Acta*, **6**, 110–127. 19

Zwicky, F. (1937). On the Masses of Nebulae and of Clusters of Nebulae. *ApJ*, **86**, 217. 19